LiDAR measurement correction for floating wind turbines

Matti Hitzerd

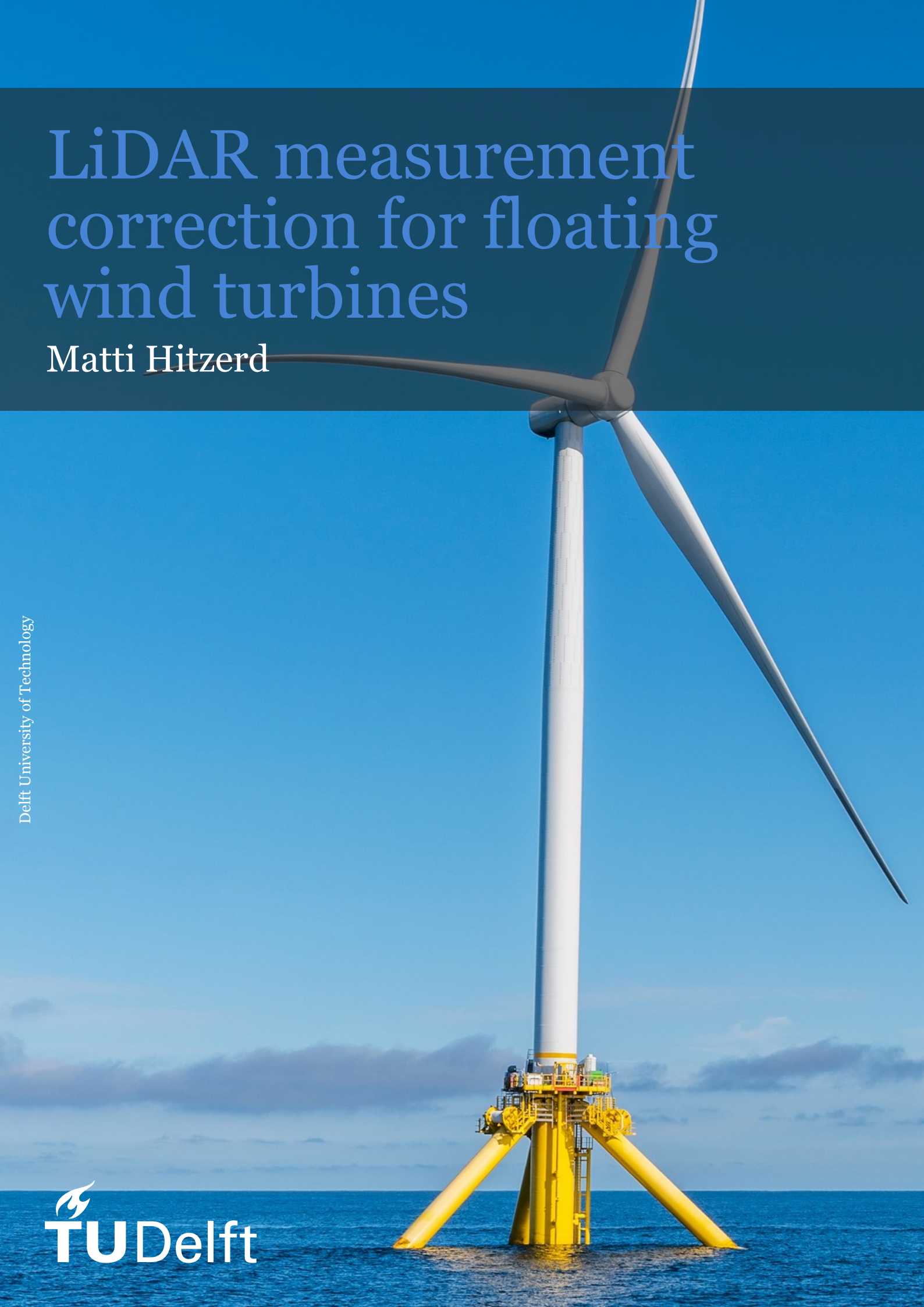

Delft University of Technology

TU Delft

LiDAR measurement correction for floating wind turbines

by

Matti Hitzerd

to obtain the degree of Master of Science

at the Delft University of Technology,

to be defended publicly on Monday February, 2025 at 13:00 o'clock.

Student number: 4853644
Project duration: April 1, 2024 – February 28, 2025

Thesis committee:

Dr. R. P. Dwight	TU Delft,	Supervisor
Dr. N. G. W. Warncke,	SGRE,	Supervisor
Dr. ir. W. A. A. M. Bierbooms	TU Delft,	External examiner
Dr. ir. A. H. van Zuijlen	TU Delft,	Chair

Cover: Tetraspar demonstrator from https://www.floatingwinddays.com/partners

TU Delft

Preface

The completion of this master's thesis marks the end of my academic journey at the Faculty of Aerospace Engineering at TU Delft. Over the years, I have grown both personally and intellectually, with this thesis being the most challenging yet insightful part of my studies.

I would like to express my sincere gratitude to my supervisor, Norbert Warncke, for his invaluable guidance throughout this project. Despite occasional challenges in communication, he has always taken the time to explain complex concepts and encouraged me to dive deeper into my research.

I am also deeply grateful to my TU Delft supervisor, Richard Dwight, for his support in navigating the challenges of conducting master's thesis research for the first time and for his insights into uncertainty propagation.

A special thanks goes to my colleagues at Siemens Gamesa Renewable Energy for their support, genuine interest in my research, and for welcoming me so warmly into the team. In particular, I would like to thank Dirk Rijnsdorp for his understanding and personal guidance, as well as Stavros Panagoulias and Sachin Navalkar for their continuous support and willingness to answer any questions. Colinda Rog should also be thanked for her never ending enthusiasm and kindness.

I also want to thank my colleagues in France for inviting me to their office in Paris and to the annual seminar. I am grateful for the opportunity to meet you, learn about your work, and see the inside of a wind turbine firsthand.

A heartfelt thank you to my fellow students at the office in The Hague for making my time there even more enjoyable. I was inspired by the way each of you tackled your own projects, and I deeply appreciated both the professional discussions we had and the moments we spent unwinding together outside the office. Your support and friendship meant a great deal to me.

Finally, I am profoundly grateful to my family and friends for their unwavering encouragement and genuine interest in my project. Your support has been invaluable throughout this journey, and I could not have done it without you.

Matti Hitzerd
Delft, February 2025

Summary

The transition to renewable energy sources is essential to mitigate climate change, and floating wind turbines (FOWTs) present a promising solution to harness offshore wind resources. Light Detection and Ranging (LiDAR) systems mounted on nacelles provide a cost-effective and efficient means to measure wind fields, critical for turbine performance, control and load simulation. However, FOWTs' motion introduces complexities in LiDAR measurements due to velocity and positional changes. This thesis focusses on developing a correction method for LiDAR measurements on FOWTs, addressing the influence of motion on wind velocity, position, and direction. The accuracy and uncertainty of these corrected measurements are quantified.

Simulated six degrees of freedom (6DOF) motion and a power law wind field are inserted in a numerical LiDAR model, in which corrected and uncorrected measurement position, direction and line of sight velocity are constructed. The corrected outputs are validated through reconstructed wind fields and the uncertainty of the correction is quantified. In this study, significant motion-induced bias is identified in the reconstructed wind fields. The dominant motion affecting measurement accuracy was identified as pitch motion, especially when it exhibits a non-zero mean. The relative error of the reconstructed power law wind field parameters is reduced by 3 orders of magnitude. Despite an increase in uncertainties associated with the correction method applied, the correction remains effective in reducing the error in LiDAR measurements induced by FOWT motions. The findings highlight the necessity and feasibility of motion correction for LiDAR measurements, offering substantial improvements in the accuracy and reliability of reconstructed wind fields for floating wind turbine applications.

Contents

Nomenclature

Abbreviations

Abbreviation	Definition
AD	Analog-to-Digital
BHawC	Bonus Horizontal axis wind turbine Code
CNR	Carrier-to-Noise ratio
CTP	Conventional Terrestrial Pole
ECEF	Earth-centred, Earth-fixed
DC	Direct Current
DFT	Direct Fourier Transform
DOF	Degrees of freedom
DWL	Doppler wind LiDAR
FOWT	Floating offshore wind turbine
FWHM	Full width half maximum
SNR	Signal-to-Noise ratio
GNSS	global navigation satellite system
IMU	Inertial Measurement Unit
LiDAR	Light Detection and Ranging
LO	Local oscillator
LOS	Line of sight
LSQ	Least squares
met	meteorological
PRNG	Psuedo-Random Number Generator
RAO	Response Amplitude Operator
REWS	Rotor effective wind speed
RWF	Range gate Weighting Function
SGRE	Siemens Gamesa Renewable Energy
TI	Turbulence intensity
TLP	Tension leg platform
TRS	Terrestrial reference system
ViConDAR	Virtual Constrained turbulence and liDAR measurements

Symbols

Symbol	Definition	Unit
A	Amplitude	$[m]$ / $[m/s]$ / [°]
a_0	Aperature diameter	$[m]$
c	Speed of light	$[m/s^2]$
$\mathbf{C}$	Covariance matrix	
$\mathbf{C}_d$	Covariance matrix of direction vector	[-]
$\mathbf{C}_p$	Covariance matrix of position vector	$[m^2]$
D	Diameter	$[m]$
D_{DC}	Direct current	$[A]$
$\vec{d}_i$	Normalised direction vector single particle	[-]
$\vec{d}_n$	Normalised mean direction vector laser beam	[-]
d_M	Mahalanobis distance	[m]
E	Electrical field magnitude	$[V/m]$
E	Young's modulus	$[Pa]$
$E_{U_{ref}}$	Error percentage of U_{ref}	[%]
E_α	Error percentage of α	[%]
F	Distance to centre range gate	$[m]$
F_i	Collection efficiency of scatter from particle i	[-]
F_{min}	Minimum range gate location	$[m]$
F_{max}	Maximum range gate location	$[m]$
f	Frequency	$[Hz]$
f	Focal length	[m]
H	Measurement height of V_{LOS} measurement	$[m]$
H_s	Wave height	$[m]$
$\mathbf{I}$	Identity matrix	[-]
I	Area moment of inertia	$[m^4]$
I	Light intensity	$[J]$
i_D	Current	$[A]$
I_n	Normalised light intensity	[-]
I_0	Peak light intensity	$[J]$
$\mathbf{J}$	Jacobian matrix	
k	Stiffness	$[N/m]$
k	wave number	$[m^{-1}]$
L	Length	$[m]$
m	mass	$[kg]$
m	Number of particles	[-]
N	Number of measurements	[-]
N_R	Number of range gates	[-]
P	Power	$[W]$
$\vec{P}_i$	Position vector individual particle	[m]
$\vec{P}_c$	Mean position of particles	[m]
$\vec{P}_{c,\text{exp}}$	Expected mean position of particles	[m]
p	Number of unknown parameters regression	[-]
$\vec{P}$	Position vector	[m]
q	Quaternion	[-]
$\mathbf{R}$	Rotation matrix	
R	Radius of curvature of wave fronts	$[m]$
R_{diode}	Responsivity of detector	[-]
r	radial distance orthogonal to laser beam	$[m]$
r_p	Half width of pulse	$[m]$
$\vec{r}_p$	Position vector to particle	$[m]$
$\vec{s}$	Rotation axis	[-]
$\vec{s}$	Normalised rotation axis	[-]

Symbol	Definition	Unit
T	Period	$[s]$
T_0	Wave period	$[s]$
t_{fit}	Sampling time of data to be fitted	$[s]$
t_{regr}	Sampling time of regression	$[s]$
U_{ref}	Reference wind speed for power law	$[m/s]$
u	Wind velocity in x-direction	$[m/s]$
v	Wind velocity in y-direction	$[m/s]$
$\vec{V}$	Wind velocity vector	$[m/s]$
V_{LOS}	Line of sight velocity	$[m/s]$
v_L	Speed of the LiDAR	$[m/s]$
v_p	Speed of a particle	$[m/s]$
w	Wind velocity in z-direction	$[m/s]$
w_i	Weight of individual particle point	[-]
w_0	Beam waist	$[m]$
$w(z)$	Beam radius	$[m]$
W	Weighting function	[-]
$\mathbf{W}$	Weight matrix	[-]
$\mathbf{X}$	Design matrix	
$\mathbf{X}^*$	Design matrix at time interval of prediction	
z_R	Rayleigh length	[-]
z_{ref}	Reference height for power law	$[m]$
α	Power law exponent	[-]
$\vec{\beta}$	Vector containing unknown variables for LSQ	
γ	Elevation angle of LiDAR	[°]
Δp	Range gate length	$[m]$
Δr	Full width at half maximum (FWHM)	$[m]$
Δt_{obs}	total observation time pulsed LiDAR	$[s]$
$\Delta \mathrm{v}$	Relative speed between LiDAR and particle	$[m/s]$
ε_0	Permittivity in vacuum	$[F/m]$
ϵ	Noise term	$[m]$ / $[m/s]$ / [°]
η_{eff}	Optical mixing efficiency	[-]
η_{rec}	Receiver loss and gain factor	[-]
θ	Zenith angle laser beam	[-]
θ_{div}	Gaussian beam divergence	[-]
θ_{pitch}	Pitch angle	[°]
λ	Wavelength	$[m]$
μ	Mean	[]
σ	Standard deviation	[]
σ_v	Standard deviation V_{LOS}	$[m/s]$
σ_y	Total standard deviation regression	$[m]$ / $[m/s]$ / [°]
$\sigma_{\hat{y}}$	Standard deviation model regression	$[m]$ / $[m/s]$ / [°]
σ_ϵ	Standard deviation noise	$[m]$ / $[m/s]$ / [°]
τ_p	Pulse $1/e$ duration	$[s]$
φ_s	Phase atmospheric signal	[rad]
φ_{roll}	Roll angle	[°]
ϕ	Rotation angle	[°]
ψ	Azimuth angle laser beam	[-]
ψ_{yaw}	Yaw angle	[°]
ω	Angular frequency	[Hz]
$\mathcal{B}$	Beam reference frame	
$\mathcal{G}$	Global reference frame	
$\mathcal{I}$	Inertial reference frame	
$\mathcal{L}$	LiDAR reference frame	

Symbol	Definition	Unit
$\mathcal{N}$	Normalisation factor for unbiased weighted (co)variance	[-]

1

Introduction

It is well known that the climate is changing and the global temperature is rising. This already has adverse effects on Earth's population and will continue to intensify over the coming years. To bring the warming of the Earth's atmosphere to a halt, significant reductions in greenhouse gases are required. It is known that in 2019 the energy sector still contributed to 34 % of global emissions in CO2 equivalents [12]. This includes direct and indirect emissions. While the wind energy sector is growing rapidly, more growth is required in the coming years to continue to decarbonise the energy sector and keep up with demand. In the COP28 it was decided that the annual growth in energy production by wind energy should roughly triple [29].

One way to contribute to the expansion of the wind energy fleet is by using floating wind turbines. These have the advantage that they can be built in deeper waters and thus more locations become available to extract wind energy. Next to this, the wind resource is usually higher in deeper waters as these are generally further from shore. In fact, 80 % of the total available global wind resource is located at water depths greater than $60\ m$ [50]. In the floating wind energy industry, a lot of development is still required before floating wind turbines become commercially viable. One of these aspects that needs to be developed is the reconstruction of the wind field that reaches the turbine. This knowledge is important for simulating the loads that the wind turbine experiences, but can also be used for control of the turbine or to construct its power curve.

The wind field in front of the turbine can be measured with a LiDAR (*Light Detection and Ranging*). This has advantages compared to simpler nacelle-mounted anemometers, such as cup or sonic anemometers, as the LiDAR can measure in a larger range in front of the turbine instead of measuring just at the mounting location of the measurement device. This provides a more complete picture of the wind field in terms of, for example, turbulence, turbine wakes or wind shear. Knowing this can optimise performance, minimise downtime and increase a wind turbine's lifetime. Of course, a LiDAR also has its challenges. It can, for example, not measure well when there is precipitation. Moreover, the blades of the turbine block the laser beams sometimes, reducing measurement availability. Compared to a met (meteorological) mast, the main advantage of using a LiDAR is the cost. A LiDAR is only a fraction of the price of a met mast, less than half a million euros for a LiDAR compared to about $15M$€for a MET mast [44]. besides, for floating wind in deep water, a met mast is not feasible due to high installation costs.

However, even though using a nacelle-based LiDAR on a floating turbine has high potential, it also presents some large challenges related to the floating motion of the turbine. An additional velocity is added to the LiDAR measurement by the movement of the LiDAR itself due to floating motions of the turbine. Next to this, the measurement position changes, as well as the direction in which the wind speed measurement is taken. Due to these alterations of the measurement, a correction for velocity, position and direction is required. In this research a part of this correction method is explored.

The basis for this research is to make a simulator for the LiDAR, in which a constructed wind field and wind turbine motion are given as inputs. The output wind velocity, direction and position are then used

in a reconstruction algorithm to reconstruct the wind field again. The input and reconstructed wind field are then compared as verification of the method. For this whole process, also the uncertainties of the outputs are required in order to determine the reliability of the correction and the measurement itself.

Once the uncertainties are known, the next step can also be taken in improving the model for generating a correction factor.

The aim is to use this research to reconstruct the wind field of a floating wind turbine demonstrator to simulate and validate the loads it experiences over its lifetime. The floating wind turbine demonstrator used is the Tetraspar, located at the Marine Energy Test Centre close to the Norwegian coastal city Karmøy. It is equipped with a pulsed coherent Doppler Wind LiDAR and an IMU to measure the global movement of the turbine and hence the LiDAR.

1.1. Existing literature

There already exists a large body of research investigating floating LiDARs. However, these researches are focussed on buoy-mounted LiDARs. It is hard to compare results between these studies and nacelle-mounted LiDARs as the movement response is much less direct for the latter. The response depends on the floater, tower and nacelle design that dedicate the stiffness and dynamics of the structure. However, for a buoy a more direct one-to-one relationship exists with the present sea-state conditions and the movement response. Besides that buoy-mounted LiDARs often point upward, instead of towards the mean wind direction, this results in orientation issues. Even though the results of buoy mounted LiDARs do not directly compare to those of nacelle-mounted ones, the correction methods used can still be useful to apply.

In [11] the correction for instantaneous line of sight velocity measurements is split in a correction for orientation change and translational velocity of the buoy. For their experiments a scanning continuous wave WindCube v2 mounted on an anchored buoy is used, and the orientation and translational velocities are measured by an IMU. First, the corrected measurement direction is found by multiplying the LiDAR direction vector with a transformation matrix that contains the orientation change of the buoy as measured by the IMU. The line of sight velocity is then found by multiplying the sampled wind field velocity with a rotational matrix. This rotational matrix is defined by the angles that define the LiDAR measurement cone, which are deduced from the rotated measurement direction vector. Next, the velocity measured is corrected for the translational velocity of the buoy. This velocity, too, is projected onto the beam, which can consequentially be added to the line of sight measurement to get the simulated V_{LOS} that the floating LiDAR would measure. In this method the change in measurement location is not considered, but for the research in this thesis this is an important factor as well.

As found in [26], nacelle-based LiDARs can be used to determine the power curve of floating wind turbines. A comparison study was conducted on a 2 MW floating turbine, where the 10-minute average reconstructed wind speed of the $1\ Hz$ line of sight velocities of four LiDAR measurements was compared to the results of a sonic anemometer. A 0.97 coefficient of determination of the correlation between LiDAR and the sonic anemometer has been found. In addition to this, higher nacelle excitations led to a larger uncertainty of the measurement. In conclusion, the paper recommends a more detailed quantification of the uncertainty of the measurement and to apply a motion compensation in terms of correction to decrease uncertainties. This highlights the relevance of this research and shows a potential application to power curve calculations for floating wind turbines.

From [19] it is concluded that a correction factor is indeed necessary for floating nacelle-based LiDARs, as a mean absolute error in the rotor effective wind speed is found to be up to 25 % for some floater motions. In this research the LiDAR is modelled and combined with an aeroelastic model of the wind turbine and floater. Some specific sea states are inserted, and the consequential error is calculated. The turbulence intensity (TI) and mean error of the rotor effective wind speed (REWS) were also found to be overestimated.

In [27] it was also found that for a LiDAR installed on a floating buoy the TI is overestimated, because an additional variance in the measured wind speed is added due to the platform's motion. The turbulence intensity is influenced by both rotational displacement and translational velocities, whereas the mean error of REWS is influenced mostly by rotational displacement resulting in a different position of the

measurement. This is relevant to determine the most influential movement to consider when performing this research. In this research, it is mentioned also that a detailed uncertainty quantification is desired to increase the trustworthiness of the results. Besides, a recommendation for further research is given to perform a parameter study exploring the effect of motion amplitudes and frequencies, together with looking into the influence of coupling between different degrees of freedom (DOF). It should also be noted that this research is limited to the evaluated wind and sea states and the behaviour of the floater used.

In [21] a first approach is described to correct for the motions of a floating wind turbine in nacelle-mounted LiDAR wind measurements. In this research a correction look-up table is constructed for specific motions for the 10-minute average wind speed. This is done using an analytical model of the LiDAR measurement. Next to this, a frequency filter is used for correction of floater pitch motions is implemented for instantaneous measurements, but this method is unlikely to be generalisable. For example, this method does not apply to varying pitch oscillations or to a combination of low pitch amplitudes and high periods. In [32] this was confirmed. In this research the analysis only focusses on limited DOFs: heave, yaw, pitch and roll for the turbine motions. The wind field input is limited to a power law wind profile for the analytical model, while turbulence is added using the Veers method in a turbulence generator. In further research, this can be improved by considering all DOFs and the coupling between them. Next to that, for the generation of a correction factor, more complicated input wind fields can be used. The goal of this research is to obtain a correction and uncertainty for instantaneous measurements, regardless of the floater motion or input wind field. This would be done by implementing the correction velocity in the LiDAR simulator and transforming the measurement location and direction vector to the global system while incorporating the local LiDAR movement. In the research by M. Grafe [21] the numerical model is used to verify the analytical results, while in this research the numerical model is the basis for obtaining corrected measurements of velocities and uncertainties. That can then be used to correct real time measurement form the LiDAR on the TetraSpar. Verification is done by reconstructing the wind field and comparing it with the input wind field.

1.2. Research questions

From the previous discussion, it should be clear what the relevance is of correcting wind velocity measurements on floating wind turbines and knowing the uncertainty of these corrections. With this application, wind fields can be reconstructed with higher accuracy, opening up possibilities for load verification, in-the-loop control and for better power curve calculations.

This master thesis fits into the current research by considering a nacelle-based LiDAR, which experiences motions different from those of a floating buoy. While floating buoy LiDARs have been researched and used more extensively for resource assessment and wind measurements in active wind farms, nacelle-based LiDARs on a floating wind turbine are relatively unexplored.

Besides, this is the first application in which this particular correction approach has been established. In this approach, a correction is determined through a numerical LiDAR model that incorporates a 6 DOF input for the LiDAR motion caused by wave-induced motions of the floating turbine.

Additionally, the development of a LiDAR model is relevant for SGRE, since a new model needs to be created. This new model is required to be independent of existing models, such as 'Virtual Constrained turbulence and LiDAR measurements' (ViConDar), developed by [36]. The reason for this is that it must be integrated into the aero-hydro-elastic model: BHawC-Orcaflex, where BHawC is developed in-house at SGRE.

All in all, these aspects create a clear research gap with the research objective of developing a correction method for the influence of floater motions on LiDAR wind speed measurements by simulating a LiDAR. For this corrected wind velocity, the uncertainty also has to be known in order to know to what extent the wind measurement can be trusted and used. Therefore, the following question will be answered in this thesis:

Main question

What are the uncertainties in corrected wind speed measurements taken from a nacelle-mounted LiDAR on a floating wind turbine?

Sub-questions

1. How is the correction of a wind velocity LiDAR measurement on a floating wind turbine performed with the use of a numerical LiDAR model?
2. What are the specific floater motions that influence LiDAR wind speed measurements and how significant is their impact?
3. What are the uncertainties of the involved input parameters, that is, of the LiDAR parameters, the LiDAR modelling and the motion input?
4. What is the most dominant source of error in the reconstructed wind field?
5. What is the remaining error of the corrected wind speed measurements?

1.3. Report Outline

In this thesis, the relevant theory required is first given to understand the methods applied. This is done in chapter 2. A general overview of the research structure is first given. Then the different steps that are detailed in this overview are expanded on, such as the floater motions, LiDAR measurements and reconstruction. In addition, uncertainty quantification and test case set-up are discussed. In the next chapter, in chapter 3 the methodology applied to correct LiDAR measurements is described. Again going over the separate components of the research structure, starting with the inputs, then focussing on the LiDAR model itself and then discussing the generation of the outputs, going on to the reconstruction method of the original wind field. The results of the correction method are presented in chapter 4. Here, first focus is again put on the different components of the correction method, that is, the motion, the LiDAR model and the reconstruction. After that, the total uncertainty of the reconstructed wind field is discussed. Lastly, the main conclusions that can be drawn from these results and answer the research questions are given in chapter 5. In addition, recommendations for future work are given here.

2

Background theory

2.1. General overview

How are LiDAR measurements corrected for motions in floating offshore wind turbines? To answer this question, the design of the correction method for the movement of the LiDAR in the LiDAR model will be explained by means of Figure 2.1.

The measurement that the LiDAR performs is modelled as a LiDAR simulator. The simulator requires inputs for both the movement of the LiDAR, influenced by its floating motion, and the wind field that it is measuring. These inputs are represented by two blocks on the left side of Figure 2.1, labelled '*floating motion*' and '*wind field*'.

The LiDAR model generates three key outputs: the line of sight velocity along the laser beam's direction, the measurement position of this velocity, and the direction vector from the LiDAR to the measurement position. These outputs are shown as three blocks to the right of the '*LiDAR model*' in the figure, labelled '*Line of Sight Velocity (VLOS)*', '*position*', and '*direction*'. All three outputs are corrected for the motion of the turbine within the LiDAR model.

The corrected outputs—line-of-sight velocity, measurement position, and direction—are then input into a reconstruction algorithm to retrieve the original wind field. This process, shown in the block labelled '*reconstruction*' to the far right of the figure, serves as a verification step for the LiDAR model. The reconstructed wind field should closely match the original wind field input.

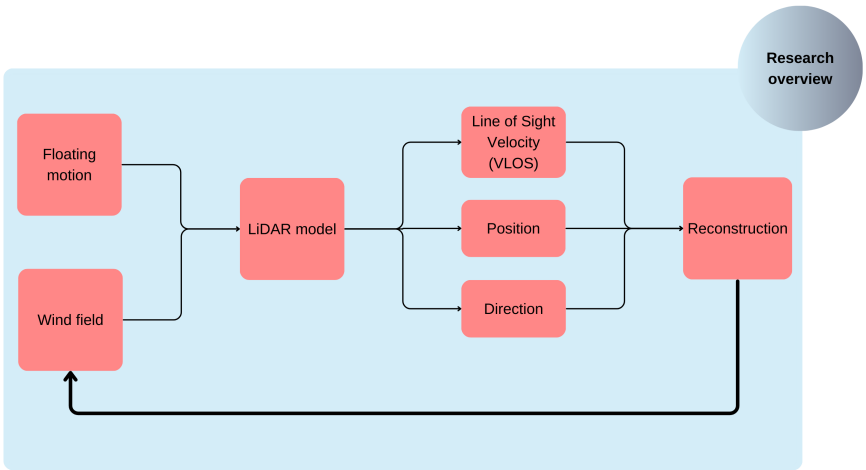

Figure 2.1: Overview of research set up

Uncertainties are present in the input of the motion data. These uncertainties propagate through the LiDAR model and result in uncertainties in line of sight velocity V_{LOS}, measurement position and direction. However, also the LiDAR simulator itself has uncertainties in its modelling that add to the total uncertainty of the output. These output uncertainties again result in uncertainties in the reconstructed wind field. The goal of this research is to get corrected outputs and quantify their uncertainties and error with respect to the original wind field.

In the next sections, the different details of the steps in the general overview will be described in more detail. Diving into the motions of a FOWT, the input wind field, the LiDAR model itself and the reconstruction algorithm. In addition to some relevant steps in between, such as the uncertainty quantification, coordinate transformations and the set up of the floating wind turbine demonstrator that gathers the relevant data.

2.2. FOWT motions

Knowing how a moving FOWT can be described is an essential step to identify the floating motion input of the research overview given in section 2.1. This section explains the movement of a floating wind turbine and describes in a very general way what causes these motions.

The simplified motion of a FOWT is defined in 6 DOFs. A rigid body motion is considered for the motions of the floater, ignoring deformations of the body itself. The translational motions are described as surge, sway, and heave, and the rotational motions are described as roll (φ_{Roll}), pitch (θ_{pitch}) and yaw (ψ_{yaw}). These angles should not be confused with blade pitching and nacelle yaw. The conventional directions in which these are defined are described in Figure 2.2. For the simulated motions on the top of the tower, where the LiDAR is located, some tower deformations will also be considered. This is further explained in the Methodologies chapter in subsection 3.1.1.

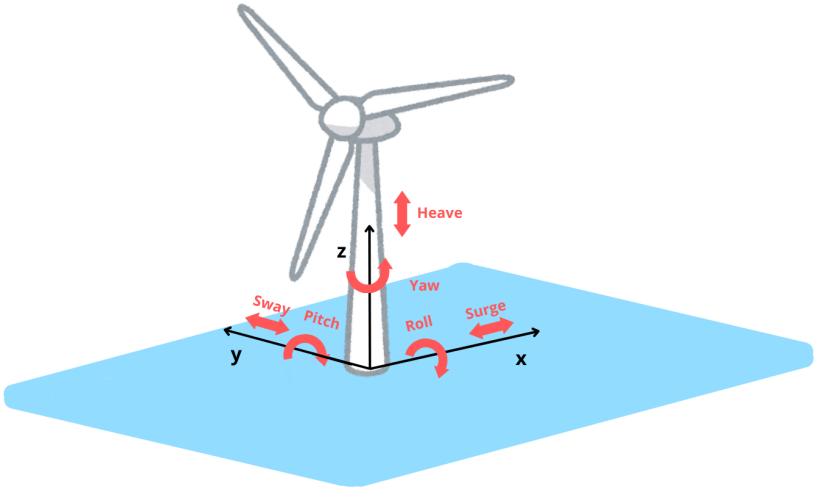

Figure 2.2: Convention of describing floater motions of a floating offshore wind turbine

The movement of the turbine depends on the sea state in which it is situated, that is, the wave height and wave period, but also the structure's geometry and stiffness, the water depth, etc. On top of that, the wind also has a high influence on the movement of a floating wind turbine, mostly contributing to a static pitch offset from zero. Floater motions that are induced by waves can be divided into three different categories, namely: wave frequency, high frequency and slow drift or mean drift motions. The latter motions are caused by non-linear waves, due to the difference in frequency contributions [31] and mostly contribute to resonance in surge, sway and yaw. The first category is associated with the wave frequency range. In turn, the second category is mostly associated with frequencies higher than the wave frequency, and these high frequency motions are connected to resonance in heave, pitch and roll.

2.2.1. Floater dependency

Floating wind turbines are much more influenced by hydrodynamic loads, compared to bottom fixed offshore turbines. The severity of the influence of hydrodynamic loads on the turbine's motion depends on the floater design. As the industry has not converged yet to one design, the influence of choosing a specific design on the turbine's and thus the LiDAR's motion should be taken into account when looking at the relevant floater motions. The Tetraspar uses a spar buoy floater design. This design will most likely experience less high wave loading compared with semi-submersible floater designs. However, it will still experience non linear wave forces and is sensitive to rotational motions. The tension leg platform (TLP) will have even smaller tower top motions because it will only experience small wave-induced motions [5]. The higher wave loading will increase the response of the system, and thus result in large relative motions of the nacelle-mounted LiDAR. These dependencies, that is, the magnitudes and periods of the motions studied, should be taken into account when conclusions are drawn for corrections. The magnitude of the error and uncertainty values connected to the influence of different degrees of freedom might differ for other floater designs. This is true because the magnitudes and periods of the dominating motions for these designs will be different.

2.3. Wind field

The wind field that is input can be modelled in multiple ways. The simplest way would be to use the same wind field for every measured location. Often to include a more realistic wind model a theoretically derived log law or an empirically derived power law is used to describe the wind shear that is created by friction with the ground, or in this case, the sea surface. In the IEC standard [3] both equations to describe wind shear are used and for this thesis the power law is chosen, which is described in (2.1). An example is plotted in Figure 2.3, with $U_{ref} = 10m/s$, $z_{ref} = 90m$ and $\alpha = \frac{1}{7}$.

$$U(z) = U_{ref} \left(\frac{z}{z_{hub}} \right)^{\alpha} \tag{2.1}$$

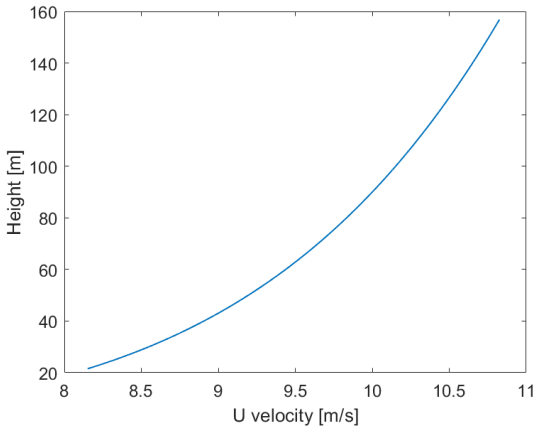

Figure 2.3: Power law wind profile with $U_{ref} = 10m/s$ and $\alpha = 1/7$

2.4. LiDAR wind measurement

The foundation that this research is based on is the LiDAR model. This section explains the working principle of a LiDAR which is essential to correct its measurements. Next to the physical principles of the LiDAR, the modelling of the LiDAR is clarified. This model will be directly applied to perform corrections, with uncertainty propagated through it.

2.4.1. Working principle

Light detection and ranging (LiDAR) measurements use laser light and the Doppler shift caused by reflection of the electromagnetic wave on air molecules and aerosols to measure wind speed. This application is also called Doppler Wind LiDAR or DWL in short. A projection of the wind vector is measured along the path of the laser beam. In this research the application of the coherent wave LiDAR is used as opposed to a direct detection LiDAR, which uses a broadband Rayleigh signal with light reflections of off molecules, and is usually used in higher parts of the atmosphere where aerosols and cloud particles are less common [38], [43].

Doppler effect

The Doppler effect occurs if the source that emits light and the observer that receives light move relative to each other. In the case of LiDAR, the source, the moving aerosols, move relative to the LiDAR that emits the laser light. In the case of a floating LiDAR the observer adds another relative motion to this as the LiDAR moves due to the floating motion. Only when the speed of the observer or LiDAR would be close to that of the speed of light, should the complete relativistic Doppler effect be considered.

If the relative speed between LiDAR and particle is described as $\Delta \mathrm{v}$, the frequency of light transmitted by the LiDAR is set to f_0 and the frequency observed by the particle is set to f_1, then f_1 can be described according to (2.2). In this equation c describes the speed of light.

$$f_1 = f_0 \cdot \left(1 + \frac{\Delta \mathrm{v}}{c}\right) \tag{2.2}$$

Here, $\Delta \mathrm{v}$ is described by (2.3).

$$\Delta \mathrm{v} = \mathrm{v_p} - \mathrm{v_L} \tag{2.3}$$

With $\mathrm{v_p}$ describing the speed of the particle and $\mathrm{v_L}$ describing the speed of the LiDAR.

Then the observed frequency f_2, which is received by the LiDAR and scattered back from the particle as f_1 is described by (2.4). Here, the term $(\frac{\mathrm{v_p}}{c})^2$ is neglected as it is much smaller than the other two terms present.

$$f_2 = f_1 \cdot \left(1 + \frac{\Delta \mathrm{v}}{c}\right) \approx f_0 \cdot \left(1 + 2 \cdot \frac{\Delta \mathrm{v}}{c}\right) \tag{2.4}$$

Now, the final difference frequency that should be detected is given by (2.5), thus describing the Doppler shift frequency.

The relative Doppler shift $\Delta f / f_0$ is usually very small and its order of magnitude is commonly between micro and nano Hz, which is very hard to detect [38].

$$\Delta f = f_2 - f_0 = 2 \cdot f_0 \cdot \frac{\Delta \mathrm{v}}{c} \tag{2.5}$$

Spectral line shape

The concept of wind can be described by the collective movement of particles in the air within a particular volume in the atmosphere. These particles can be molecules, aerosols or cloud particles. On top of this movement, there acts a so-called Doppler broadening that is caused by the movement of the individual air particles. This causes a variance to be present in the measured wavelength or frequency shift.

The spectral distribution commonly looks as depicted in Figure 2.4. This figure shows the spectral distribution for an emitted wavelength of $355nm$. On the axis of the graph, the Doppler shift is shown for the wavelength change in $pm(1pm = 10^{-12}m)$, and V_{LOS} in m/s, where a $1pm$ difference in $\Delta\lambda$ is equal to a $422m/s$ change in V_{LOS}. In the graph also the full-width half-maximum is indicated with FWHM.

The broad variance (σ_v) seen in the signal is caused by the light that is back-scattered by molecules. These are very light and have a relatively high speed. Air molecules namely have a mean velocity of $459\ m/s$ at a temperature of $15°$ [38]. For aerosols, the variance in the spectral distribution is much smaller as these are much heavier compared to air modules. In the application for relatively local wind measurements with coherent LiDARs on earth, aerosols are used only.

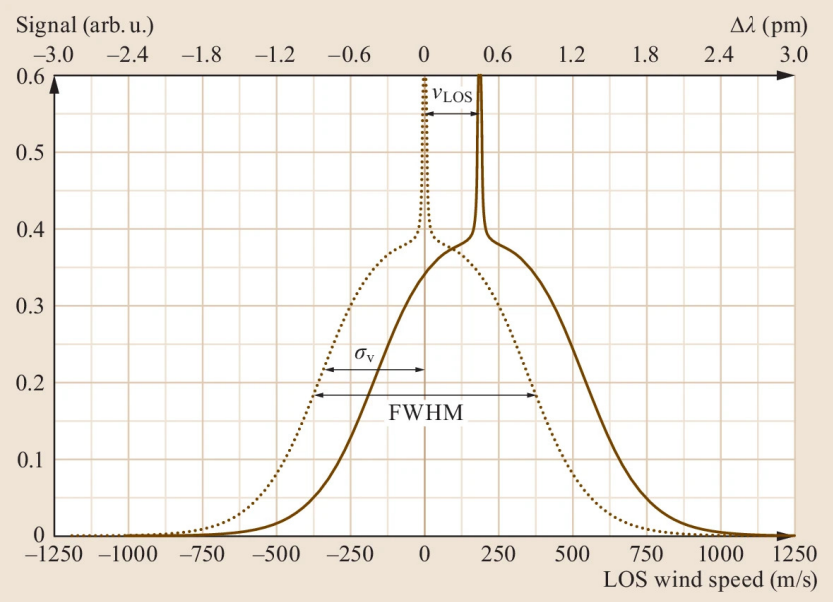

Figure 2.4: Spectral distribution of V_{LOS}, where a mean V_{LOS} of $0m/s$ is depicted by the dotted line and a V_{LOS} of $180m/s$ is depicted by the bold line. [39]

Finally, the goal is to find the mean of the spectral distribution to quantify the Doppler shift and find the line of sight velocity.

Coherent detection Doppler Wind LiDAR

As discussed in the first section of subsection 2.4.1 on the Doppler effect, the change in relative frequency due to the Doppler shift is very small, requires incredibly sensitive measurement material and would be extremely sensitive to disturbances. To solve this issue, a reference signal is used. Another light beam is emitted that will interfere with the received signal. The frequency of the reference signal will be subtracted from the received signal. This is shown in the schematic below in Figure 2.5. This type of LiDAR is called coherent because of the additional coherent laser beam that is added as part of the detection of the Doppler shift. However, in fact, all LiDARs make use of coherent lasers, as opposed to incoherent light. This additional electromagnetic light wave has frequency f_{LO}, where LO signifies local oscillator.

As described in [38], the detector registers the current induced by the time-averaged square of the electrical field of the combined and the reference signal. Here, the electrical field of the different signals is described by (2.6), which corresponds to the sinusoidal solution of the electromagnetic wave equation. The subscript s describes the atmospheric source signal and thus $f_s = f_2 = f_0 + \Delta f$. Each electric field of the electromagnetic waves has a corresponding frequency and phase.

$$\begin{aligned} E_S(t) &= \bar{E}_S \cdot \cos\left(2\pi \cdot f_s \cdot t + \varphi_S\right) \\ E_{LO}(t) &= \bar{E}_{LO} \cdot \cos\left(2\pi \cdot f_{LO} \cdot t\right) \\ E_D(t) = E_S(t) + E_{LO}(t) &= \bar{E}_S \cdot \cos\left(2\pi \cdot f_s \cdot t + \varphi_S\right) + \bar{E}_{LO} \cdot \cos\left(2\pi \cdot f_{LO} \cdot t\right) \end{aligned} \tag{2.6}$$

Here, the magnitudes of the electrical field can be determined from the LiDAR equation, given in (2.7) from [48]. This equation gives the power of the received signal depending on the LiDAR parameters. The power of the local oscillator signal is known and constant.

$$P(r) = KG(r)\beta(r)T(r) \tag{2.7}$$

As described in [48], the first two terms describe the setup of the LiDAR, while the last two summarise the information from the atmosphere. The first component of the LiDAR equation K describes the performance of the LiDAR system itself. Then $G(r)$ contains a description of the measurement geometry that depends on the range. For the atmosphere, $\beta(r)$ identifies the backscatter for a distance r and $T(r)$ stands for transmission, indicating the amount of light that is lost while the light travels through the atmosphere.

The laser photon detector receives a current that is proportional to the light intensity. The light intensity is proportional to the square of the electrical field of the combined signal and the reference signal E_D. What this looks like is shown in (2.8), also retrieved from [38]. The last term in the second equation of (2.8) is zero as the frequency of this term is much higher than the bandwidth of the detector. This also holds for the direct current terms that correspond to the first two terms in I_D, they contain twice the beam frequencies ($4\pi f_{LO}$ and $4\pi f_s$). Therefore, only the beat frequency is recorded.

The efficiency η_{eff} that is placed in (2.8) describes the optical mixing efficiency. This parameter shows the spatial inference of the s and LO beams and their temporal correlation. For perfect coherent beams, η_{eff} would be 1. It describes the efficiency of the mode matching of the two beams. In this way, non-coherent background noise is also filtered out, which would have a low η_{eff}.

$$\begin{aligned} I_D(t) &\propto \overline{|E_D(t)|^2} \\ I_D(t) &\propto \frac{1}{2}\bar{E}_S^2 + \frac{1}{2}\bar{E}_{LO}^2 + \eta_{eff}\bar{E}_S\bar{E}_{LO} \\ &\quad \overline{[\cos\left(2\pi \cdot (f_S - f_{LO}) \cdot t + \varphi_S\right)} + \underbrace{\overline{\cos\left(2\pi \cdot (f_S + f_{LO}) \cdot t + \varphi_S\right)}}_{=0}] \\ I_D(t) &\propto \frac{1}{2}\bar{E}_S^2 + \frac{1}{2}\bar{E}_{LO}^2 + \eta_{eff}\bar{E}_S\bar{E}_{LO}\cos\left(2\pi \cdot (f_S - f_{LO}) \cdot t + \varphi_S\right) \end{aligned} \tag{2.8}$$

With the use of time-averaging, only the frequency difference between the received signal f_2 and the local oscillator signal f_{LO} is recorded, this is called the beat-frequency, as shown in (2.9). It is heterodyne if $f_{LO} \neq f_0$.

$$f_{\text{beat, heterodyne}} = |f_2 - f_{LO}| = |f_0 + \Delta f - f_{LO}| \tag{2.9}$$

(2.10) relates the LiDAR equation for power to the detected current and is retrieved from [30]. A similar equation is also given in [49]. The power received $P_{s,i}$ can be described by the LiDAR equation in (2.7).

(2.10) is the same equation as (2.8), but with the magnitude of the electric field replaced by the power of the electric field and the power received by each particle is specified as $P_{s,i}$ and summed for the measurement volume. Besides that, η_{rec} is the receiver loss and gain factor, F_i is the collection efficiency of the scatter from particle i and R_{diode} is the responsivity of the detector.

$$i_D(t) = 2R_{\text{diode}} \sum_V \sqrt{\eta_{rec} F_i P_{s,i} P_{LO}} \cos\left(2\pi \left(f_{s,i} - f_{LO}\right) t + \varphi_s\right) + D_{DC} \tag{2.10}$$

The (2.11) shows the exact and not proportional relationship of the current described in terms of the magnitude of the electrical field of (2.8). In this equation c is the speed of light and ε_0 is the permittivity in vacuum.

$$i_D(t) = \eta_{eff} \frac{\bar{E}_s \bar{E}_{LO} \cos\left(2\pi \left(f_s - f_{LO}\right) t + \varphi_s\right)}{c\varepsilon_0} + D_{DC} \tag{2.11}$$

Here, D_{DC} describes the direct current according to (2.12).

$$D_{DC} = \eta_{eff} \frac{\bar{E}_s^2 + \bar{E}_{LO}^2}{2c\varepsilon_0} \tag{2.12}$$

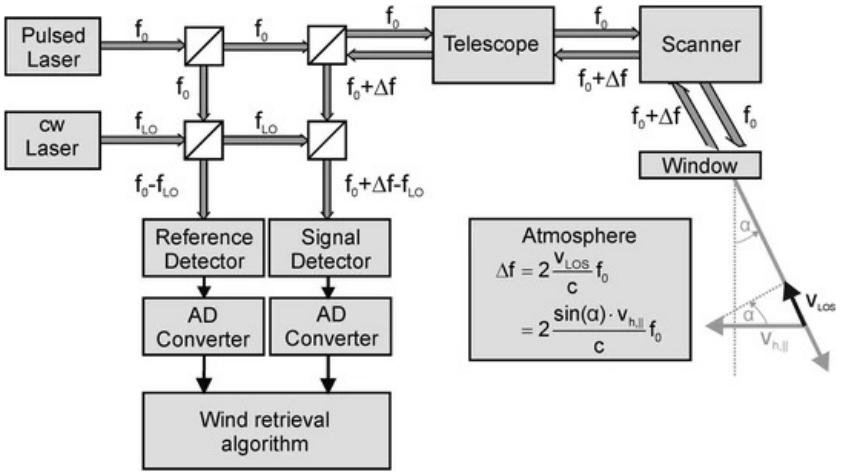

Figure 2.5: Schematic overview of working principle of a coherent heterodyne Doppler Wind LiDAR [38]

Signal processing

Once the signal has been received by the detector, it is converted to a digitised signal and a direct Fourier transform is applied to obtain the power spectral density of the received signals. This signal is then averaged for several time blocks to filter out noise. For the same purpose, a threshold is applied to the data. Consequently, a mean of the Doppler shift can be found, and from this the relative wind speed is calculated. All of this is visualised in Figure 2.6.

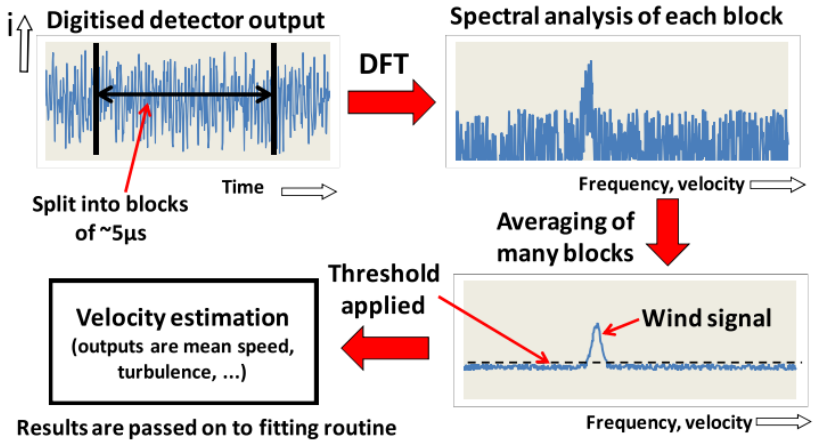

Figure 2.6: Signal processing of LiDAR detection retrieved from [43]

Line of sight velocity
The velocity measured by one laser beam of the LiDAR is not the real wind speed vector, but the wind speed along the direction the laser beam points in. This velocity is called the line of sight (LOS) velocity and is shown in (2.13).

$$V_{LOS} = \vec{V} \cdot \vec{d_n} = u\cos(\theta) + v\sin(\theta)\sin(\psi) - w\sin(\theta)\cos(\psi) \tag{2.13}$$

In this equation, $\vec{V}$ is the wind speed vector, $\vec{d_n}$ is the direction vector of the LiDAR laser beam, u, v and w are the wind speeds in x, y and z directions. In Figure 2.7 the measurement principle is shown with the conventional coordinate system for the nacelle-based LiDAR. The LiDAR points towards the main wind direction in u. In addition, the direction in which the laser beam points is indicated with the zenith angle θ and the azimuth angle ψ, as shown in Figure 2.7. These angles correspond to the angles in (2.13). The parameter F describes the position of the range gate. In the figure a scanning LiDAR is used, while in this research a fixed LiDAR is used measuring with four non-scanning LiDAR beams as depicted in Figure 2.8.

In the case of the floating LiDAR the measurement device itself also has a movement and so in fact it does not measure wind speed of the wind field directly, but rather calculates the relative speed compared to its own movement. Therefore, in this research (2.14) is considered. In section 2.5 the inclusion of the LiDAR movement and the transformations that accompany it will be discussed in more detail.

$$\begin{aligned} V_{LOS} = (\vec{V} - \vec{V}_{LiDAR}) \cdot \vec{d_n} = \\ (u - \dot{x}_{LiDAR})\cos(\theta) + (v - \dot{y}_{LiDAR})\sin(\theta)\sin(\psi) - (w - \dot{z}_{LiDAR})\sin(\theta)\cos(\psi) \end{aligned} \tag{2.14}$$

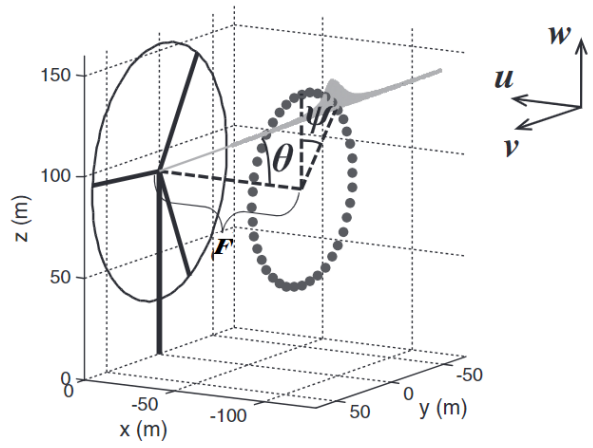

Figure 2.7: Description of LiDAR measurement, here a scanning pattern is visualised. Retrieved from [42].

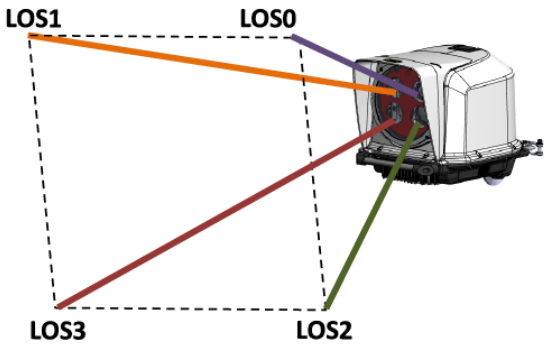

Figure 2.8: Leosphere Windcube with 4 pulsed laser beams, retrieved from the user manual [6]

2.4.2. Modelling of LiDAR
Now that the principles of LiDAR measurement are clear, the LiDAR model that will be programmed to correct the measurements can be described in detail.

Point measurement
The LiDAR can be simplified in a model by simulating it as a point measurement. The assumption would be that the LiDAR focusses on one point in space (or a range of points), which has a certain radial velocity along the beam. One then assumes that one particle is present at exactly the measurement point that gives the local line of sight velocity. This simplification is useful for gaining a basic understanding as well as for the use of a test case of the more complex LiDAR model. The equation connecting the line of sight velocity and the wind speed, given in section 2.4.1 as (2.14) can directly be used.

Volume measurement
In reality, the wind speed is not measured for one single particle at which the laser is pointed, but rather for a number of particles enclosed in a measurement volume that the laser illuminates. This is also shown in the spectral line shape shown in section 2.4.1, with Figure 2.4, for example.

The laser beam is modelled as a thin beam, since the width of the beam is very small compared to the length along the pointing direction of the beam. Then the wind speeds of the particles are integrated over an enclosed volume with a weighting function $W(r, z)$ according to (2.15). In the following, the derivation of this weighting function and its connection to the working principle of a LiDAR is discussed. In addition, in subsection 3.3.3 the practical implementation of (2.15) as a quadrature is discussed.

$$V_{LOS} = \int_0^\infty \int_0^\infty ((\vec{V}(r) - \vec{V}_{LiDAR}) \cdot \vec{d}_n)\, W(r, z) dr dz \tag{2.15}$$

The received electrical field as described in (2.6) is now modelled as a Gaussian beam and is depicted in Figure 2.9. A Gaussian beam describes the first mode of the transverse electromagnetic modes (TEM) as a solution of the paraxial Helmhotz equation. This is firstly an idealisation because only the first TEM mode is considered, while in reality more modes should be present to model reality better. In addition, in the paraxial approximation, it is assumed that the envelope of a forward-travelling wave pulse varies slowly in time and space compared to its period or wavelength. That implies that the beam waist is relatively large and the beam divergence small enough for this assumption to apply. Thus, if the beam is very focused, which implies a small w_0, the paraxial assumption no longer holds. The beam waist in Figure 2.9 is exaggerated from reality for visualisation purposes. These assumptions can induce uncertainties in the modelling and thus in the final correction factor for the measured wind speed. For example, to increase accuracy of the model, more TEM modes could be included. It is namely unlikely that the laser beam only makes use of the Gaussian beam, more realistically other modes will be present at the same time. The TEM modes and the corresponding magnitudes that are present depend on the laser resonator. The LiDAR manufacturer could be contacted to ask for the most dominant modes in the laser.

The electrical field for a Gaussian beam is given in (2.16) from [40].

$$E(r, z) = E_0 \frac{w_0}{w(z)} \exp\left(-\frac{r^2}{w(z)^2}\right) \exp\left(i\left[kz - \arctan\left(\frac{z}{z_R}\right) + \frac{kr^2}{2R(z)}\right]\right) \tag{2.16}$$

The phase of the Gaussian beam is described by (2.17) from [40], where the first term represents the phase of a plane wave. The second term is the Gouy phase shift, which represents an extra delay of the wavefront compared to plane waves because of the confinement of the beam in spatial directions. The effect is largest near the focal point. The third term is connected to wavefront bending, and is connected to a deviation of the phase of on-axis points, so when $r \neq 0$.

$$\varphi(r, z) = kz - \arctan\left(\frac{z}{z_R}\right) + \frac{kr^2}{2R(z)} \tag{2.17}$$

The other parameters of (2.16) are described in the list below.

- E_0 = peak amplitude at the origin where $r = 0$ and $z = 0$
- w_0 = beam waist (see Figure 2.9)
- $w(z)$ = the beam radius where the intensity lowers to $1/e^2$ or the the magnitude of the electrical field drops to $1/e$ due to diffraction of light, which is calculated as:

$$w(z) = w_0 \sqrt{1 + \left(\frac{z}{z_R}\right)^2} \tag{2.18}$$

- r = the radial distance from the central z-axis of the beam (in the x-y-plane).

$$r = \sqrt{x^2 + y^2} \tag{2.19}$$

- k = wave number
- z_R = Rayleigh length , indicating the distance at which the area of the beam waist has doubled, thus the waist is increased with a factor $\sqrt{2}$, as indicated in Figure 2.9.

$$z_R = \frac{\pi\ w_0^2}{\lambda} \tag{2.20}$$

- $R(z)$ = radius of curvature of the wave fronts

$$R(z) = z + \frac{{z_R}^2}{z} \tag{2.21}$$

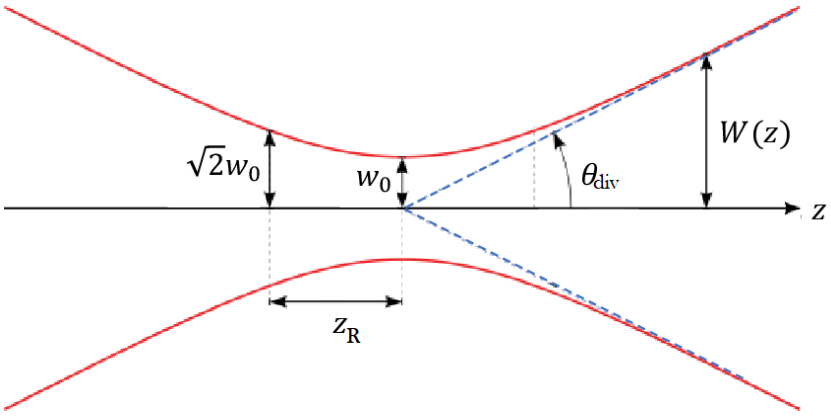

Figure 2.9: Gaussian beam geometry retrieved from [10].

Next to the beam properties close to the waist, the beam divergence in the far field, that is for z values much larger than z_R is described according to (2.22) from [40].

$$\theta_{div} = \frac{\lambda}{\pi w_0} \tag{2.22}$$

Now in the same way as described in (2.6), the intensity or received current is proportional to the square of the magnitude of the electrical field, which in turn is proportional to the power of the signal. Finally, the intensity of the Gaussian beam can be written as (2.23) from [40].

$$I(r,z) = \frac{2\ P}{\pi\ w(z)^2}\ \exp\left\{\left(-2\frac{r^2}{w(z)^2}\right)\right\} \tag{2.23}$$

Here, P is the total power of the beam. For a perfect Gaussian beam, P is the peak irradiance.

Knowing how to model the light intensity of the laser beam of the LiDAR is useful so that the velocity of the particles that scatter light can be weighted with the received light intensity. This weighting function is found using the normalised version of (2.23). For this, the following definition of total power is used as in (2.24) from [22], with I_0 the peak light intensity. If now the light intensity is assumed to be $I_0 = \frac{1}{\pi z_R}$, then (2.23) can be rewritten as (2.25). Now, a multiplication of a Lorentzian profile along the z-axis of the beam and a Gaussian profile along the radial axes of the beam is produced. In this way, there is no need to know the power nor the peak irradiance of the LiDAR pulse. This normalisation is allowed, because for the final calculations normalised weights are required to avoid dependency on the number of particles. Now (2.25) is only a function of the coordinate parameters x, y, z and the Rayleigh length z_R.

$$P = \frac{\pi w_0^2}{2} I_0 \tag{2.24}$$

$$W_{GaussianBeam} = \frac{z_R}{\pi(z^2 + z_R^2)} \exp\left\{\left(-2\frac{r^2}{w(z)^2}\right)\right\} \tag{2.25}$$

Now that the weighting for the particles in the measurement volume is known, one can model which particle's velocity will contribute more to the final measurement of V_{LOS}. This is done with a convolution integral. The interaction of the input: the physical property of the speed of the particle, with the system: the laser beam, is represented by this convolution integral. The light intensity of the Gaussian beam is incorporated in the weighting function of the convolution integral that is described at the beginning of this section in (2.15).

Pulsed LiDAR

Within the Doppler wind LiDARs, there exist continuous wave (CW) and pulsed LiDARs. The Tetraspar has a pulsed LiDAR installed, so the focus in this report will be on the pulsed LiDAR. A continuous wave LiDAR focusses on one spatial point, or volume, and measures the wind speed for that position. Instead, a pulsed LiDAR can measure at several distances by sending out pulsed laser signals. In this way a more complete image of the wind field is registered, but with the disadvantage that the measurement is integrated over a larger time span, in order to guarantee a good signal-to-noise ratio (SNR).

Now, the weighting function of (2.15) consists of the Gaussian intensity along the axial direction of the laser beam, as well as a range gate weighting function (RWF), which describes the pulsed laser measuring at different range gates. These two weights that describe the total weight for the convolution integral to find V_{LOS} in (2.15), are defined in (2.26).

$$W(r, z, F) = W_{GaussianBeam}(x, y, z)W_{RWF}(z, F) \tag{2.26}$$

In this section, the range gate weighting function W_{RWF} will be explained.

The W_{RWF} is a convolution of the pulse power profile and a measurement window. Now, under the simplifying assumption of a Gaussian for the pulse shape as described in (2.27) and a rectangular windowing function, (2.30) is produced. This equation has first been derived by [2] and has been used in multiple sources in literature, such as [15], [33], [42].

$$I_n(F, z) = \frac{1}{\sqrt{\pi} r_p} \exp\left(-\frac{(F - z)^2}{r_p^2}\right) \tag{2.27}$$

In this equation r_p is the half width of the pulse, represented by (2.28). The variable Δr is the full width at half maximum (FWHM) of the pulse width, described by (2.29) [15], for which τ_p is the pulse $1/e$ width [14].

$$r_p = \frac{\Delta r}{2\sqrt{\ln(2)}} \tag{2.28}$$

$$\Delta r = \sqrt{\ln(2)} c \tau_p \tag{2.29}$$

With this, the weight ranging function is defined as an integration of the intensity over the range gate range, with Δp the length of the range gate, found with $\frac{\Delta t_{\text{obs}} c}{2}$, with Δt_{obs} the total observation time [33].

$$W_{RWF}(F, z) = \frac{1}{\Delta p} \int_{-\frac{\Delta p}{2}}^{+\frac{\Delta p}{2}} I_n(F, z + s) ds \tag{2.30}$$

In turn, this integral can be solved analytically with the Erf function, as described in (2.31).

$$W_{RWF}(F,z) = \frac{1}{2\Delta p}\left[Erf\left(\frac{z-F+\frac{\Delta p}{2}}{r_p}\right) - Erf\left(\frac{z-F-\frac{\Delta p}{2}}{r_p}\right)\right] \tag{2.31}$$

Here, the error function is used for integrating normal functions and looks like (2.32).

$$Erf(z) = \frac{2}{\sqrt{\pi}}\int_0^z e^{-t^2}dt \tag{2.32}$$

In summary, to model the LiDAR all required inputs repeated in the following have to be present. All relevant LiDAR parameters have to be known, that is, the range gate length (Δp), the range gate locations (F) and the half width of the pulse (r_p). In addition, a wind field should be simulated. Moreover, a point cloud of particles with their respective wind speeds has to be created. For the moving LiDAR the translational and rotational movements are also required. The real application of the weighting functions is discussed in chapter 3 and, more specifically, in subsection 3.2.3.

2.5. Transformation from LiDAR to global coordinate frame

What makes this model different from the majority of existing LiDAR models is the movement of the LiDAR. One of the problems that floating motion brings is the use of different coordinate systems and the transformations required that will map one location or velocity to the other. In this section, these different transformations will be discussed.

2.5.1. Definition of reference frames

Three major reference frames exist: that of the laser beam, as described in the Gaussian beam model, that of the LiDAR and an inertial reference frame. First, the convention of these three will be explained, then the transformation between them, and then the necessary operations on the input variables will be given in terms of transformations to arrive at the desired outputs.

Firstly, the inertial reference frame is defined as a global Earth-centered, Earth-fixed (ECEF) reference frame or Terrestrial Reference System (TRS). This frame has its origin at Earth's centre of mass and the z-axis is defined towards the Conventional Terrestrial Pole (CTP), the average of the poles from 1900 to 1905. Then the y-axis is directed towards the intersection of the mean Greenwich meridian and the equator. The y-axis is then perpendicular to this. All this is retrieved from [45] and visualised in Figure 2.10.

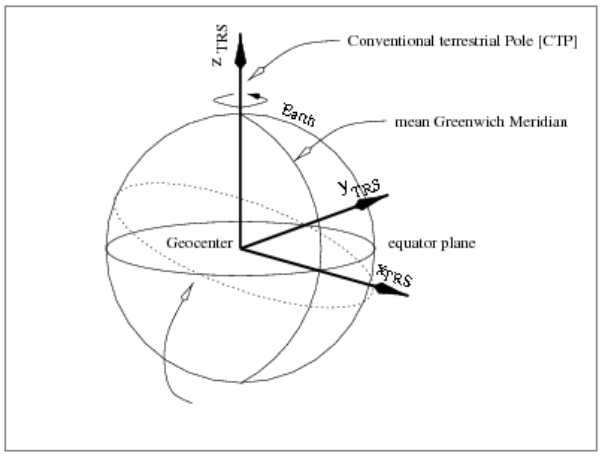

Figure 2.10: Terrestrial reference system from [45]

Next, if we would call the TRS the inertial frame, even though it moves with the Earth's rotation, then the LiDAR reference frame is defined as in Figure 2.11. The TRS will now be called the inertial frame and will be indicated as $\mathcal{I}$, while the LiDAR frame will be indicated as $\mathcal{L}$.

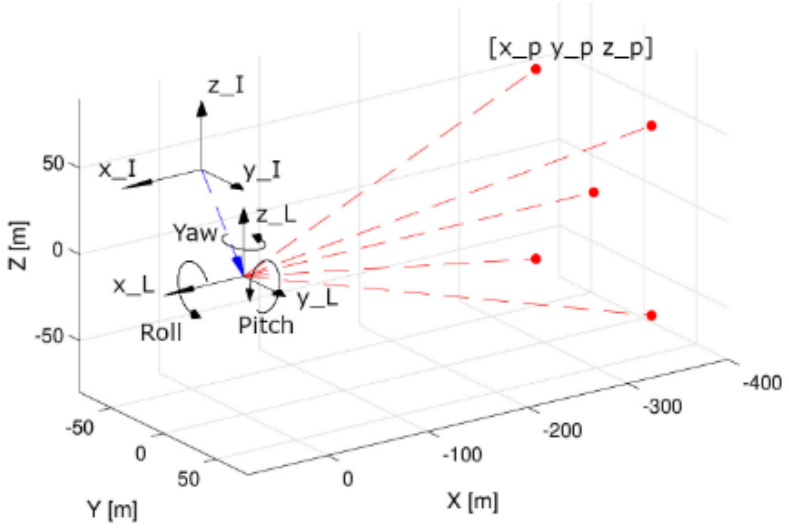

Figure 2.11: Definition of the LiDAR reference frame, defined in the inertial reference frame (TRS), from [20]

In the figure the angles ψ_{yaw}, θ_{pitch} and φ_{roll} represent the yaw, pitch and roll angles, relatively. The LiDAR position with the coordinates $x_{L,\mathcal{I}}$, $y_{L,\mathcal{I}}$ and $z_{L,\mathcal{I}}$ is taken from either a simulation or the IMU, as described in section 2.2. In this thesis, finally, not the inertial reference frame as described here is used, but a global reference frame centred at the original position of the turbine tower bottom as described later in subsection 3.2.1.

2.5.2. Transformations

There are two major transformations for this problem. That is, a transformation from the beam coordinate system to the LiDAR and that from the LiDAR to a global reference frame. These reference frames are described later in subsection 3.2.1. The wind field as input for the LiDAR model will be given in the global reference frame, as will the movement of the wind turbine.

LiDAR to global

The normalised direction vector that points in the direction of the laser beam is described as (2.33), which is derived from (2.13) and for which the angles are described in Figure 2.7.

$$\vec{d}_n = \begin{bmatrix} -\cos(\theta) \\ -\sin(\theta)\sin(\psi) \\ \sin(\theta)\cos(\psi) \end{bmatrix} \tag{2.33}$$

Then the point of measurement, that is, the location where one V_{LOS} is found, is defined as (2.34). Here, F is the distance along the beam from the origin of the LiDAR reference frame to the centre of the range gate, as used in the pulsed LiDAR weight ranging equation and described in Figure 2.7.

$$\vec{r}_p = \begin{bmatrix} x_p \\ y_p \\ z_p \end{bmatrix}_{\mathcal{L}} = F\vec{d}_n = F \begin{bmatrix} -\cos(\theta) \\ -\sin(\theta)\sin(\psi) \\ \sin(\theta)\cos(\psi) \end{bmatrix} \tag{2.34}$$

These measurement positions need to be known in the inertial reference frame in order to connect a wind speed to these positions. Then the following transformation is applied, as shown in (2.35).

$$\vec{r}_{p,\mathcal{I}}(t) = \vec{r}_{\text{LiDAR},\mathcal{I}}(t) + \mathbf{R}(q_{\text{LiDAR}}(t))\ \vec{r}_{p,i,\mathcal{L}} \tag{2.35}$$

To shorten the formula, the time dependency can be left out of the equation, but not forgetting that the first three parameters are, in fact, time dependent, resulting in (2.36).

$$\vec{r}_{p,\mathcal{I}} = \vec{r}_{\text{LiDAR},\mathcal{I}} + \mathbf{R}(q_{\text{LiDAR}})\ \vec{r}_{p,i,\mathcal{L}} \tag{2.36}$$

If the vectors are written out fully the equation looks like (2.37).

$$\begin{bmatrix} x_{\text{p}} \\ y_{\text{p}} \\ z_{\text{p}} \end{bmatrix}_{\mathcal{I}} = \begin{bmatrix} x_{\text{L}} \\ y_{\text{L}} \\ z_{\text{L}} \end{bmatrix}_{\mathcal{I}} + \mathbf{R}(q_{\text{L}}) \cdot \begin{bmatrix} x_{\text{p}} \\ y_{\text{p}} \\ z_{\text{p}} \end{bmatrix}_{\mathcal{L}} \tag{2.37}$$

With the following parameters:

- $\vec{r}_{p,\mathcal{I}}$ is the position vector of the measurement position in the inertial reference frame.
- $\vec{r}_{\text{LiDAR},\mathcal{I}}$ is the position vector of the LiDAR in the inertial reference frame.
- $(\mathbf{R}(q_{\text{LiDAR}})$ is a rotation matrix, a function of quaternions, defining the rotation from LiDAR to inertial reference frame.
- $q_{\text{LiDAR}} = q_O(\psi_{\text{yaw}}, \theta_{\text{pitch}}, \varphi_{\text{roll}})$ is the quaternion describing the orientation of the LiDAR.
- $\vec{r}_{p,\mathcal{L}}$ is the position vector of the measurement position in the LiDAR reference frame.
- x_{mount} is the distance between the mounting position of the LiDAR and the measurement of the orientation and displacement.

The LiDAR position ($\vec{r}_{\text{LiDAR},\mathcal{I}}$) is dependent on the translational movement of the FOWT. These are found by implementing the surge, sway and heave motion of the FOWT, as expressed below in (2.38)

$$\begin{bmatrix} x_{\text{L}} \\ y_{\text{L}} \\ z_{\text{L}} \end{bmatrix}_{\mathcal{I}} = \begin{bmatrix} x_{\text{surge}} \\ y_{\text{sway}} \\ z_{\text{heave}} \end{bmatrix}_{\mathcal{I}} \tag{2.38}$$

The rotation of the LiDAR is expressed in the yaw, pitch, and roll angles, and the rotation matrix can be deduced from the quaternion of the rotating motion of the LiDAR. This is described in detail in [32]. However, in this thesis, rotation matrices based on Euler angles are used to simplify the implementation of orientation changes. The Matlab function *eul2rotm()* is used to compute the corresponding orientation matrix, where the default axis rotation sequence of 'ZYX' is applied. However, in further research, quaternions should be implemented to make the rotation matrix unambiguous and more robust by not allowing Gimbal lock, for example.

Looking back at (2.15), all parameters are now defined to find V_{LOS}. The position of the measurement location $\vec{r}_{p,\mathcal{I}}$ is known, which can be used to retrieve the wind speed that is measured from the simulated wind field. The speed of the LiDAR is also known by simulation or measurements of the IMU. The direction vector is defined by the LiDAR beam geometry settings and can be transformed to inertial coordinates with (2.35). Lastly, $W(F, r)$ is fully dependent on the LiDAR properties.

2.5.3. Beam to LiDAR

For the weighting function described in (2.26) a transformation is required to move from the LiDAR frame to the beam coordinate frame. A rotation is required. For rotation, the z-axis of the LiDAR frame is defined by the unit vector $z_0 = [0, 0, 1]^T$ should be aligned with the direction vector $\vec{d}_n$. The rotation axis can be computed by taking the cross product of these two vectors as defined in (2.39).

$$\vec{s} = \vec{z}_0 \times \vec{d}_n = \begin{pmatrix} d_{n,y} \\ -d_{n,x} \\ 0 \end{pmatrix} \tag{2.39}$$

Consequently, the angle of rotation is found by applying the dot product between the two vectors, as is done in (2.40).

$$\cos(\phi) = \vec{z}_0 \cdot \vec{d}_n = d_{n,z} \tag{2.40}$$

Rotation along the rotation axis s with rotation angle ϕ can be performed using the Euler-Rodrigues formula given in (2.41) from [9]. The rotation axis used here should be a unit vector and is thus normalised as $\vec{s}_n = \frac{\vec{s}}{||\vec{s}||}$.

$$\boldsymbol{R} = \boldsymbol{I} + \sin\phi[\vec{s}_n\times] + (1-\cos\phi)[\vec{s}_n\times]^2. \tag{2.41}$$

In (2.41) $[\vec{s}_n\times]$ represents the skew-symmetric matrix of the unit axis of rotation $\vec{s}_n$, expressed as (2.42).

$$[\vec{s}_n\times] = \begin{bmatrix} 0 & -s_{n,z} & s_{n,y} \\ s_{n,z} & 0 & -s_{n,x} \\ -s_{n,y} & s_{n,x} & 0 \end{bmatrix} \tag{2.42}$$

Finally, the rotation can be applied to the position vector in the beam frame to rotate it to the LiDAR frame. The opposite can also be achieved by multiplying by the inverse of the rotation matrix.

$$\vec{r}_{p,\mathcal{L}} = \mathbf{R}\,\vec{r}_{p,\mathcal{B}} \tag{2.43}$$

2.6. Reconstruction

When the (corrected) direction, position and LOS velocity have been computed with the LiDAR model, a reconstruction of the measured wind field is required to complete the loop and gain some useful knowledge on the actual wind field surrounding the turbine. To find a mean wind speed of the field as a 10-minute average, often the least squares method is used, where the error between the V_{LOS} and the reconstructed wind speed along the same direction is minimised, as shown in (2.44), for the total number of measurements or simulations N.

$$\min_{\vec{V}} \sum_{i=1}^{N} \left(V_{LOS,i} - \vec{V}(H_i)\cdot\vec{d}_{n,i} \right)^2 \tag{2.44}$$

If the V_{LOS} measurement is assumed to be a point measurement at the centre of its range gate, then (2.13) can be used for reconstruction, using the direction along the laser beams. However, if instead a volume averaged measurement is used,

For the reconstruction a model that describes the wind field is required. For example, a power law for the wind shear can be used or a more general model using basis functions can be applied. In these models the wind speed in vertical direction is assumed zero. Below the reconstruction based on a power law is described.

Power law (non-linear LS)

The velocity $\vec{V}_i$ from (2.45) can be modelled with a power law, which is detailed as a possible input in section 2.3. As this function is non-linear, the regular linear least squares method cannot be used. However, it is possible to use non-linear least squares.

$$\sum_{i=1}^{N} \left(V_{LOS,i} - U_{ref} \left(\frac{H_i}{z_{ref}} \right)^{\alpha} \cdot d_{x,i} \right)^2 \tag{2.45}$$

This function is then minimised by setting its partial derivatives for the unknown variables U_{ref}, z_{ref} and α to zero. This can be numerically evaluated with a Gauss-Newton algorithm.

2.7. Uncertainty quantification

As partially the goal of this research is to find the uncertainty in the wind speed corrections, an explanation of what uncertainty propagation means is required. First, a basic explanation is given, followed by an example of Cartesian to polar coordinate transformations.

2.7.1. Analytical uncertainty propagation

The following explanation of uncertainty quantification is based on [7]. As an example, a function f is taken with variables X_1 and X_2. This function is Taylor expanded to the first order, as in (2.46). This also poses the first problem of the analytical uncertainty propagation. Usually, the higher orders are ignored, due to which only linear error propagation is possible. This can pose problems for non-linear models. This is discussed in more detail in subsection 2.7.4.

$$Y = f(X_1, X_2) \approx f(\mu_{X_1}, \mu_{X_2}) + \frac{\partial f}{\partial X_1}(X_1 - \mu_{X_1}) + \frac{\partial f}{\partial X_2}(X_2 - \mu_{X_2}). \tag{2.46}$$

The estimate of the random variable X_i is x_i, while the estimate of the measured Y is y. When taking the variance of this function, the resulting variance for y is found in (2.47), where the last term represents the covariance between the variables x_1 and x_2. The partial derivatives can be seen as the sensitivity coefficient of the uncertainty propagation because these determine how much a certain variance or covariance of the inputs contributes to the final variance of the output.

$$\sigma_c^2(y) = \left(\frac{\partial f}{\partial x_1}\right)^2 \sigma^2(x_1) + \left(\frac{\partial f}{\partial x_2}\right)^2 \sigma^2(x_2) + 2\frac{\partial f}{\partial x_1}\frac{\partial f}{\partial x_2}\sigma(x_1, x_2). \tag{2.47}$$

This can be generalised for a function with more variables according to (2.48), where the last term $\sigma(x_i, x_j)$ represents the covariance of x_i and x_j.

$$\sigma_c^2(y) = \sum_{i=1}^{N}\left(\frac{\partial f}{\partial x_i}\right)^2 \sigma^2(x_i) + 2\sum_{i=1}^{N-1}\sum_{j=i+1}^{N}\frac{\partial f}{\partial x_i}\frac{\partial f}{\partial x_j}\sigma(x_i, x_j). \tag{2.48}$$

Recall that the variance is expressed as (2.49).

$$\sigma^2(x) = \frac{1}{N}\sum_{i=1}^{N} x_i - \mu \tag{2.49}$$

When two output quantities can be found through a model that have the same input values, then a covariance matrix can be used as described in (2.50), with $\mathbf{U}_x$ the covariance matrix of the inputs and $\mathbf{C}_y$ the covariance matrix of the outputs. The matrix $\mathbf{J}_x$ is the Jacobian matrix and contains the partial derivatives, or sensitivity coefficients. Therefore, the Jacobian matrix can also be called the sensitivity matrix. These matrices can be extended to a larger number of inputs and outputs.

$$C_y = \mathbf{J}_x \mathbf{U}_x \mathbf{J}_x^T = \begin{bmatrix} \sigma^2(y_1) & \sigma(y_1, y_2) \\ \sigma(y_1, y_2) & \sigma^2(y_2) \end{bmatrix} \text{ with } \mathbf{J}_x = \begin{bmatrix} \frac{\partial f_1}{\partial x_1} & \frac{\partial f_1}{\partial x_2} \\ \frac{\partial f_2}{\partial x_1} & \frac{\partial f_2}{\partial x_2} \end{bmatrix} \tag{2.50}$$

These matrices can be extended to a larger number of inputs and outputs.

2.7.2. Monte Carlo

Another way of performing uncertainty propagation is described by the Monte Carlo method. In this method a large amount of random samples are taken for the inputs. All of these are then put through the model, resulting in a large number of output values as well. The distribution of these output values can then be fitted to find its mean and uncertainties. This is also illustrated with Figure 2.12.

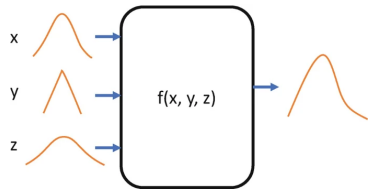

Figure 2.12: The principle of the Monte Carlo method

The random samples of the inputs will be generated using Pseudo-Random Number Generators (PRNG). This PRNG should comply with a few requirements in order to perform a reliable Monte Carlo uncertainty analysis, as stated in [8]. Firstly, the sequence length of the PRNG after which the random numbers will be repeated should be larger than the number of samples, generally the square of the sample number [24]. Second, the random numbers should be independent and uncorrelated. Third, the random values should be sampled uniformly within the range, that is, they should not be biased towards a certain value. Finally, the random numbers should be reproducible for debugging and testing of the model.

The advantage of this method is that no assumptions are made about the model or the inputs. In order to check the convergence of the Monte Carlo method, a convergence plot can be used to see if the output value stays close to one value. This process can also be automated by setting a tolerance under which the changes in the output value should remain.

Although the Monte Carlo method does not directly use any sensitivity coefficients, they can still be estimated. To do this, all input variables are kept constant, while the variable of interest x_1 is sampled to create a large input set. Then the output uncertainty, due to the randomly sampled variable of interest, can be computed just like a regular Monte Carlo simulation. Now, to obtain the sensitivity coefficient, the variance in output due to varying x_1, should be divided by the variance in output where all inputs are sampled.

2.7.3. Example Cartesian to polar coordinates

To test the application of uncertainty propagation, this method has been applied to random points defined in Cartesian coordinates that are transformed to polar coordinates, with (2.51) and (2.52). For this distribution a normal distribution is used with $\mu_x = 0$ and $\mu_y = 1$, the covariance matrix of the inputs x and y is chosen as (2.53).

$$r = \sqrt{x^2 + y^2} \tag{2.51}$$

$$\theta = \arctan\left(\frac{y}{x}\right) \tag{2.52}$$

$$\mathbf{C}_x = \begin{bmatrix} 0.01 & 0.001 \\ 0.001 & 0.01 \end{bmatrix} \tag{2.53}$$

The confidence ellipse of the normal random distribution of 100,000 points is depicted in Figure 2.13.

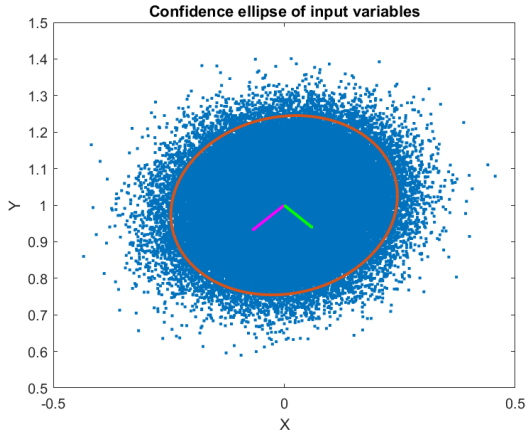

Figure 2.13: Confidence ellipse of input variables x and y

The confidence ellipse of the two outputs θ and r is shown in Figure 2.14, which can be compared to the Monte Carlo method in Figure 2.15.

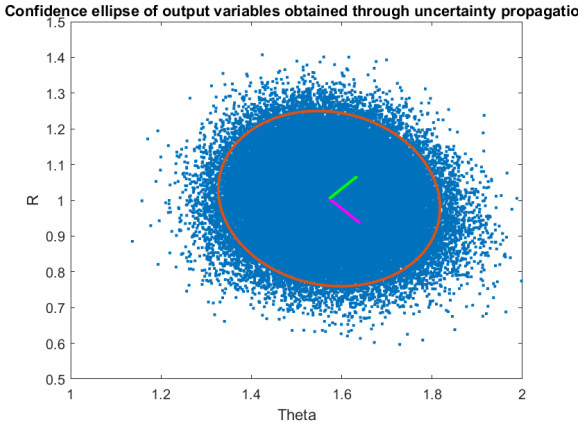

Figure 2.14: Confidence ellipse of output variables θ and r, using analytical uncertainty propagation

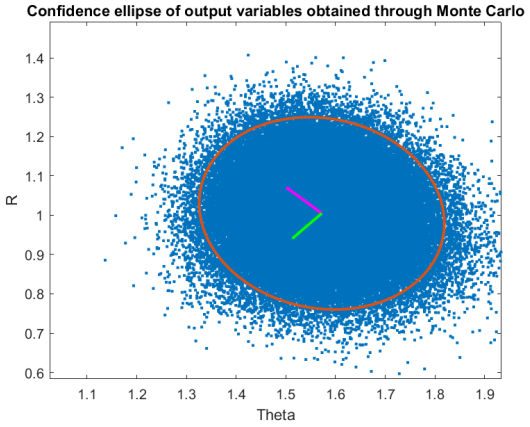

Figure 2.15: Confidence ellipse of output variables θ and r, using Monte Carlo

2.7.4. Limitations

A major limitation of analytical uncertainty propagation exists due to the first order Taylor approximation. Non-linearities cannot be captured because of this. It can be difficult to know beforehand what the influence of non-linearities in the model on the variance of the output is. If the variance of the inputs is small, that is, the function is evaluated over a small range, it can be approximated as linear. However, the larger the range, the farther from reality this becomes. This is clearly illustrated in Figure 2.16. The function $f(x) = e^x$ is used in this example and is plotted with an x-measurement with a small variance (left) and a high variance (right).

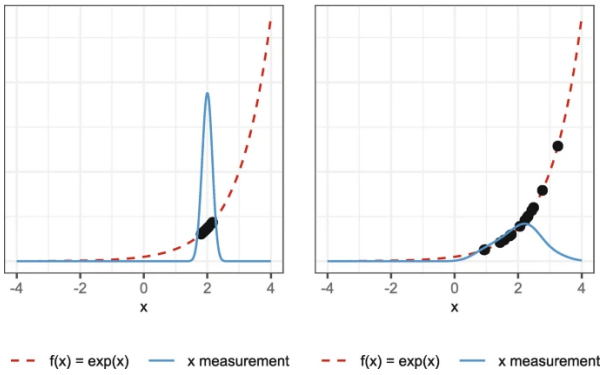

Figure 2.16: Illustration of how uncertainty in inputs influences the validity of the linear approximation from [7]

The example that is used also makes use of non-linear equations. The choice of the variance of the inputs and the choice of the mean of the inputs influence the degree to which nonlinearities play a role. In this case, the variance should be small and the mean of the coordinates should be sufficiently far from the origin. This in order to guarantee that the mean of r and θ is larger than their variance. In other words $\frac{\sigma}{\mu}$ should be small. If the mean of the inputs x and y is taken at the origin, so at $(0, 0)$, then nonlinearities will definitely play a role, since both r and θ will be heavily influenced by the spread of the inputs. This is illustrated in Figure 2.18 and can be compared to the linear case in Figure 2.17.

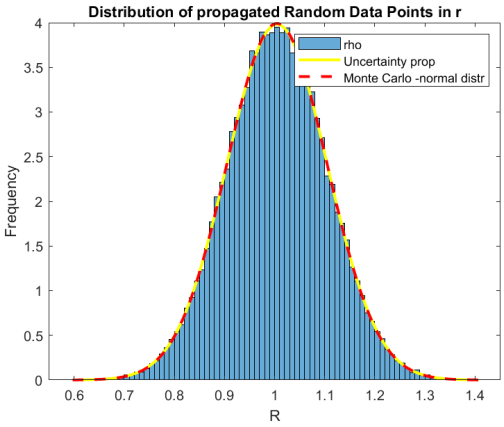

Figure 2.17: PDF of r with $m_x = 0$ and $\mu_y = 1$, non-linearity can be ignored

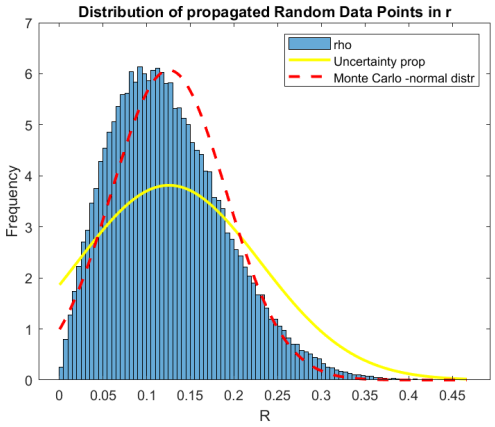

Figure 2.18: PDF of r with $m_x = 0$ and $\mu_y = 0$, non-linearity cannot be ignored

Besides linearities, another problem that the analytical method poses is that partial derivatives of the model are required, while for some models this is not possible. This could be the case if the model is, for example, discontinuous.

Another huge assumption that is applied in the method described above is that all inputs have a normal distribution, this is required to perform the uncertainty propagation. However, it is very likely that for at least one of the input variables that will be analysed the distribution is not normal. As a result of this assumption, the output variable will also always have a normal distribution, while in reality this might not be an accurate representation.

To overcome the assumption of a linear model, a Monte Carlo analysis can be applied. If possible, this should always be used to check the validity of the analytical approach. However, at some point when a lot of inputs are used that all require a large amount (1,000,000 or even more) of samples, this method can become too computationally expensive. Another advantage of using Monte Carlo over analytical uncertainty propagation is that the output can have another distribution then a normal distribution, as the input samples do not have to be taken as a normal distribution.

2.8. Set up of Tetraspar demonstrator

The case study on which this thesis is based is the Tetraspar demonstrator located off the coast of Norway. It is equipped with a $3.6MW$ SGRE turbine at a water depth of around 200 m. The Tetraspar demonstrator is shown in Figure 2.19 [4]. What makes this floating design stand out is that it consists only of parts that can be manufactured in an industry with an already existing supply chain.

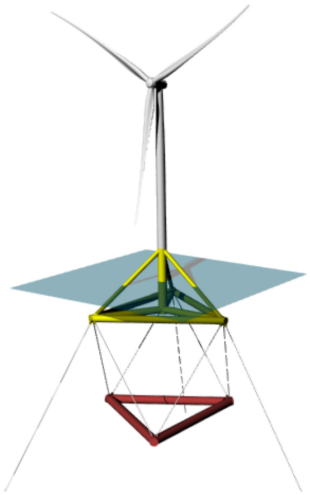

Figure 2.19: Tetraspar concept from [4]

Figure 2.20: WindCube Nacelle Lon-Range LiDAR

2.8.1. LiDAR

The floating wind turbine has a four-beam pulsed LiDAR mounted on top of the nacelle. More specifically, this is the WindCube Nacelle Long-Range LiDAR Figure 2.20 developed by Leosphere, a Vaisala company. The LiDAR has a range up to $700m$, with a maximum of 20 range gates. The specifications of the LiDAR will be further detailed in subsection 3.1.5.

2.8.2. IMU

The Tetraspar demonstrator is also equipped with an Inertial Measurement Unit (IMU), which measures both translational and rotational acceleration and velocity using accelerometers and gyroscopes, as well as orientation and position using GNSS data. The specific IMU used on top of the Tetraspar is the Taxtical Grade MEMS Inertial Sensor of the Ekinox series produced by SBG systems. For application of the correction algorithm to actual LiDAR measurements on the Tetraspar the measurements from this system would be used. However, in this thesis only simulated motion data is applied.

3
Methodology

In this chapter, the methods used to obtain the required results for this research will be discussed. Both the algorithm and equations themselves, as well as how to obtain the uncertainties for each step will be presented.

First, the inputs of the model will be discussed section 3.1, that is the motions, wind field and LiDAR properties. Next, the LiDAR model that simulates the LiDAR measurement is explained in section 3.2, where in section 3.3 a focus is placed on the output generated by this model. These outputs are measurement position, direction and the simulated line of sight velocity, including their (co)variance matrices. Consequently, it is explained in section 3.4 how these outputs are used for the reconstruction of the input wind field. Lastly, in section 3.5 an explanation is given as to how the final uncertainty of the reconstructed wind field is obtained.

3.1. Inputs

The generation of the inputs for the LiDAR model is discussed in this section. The floater motions, the wind field and the LiDAR properties will be covered.

3.1.1. Floater motion

The floater motions are modelled with increasing complexity, starting with simple harmonic motions that are easy to implement and analyse. This is followed by simulated floater motions in 2DOF and then increased to simulated motions in 6DOF. Due to time constraints, the experimental IMU data have not been analysed, but they can be said to be close to the simulated 6DOF results.

Harmonic motions

The first motions that are implemented to test the working principle of the program are harmonic motions. The motions of the floater are described by simple harmonics as expressed by (3.1) and (3.2). These describe the motions in all 6DOF, so in translation and rotation. Each motion has a specific amplitude A and a period T. The harmonic floater motions are around the centre of gravity of the floater and need to be transferred to hub height. If the tower is assumed to be rigid, the velocity described in (3.3) from [47] gives the velocity at hub height, where the LiDAR is located. Now, the total translational velocity is known in the directions x, y, and z at hub height. The hub height is equal to $H_{hub} = 90m$, which is the hub height of the Tetraspar demonstrator.

The amplitudes and periods used in this research are based on the Response Amplitude Operators (RAO's) for a floating wind turbine with a square-shaped barge platform given in [1], these are summarised in Table 3.1. The translational velocity at hub height in the z-direction is not a sinusoidal wave, because sinusoidal waves with different periods are added here. The heave motion, namely, has a larger period compared to the other motions. These are used in order to consider somewhat realistic motions, but it should be noted that this differs greatly per floater design, aside from the fact that the motions are immensely idealised by assuming harmonic motions here. Later, more complex and

realistic motions will be considered.

$$x = A\sin\left(\frac{2\pi}{T}t\right) \tag{3.1}$$

$$V = A\frac{2\pi}{T}\cos\left(\frac{2\pi}{T}t\right) \tag{3.2}$$

$$\begin{aligned}\vec{V}_{hub} = [\ V_{x,surge} \quad &+H_{hub}\dot{\theta}_{\text{pitch}}\cos\left(\theta_{\text{pitch}}\right) - H_{hub}\dot{\psi}_{\text{yaw}}\cos\left(\psi_{\text{yaw}}\right)\ ] \quad \vec{i} \\ +[\ V_{y,sway} \quad &+H_{hub}\dot{\psi}_{\text{yaw}}\sin\left(\psi_{\text{yaw}}\right) - H_{hub}\dot{\varphi}_{roll}\cos\left(\varphi_{roll}\right)\ ] \quad \vec{j} \\ +[\ V_{z,heave} \quad &+H_{hub}\dot{\varphi}_{roll}\sin\left(\varphi_{roll}\right) - H_{hub}\dot{\theta}_{pitch}\sin\left(\theta_{pitch}\right)\ ] \quad \vec{k}\end{aligned} \tag{3.3}$$

Direction	Amplitude	Period [s]
Surge	2.0 [m]	13
Sway	0.2 [m]	13
Heave	1.0 [m]	20
Roll	0.02 [°]	13
Pitch	2.50 [°]	13
Yaw	0.20 [°]	13

Table 3.1: Input values harmonic motions

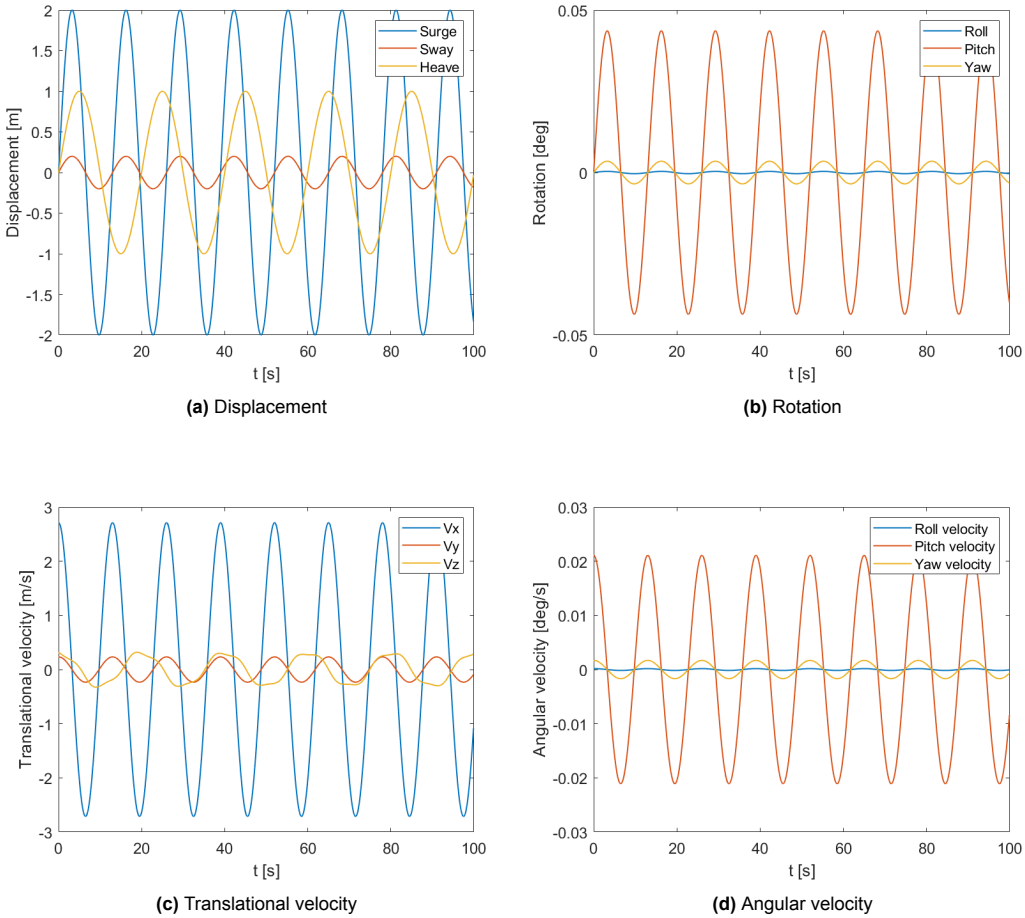

(a) Displacement

(b) Rotation

(c) Translational velocity

(d) Angular velocity

Figure 3.1: Harmonic motions

2DOF BHawC floating example

To have more realistic movements a simulation in BHawC has been used. BHawC stands for Bonus Horizontal Axis Wind turbine Code and is an aero-servo-elastic simulation tool, developed by Siemens Gamesa to model loads on wind turbines. The 2DOF floater model is a separate model, and the motions simulated by this tool are coupled with the tower bottom. Even though the floater motion model has 2DOF, the BHawC model still models 6DOF due to tower vibrations. The resulting motions are taken at the top of the nacelle, close to the location where the LiDAR would be.

Here, the floater is modelled in 2 degrees of freedom and is applied to a representative floating offshore wind turbine. The 2DOF that are used are motions in x direction: surge and x-velocity, as well as rotations around the y-axis, meaning pitch motions. The results are shown in Figure 3.2 below. A power law wind profile is used, with a wind speed of $10m/s$ at the hub height and $\alpha = 1/7$ at the hub height of $z_{ref} = 86.2m$, corresponding to the tower top height from which the BHawC simulation data are taken. This is summarised in Table 3.2. It can be seen that the structure experiences decaying oscillations either around zero for surge and x-velocity or around a non-zero mean value for pitch. This is an inherent property of floating wind turbines that will be pitching backward due to the aerodynamic thrust force that the turbine experiences at the rotor.

Both pitch and velocity show smaller oscillations around the larger oscillating motions. These oscillations correspond to higher structural modes. For this 2DOF model only a power law wind field is given as input to generate floating motions, no wave loads are included here. That is why the oscillation is quite low in Figure 3.2. This is also the reason for the motion to look like a decaying harmonic motion. The turbine responds to the wind field and finds a new equilibrium position.

U_{ref} [m/s]	10
Hub height (z_{ref}) [m]	86.2
α [-]	0.1429

Table 3.2: Input data on wind field

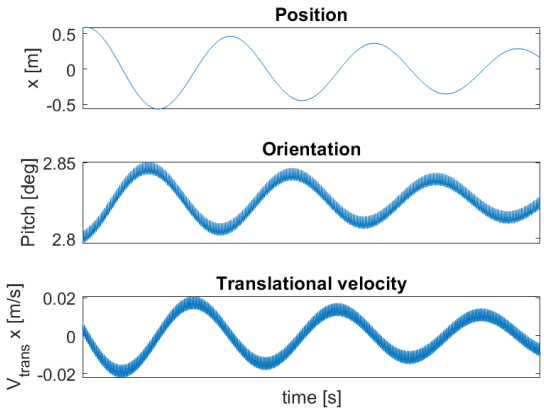

Figure 3.2: 2 DOF motions BHawC, taken at the nacelle

6DOF BHawC-Orcaflex + turbulence

For the application of this project in reality, information is required for all six degrees of freedom instead of only two. This is achieved by another simulation. This time using the coupled code BHawC-Orcaflex, which models both the floater dynamics to environmental inputs, as well as the structural response of the whole turbine, including the tower. In this code, the Tetraspar model is implemented, which allows for better comparison with the experimental IMU measurements. Additionally, turbulence is added to this simulation using the Mann model, which results in less predictable motions. The input conditions for the wind field are summarised in Table 3.3. In addition to this more complicated wind field, waves and current are added to the turbine's environment. The most important input parameters for the ocean

environment are documented in Table 3.4. The resulting environmental wind and wave conditions are given in Figure 3.4. Much more inputs are given for the simulation, such as the specifications for the Mann turbulence box and the specifications of the floater kinematics, to model the floating response to wind and waves, but these are taken as given for the Tetraspar turbine. The results are documented in Figure 3.3.

U_{ref} [m/s]	18
Hub height (z_{ref}) [m]	86.9
α [-]	0.05
Turbulence intensity (TI) [-]	0.062

Table 3.3: Input data on wind field

Wave spectrum	Torsethaugen
Wave height (H_s) [m]	2.88
Wave period (T_0) [s]	8.33
Ocean current speed [m/s]	0.352

Table 3.4: Input data on waves

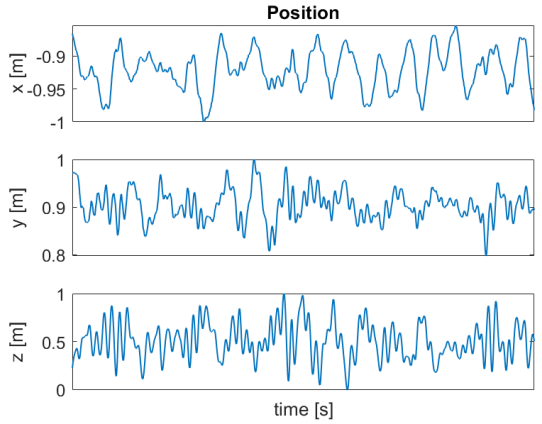

(a) Displacement

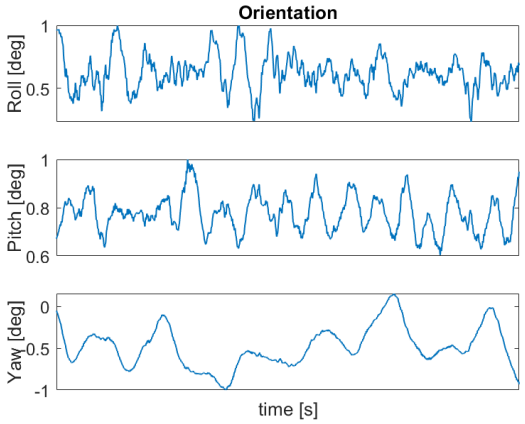

(b) Rotation

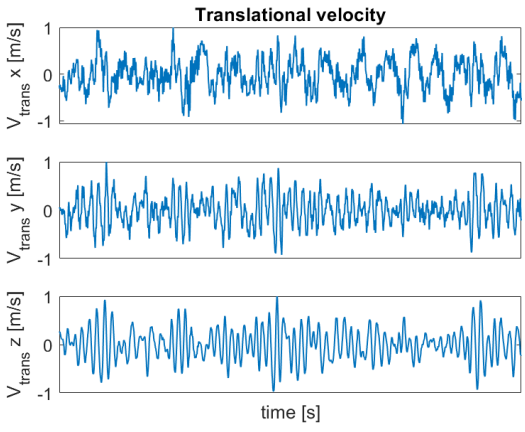

(c) Translational velocity

Figure 3.3: BHawC simulated motions, normalised to the maximum value, in 6DOF with turbulent wind field

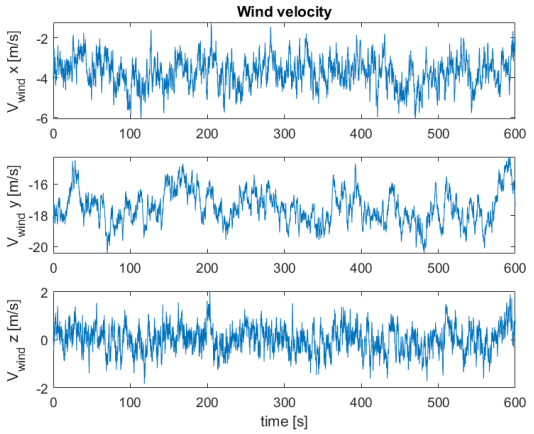

(a) Wind velocity in x, y and z direction

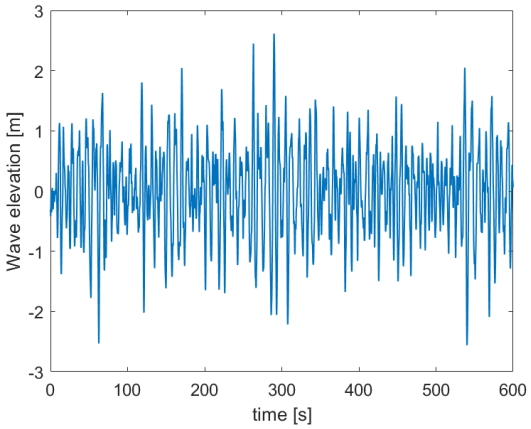

(b) Wave elevation

Figure 3.4: Environmental conditions for the 6DOF motion simulation

3.1.2. Regression and uncertainty model

The data obtained through the simulations have noise, as will the real experimental data obtained from the IMU measurement device. A regression method can be used to smooth the data as it were and in this way get rid of the high frequency fluctuations. An advantage of using this method is that the data will now be known continuously and any point in time can be chosen to find the corresponding motion. This is necessary to time the motion with the corresponding LiDAR measurement.

Using this regression technique helps to quantify uncertainties in the motion data. This can be expressed by the variance of the regression model, described in (3.4).

$$\sigma_y^2 = \sigma_{\hat{y}}^2 + \sigma_\epsilon^2 \tag{3.4}$$

The derivation for this will be given in the following and is based on [25].

A linear regression model of the form shown in (3.5) is used. Where, y is a vector containing the observed variables of the motion, such as position, velocity or orientation. Then X is the design matrix, containing functions of the independent variable of time t. The vector $\vec{\beta}$ contains the regression coefficients and lastly, $\vec{\epsilon}$ is the noise term.

$$\vec{y} = \mathbf{X}\vec{\beta} + \vec{\epsilon} \tag{3.5}$$

The design matrix $\mathbf{X}$ contains polynomial basis functions that are a function of t. These regressors between two data points are represented by Quintic-Hermite basis functions. These are used to guarantee smoothness of the fit and continuity of its first and second derivatives. This was initially set up by Axel Matavar in [32], where he provided a fit for position, velocity and acceleration, all at the same time. Quintic-Hermite basis functions as opposed to Cubic-Hermite basis functions were required, to ensure continuity of the second derivative for acceleration.

$$y_i = \sum_{j=1}^{6} \beta_{j,i} H_{j,i}(t_i) + \epsilon_i \tag{3.6}$$

The noise term ϵ will represent what part of the original data is not captured, looking at the residuals of the fit, and thus will provide information on the value of the noise of the original signal. The noise term is assumed to be normally distributed, with mean 0 and variance σ_ϵ^2, as expressed in (3.7).

This error model of normal distributed residuals with a zero mean is a good choice for the 6DOF data, as shown in Figure 3.5, but not for the 2DOF data. However, it will still be used for the evaluation of the data to be consistent with the evaluation of the 6DOF data.

$$\epsilon \sim \mathcal{N}(0, \sigma_\epsilon^2) \tag{3.7}$$

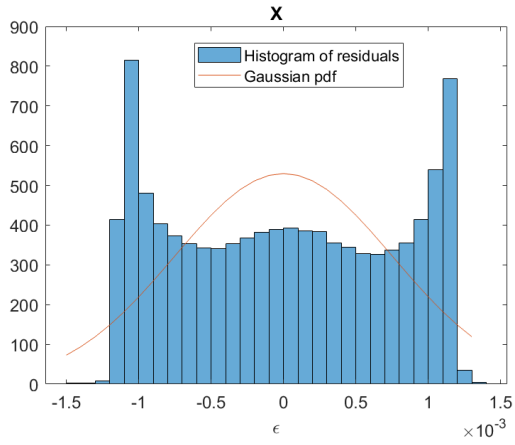

(a) Surge 2DOF

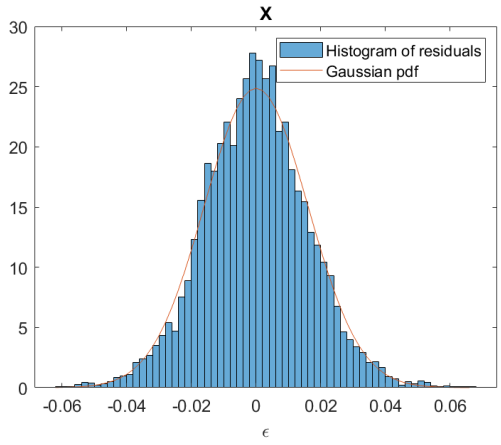

(b) Surge 6DOF

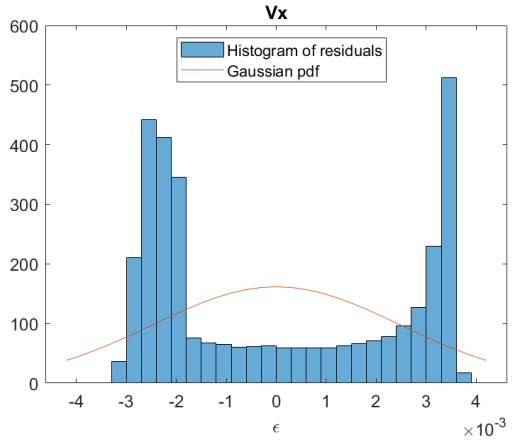

(c) X-Velocity 2DOF

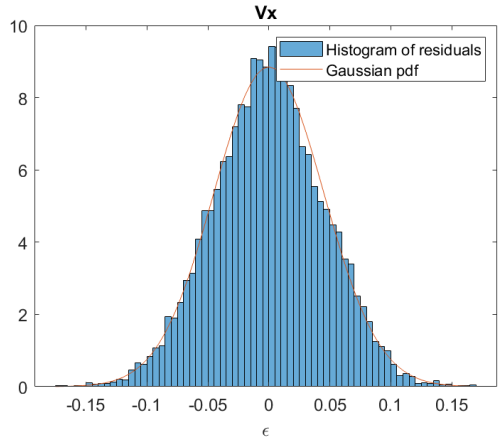

(d) X-Velocity 6DOF

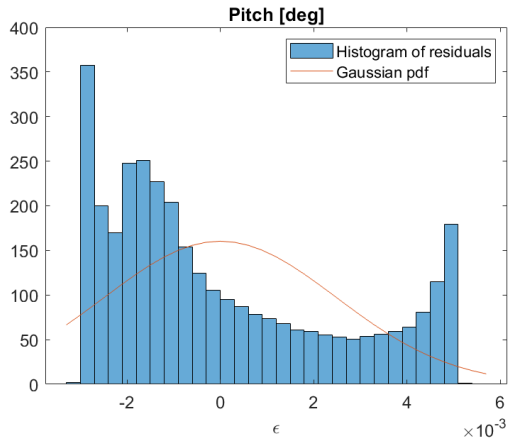

(e) Pitch 2DOF

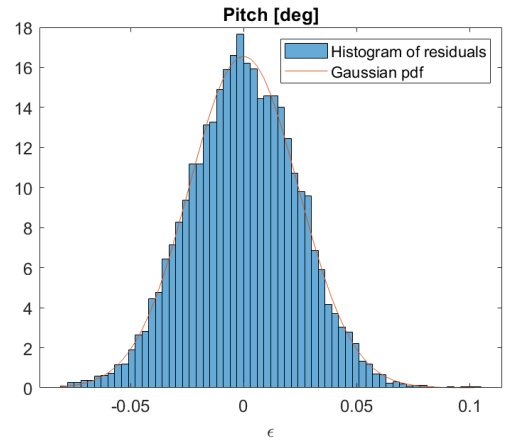

(f) Pitch 6DOF

Figure 3.5: Histogram of residuals of the regression fits for 2DOF and 6DOF simulated data, with a Gaussian pdf fitted to it

The residuals or noise terms are modelled according to (3.8). Their uncertainty is computed according to (3.9). The resultant value of this equation is also called the Mean Square Error (MSE). For (3.9), the parameter N is the number of measurement or simulation points, which is found by $N = \frac{\text{Sample duration [s]}}{\text{Sampling period [s]}}$. Therefore, $N = 600/0.02 = 30000$ for the 2DOF simulation and $N = 600/0.04 = 15000$ for the 6DOF simulation. The value p represents the number of unknown parameters for the regression, which is $p = 6$ for the 6 regression coefficients of the Quintic-Hermite regression to arrive at an unbiased variance.

$$\vec{\epsilon} = \vec{y} - \mathbf{X}\vec{\beta} \tag{3.8}$$

$$\sigma_\epsilon^2 = \frac{(\vec{y} - \mathbf{X}\vec{\beta})^T(\vec{y} - \mathbf{X}\vec{\beta})}{N - p} \tag{3.9}$$

The predicted values $\hat{y}$, which are fitted with the linear regression model, are found with (3.10).

$$\vec{\hat{y}} = \mathbf{X}^*\vec{\hat{\beta}} \tag{3.10}$$

Now, the variance of this predicted value $\hat{y}$ due to model uncertainty, can be taken as (3.11). Where in this equation, $\mathbf{C}_{\hat{\beta}}$ is the covariance matrix of the regression coefficients and $\mathbf{X}^*$ is the design matrix for the time interval that is desired for the prediction. The design matrices $\mathbf{X}$ and $\mathbf{X}^*$ thus have the same coefficients for the Quintic-Hermite basis functions, but are evaluated at different time intervals. This equation is an uncertainty propagation of the uncertainty in $\vec{\hat{\beta}}$.

$$\mathbf{C}_{\hat{y}} = \mathbf{X}^*\mathbf{U}_{\hat{\beta}}\mathbf{X}^{*T} \tag{3.11}$$

The variance of $\vec{\hat{\beta}}$ can be deduced from (3.12). For this equation, it is assumed that all noise terms have the same variance σ_ϵ^2 and are uncorrelated. For the actual measurements this is not true, which will be discussed in subsection 3.1.3. Furthermore, σ_ϵ^2 is given in (3.9).

$$\mathbf{C}_{\hat{\beta}} = \sigma_\epsilon^2(\mathbf{X}^T\mathbf{X})^{-1} \tag{3.12}$$

Now, if (3.12) is filled into (3.11), (3.13) is produced to find the variance in the model prediction.

$$\mathbf{C}_{\hat{y}} = \sigma_\epsilon^2\left(\mathbf{X}^*\left(\mathbf{X}^T\mathbf{X}\right)^{-1}\mathbf{X}^{*T}\right) \tag{3.13}$$

If then the variance in noise or residuals is added to that, as done in (3.4), but now in matrix form, finally (3.14) is obtained. This thus represents the total variance in the predicted values, considering the model error, as well as the error due to noise.

$$\mathbf{C}_y = \sigma_\epsilon^2\left(\mathbf{X}^*\left(\mathbf{X}^T\mathbf{X}\right)^{-1}\mathbf{X}^{*T} + \mathbf{I}\right) \tag{3.14}$$

Regression position and velocity

Position and velocity data are related to each other, as they are both based on accelerometer and satellite positioning data. Position is the derivative of velocity. Therefore, the regression for these data points is performed in one go per direction. The design matrix $\mathbf{X}$ thus consists of both the Quintic-Hermite equations and their derivatives. The vector with observed variables $\vec{y}$ includes both position and velocity data.

The difference in the uncertainty calculations presents itself in the calculation of the variance of the noise term, in (3.9). Now only half of the design matrix $\mathbf{X}$ and half of the observation vector $\vec{y}$, with the position and Quintic-Hermite relations, or the velocity and derivative of those relations are used, respectively. N changes to the number of observations of either of the variables. Moreover, the calculation of (3.11) changes too. Namely, the matrix $\mathbf{X}^*$ now contains the Quintic-Hermite relations for position and for velocity the derivative is used, both applied to the sampling time of the output of the regression.

Regression orientation
For orientation the method described in the section above is used, no coupling between it's velocity is assumed, because this data is not always available. While for this research Quintic-Hermite regression of the Euler angles is applied, a better approach would be to use splines for the quaternion version of the orientation. Quaternions would be better to use, because there cannot be any ambiguity when rotating in different reference frames and gimbal lock does not occur. More information on how to apply quaternions within this research framework is extensively discussed in [32].

Choosing a time step for the regression
A time step for which the regression nodes are picked is set at $4s$. The LiDAR measurements are averaged over 4 seconds. Therefore, knowing the movement data more precisely for smaller time steps does not make sense.

Moreover, with a very crude calculation, it can be assumed that the tripod installation of the LiDAR has vibration periods in the order of one tenth of a second or smaller. If the tripod with the LiDAR mounted on top is simplified as a cantilever beam structure and the beam is modelled as one straight leg of the tripod, then the stiffness of the tripod can be calculated as (3.16). The material of the tripod is assumed to be aluminium with a Young's modulus of $E = 70GPa$, the length of the tripod with its legs spread out is approximately $L = 1m$, the LiDAR head weighs approximately $m = 25kg$ and lastly the diameter of one of the legs of the tripod is approximately $D = 0.05m$. All this would result in an area moment of inertia of $I = 3.0710^{-7}m^4$, from (3.17), a stiffness of $k = 64470N/m$ from (3.16) and a period for the vibration of $T = 0.12s$ from (3.15).

$$T = \frac{2\pi}{\omega} = 2\pi\sqrt{\frac{m}{k}} \tag{3.15}$$

$$k = \frac{3EI}{L^3} \tag{3.16}$$

$$I = \frac{D^4\pi}{64} \tag{3.17}$$

These calculations should be taken with a very large grain of salt, because they are based on far reaching assumptions. The vibrations will, of course, be much more complex than that of a cantilever beam. Next to that, the material of the tripod is unknown. However, the moment of inertia will be a lot larger as the tripod's positioning of the 3 legs increases the structure's resistance against excitations, which would increase the stiffness and thus decrease the potential period further. The mass and length are taken from the LiDAR manufacturer's manual [6] and rounded to the nearest integer.

From these calculations a guess is made that the LiDAR vibrations are in the order of 10 Hz or 0.1 s. For IMU data, this would pose limitations in the time step of regression that can be taken, which should not be smaller than $1s$. Further research is necessary to properly quantify the vibrations of the LiDAR mounting bracket. This could be done by comparing the frequency of the orientation changes in pitch and roll recorded by the LiDAR with those measured by the IMU.

Taking larger time intervals in the fitting process, that is, using fewer nodes for regression, tends to increase the residual error, as the resulting graph cannot closely fit all the data points. However, since this error is two to three orders of magnitude smaller than the residual error, this effect is negligible.

The regression can be seen as some kind of low-pass filter, as for given regression time intervals it filters out the higher frequency data. Having more knowledge about the motion data than the LiDAR data does not make sense. The frequencies that are higher than the regression sampling frequency are not captured accurately and thus introduce error in the information that is known about the motion data. These higher frequencies are now considered signal noise. The motion error is quantified in terms of a noise error plus a model error.

3.1.3. Uncertainty in experimental motion data IMU

In this research, it should be noted that an assumption is made on the motion measurement, which will come into effect here. The IMU and the LiDAR are namely not mounted at the same location. This results in the motion measurements having to be transferred to the position of the LiDAR. To make this transformation possible, it is assumed that the connection of the LiDAR to the nacelle is rigid. The LiDAR is installed on a tripod, which is thus assumed to be rigid, while it will not be completely in reality. The consequence of this assumption is that high frequency motions cannot be transformed to the LiDAR as these are unlikely to be exactly the same at the location of the IMU and the LiDAR. It is not clear what a good cutoff frequency would be and which frequencies can be ignored, since the order of magnitude of the frequencies of the LiDAR bracket are unknown, the selection of this time step is further ignored in the section below in a section of 3.1.2.

For the IMU data, it is possible to get a standard deviation for each measurement in time. This can improve the uncertainty quantification in the motions. These standard deviations can be included in terms of weights W, where $\mathbf{W}$ would be a diagonal weight matrix with each entry $w_i = \frac{1}{\sigma_i^2}$. This can then be included in (3.9) to obtain (3.18), which is based on [37]. To obtain unbiased and normalised variance, a division is necessary with the sum of the weights and the number of DOF $p = 6$ of the Quintic-Hermite regression subtracted. (3.18) simplifies to (3.9) when all weights w_i are equal to 1.

$$\sigma_{\epsilon,w}^2 = \frac{(\vec{y} - \mathbf{X}\vec{\beta})^T \mathbf{W} (\vec{y} - \mathbf{X}\vec{\beta})}{\sum_{i=1}^{m} w_i - p} \tag{3.18}$$

Similarly, (3.14) can be extended to (3.19).

$$\mathbf{C}_{y,w} = \sigma_{\epsilon,w}^2 \left(\mathbf{X}^* \left(\mathbf{X}^T \mathbf{W} \mathbf{X} \right)^{-1} \mathbf{X}^{*T} + \mathbf{I} \right) \tag{3.19}$$

3.1.4. Wind field

Power law

As a first test of the LiDAR model and correction, a power law as described by (3.20) and used in the IEC standard [3] will be given as input for the wind field. This wind field was already described in section 2.3. A power law is used to ease reconstruction and comparison after completing the modelling loop. As a standard, to avoid ambiguity, the reference height is always taken as the hub height. In this way, only the reference speed and the exponent α have to be reconstructed.

$$U(z) = U_{ref} \left(\frac{z}{z_{hub}} \right)^{\alpha} \tag{3.20}$$

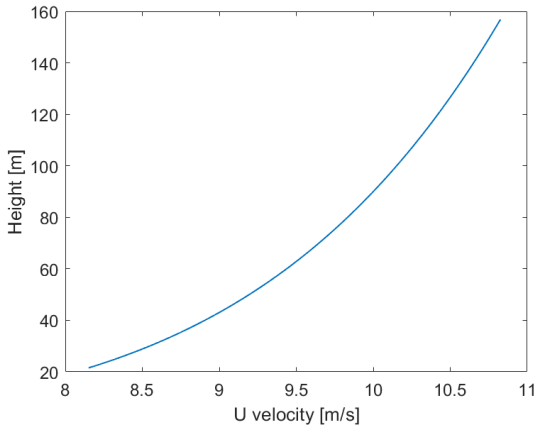

Figure 3.6: Power law wind profile with $U_{ref} = 10m/s$ and $\alpha = 1/7$

3.1.5. LiDAR properties

Pulse width

The pulse duration of the WindCube Nacelle v2.2 Long-Range configuration is found with (2.28) and (2.29), resulting in (3.21). In this equation c is the speed of light.

$$r_p = \frac{c\tau_p}{4\sqrt{\ln(2)}} \tag{3.21}$$

The question thus is what the value of the pulse duration τ_p is. This value is not given by the manufacturer. The difference between pulse duration and observation time or in terms of distance: pulse width or range gate length, is depicted in Figure 3.7. The pulse duration varies quite a lot depending on the LiDAR manufacturer. For example $343ns$ for [15], $115ns$ for [16] and $150ns$ for a scanning WindCube LiDAR from [28]. For the WindCube used in this research $\tau_p = 100\ ns$ was found to be a realistic value.

Knowing the pulse duration is important for the RWF and determines how many particles within the measuring volume are included for a specific range gate. The longer this time is, the more particles are illuminated and more information is received, leading to a lower signal-to-noise ratio. However, for shorter pulse durations the measuring position is more accurately known, which is key for reconstruction and results in less variance in wind speeds within the measurement volume.

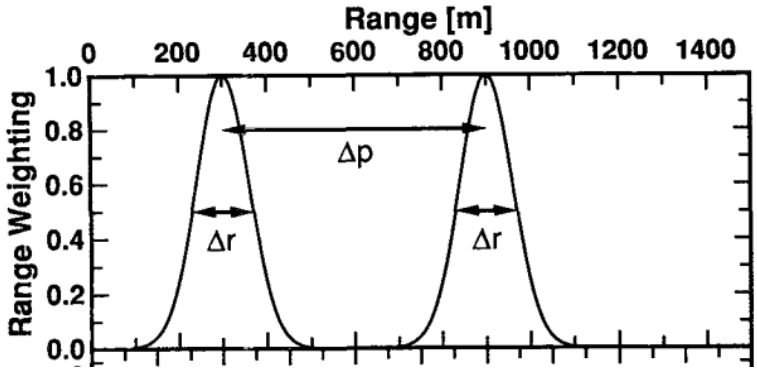

Figure 3.7: Comparison between pulse width Δr and range gate length Δp from [17]

Range gate length

The difference between the pulse width and the range gate length is visualised in Figure 3.7. The range gate length of the WindCube Nacelle v2.2 Long-Range configuration can be found in the manufacturer's manual as the probed length and is specified as $\Delta p = 30m$. To obtain the observed time of the range gate length, one can apply (3.22). Thus, resulting in an observation time $\Delta t_{\text{obs}} = 200ns$. In this equation c is the speed of light.

$$\Delta t_{\text{obs}} = \frac{2\Delta p}{c} \tag{3.22}$$

Range gate centre

The laser beams of the LiDAR can be divided into 20 range gates from 50 to 700 m. These are described along the horizontal x-direction. As the beams are at an elevation angle of $\gamma = 5°$, as shown in Figure 3.8, the range gate centre along the beam is found with (3.23).

$$F_{beam} = \frac{F}{cos(5°)} \tag{3.23}$$

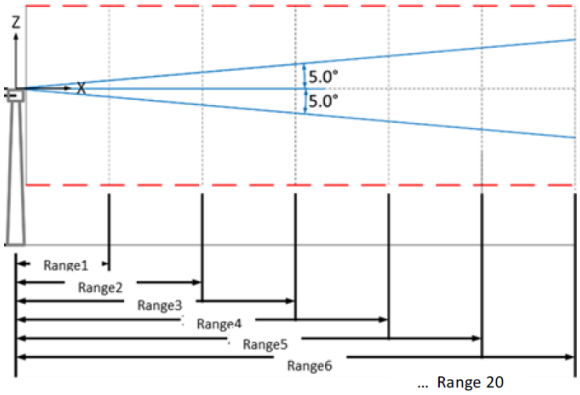

Figure 3.8: Elevation angle for the WindCube Nacelle v2.2 Long-Rang LiDAR obtained from [6]

Rayleigh length

The Rayleigh length is an important variable that is needed to determine the weighting of a Gaussian beam. Its relation is given in (2.20) in subsection 2.4.2.

Normally, the beam waist should be known in order to determine this value through the equation referred to above. As the beam waist size is unknown, the Rayleigh length is found by (3.24), retrieved from [13]. In this equation a_0 is the effective aperture radius, which is unknown for the LiDAR used for the project. Therefore, the value of $a_0 = 24mm$ characteristic of a Windscanner ZephIR continuous wave LiDAR is taken to assume a realistic value here. This is specified in [33].

The focal length f is often not provided for pulsed LiDARs, as the range gate weighting is more dominant for these LiDARs, as opposed to the weighting of the Gaussian beam. However, as also shown in [32], in fact, the weighting is influenced at or close to the focal point, as can be seen in Figure 3.9.

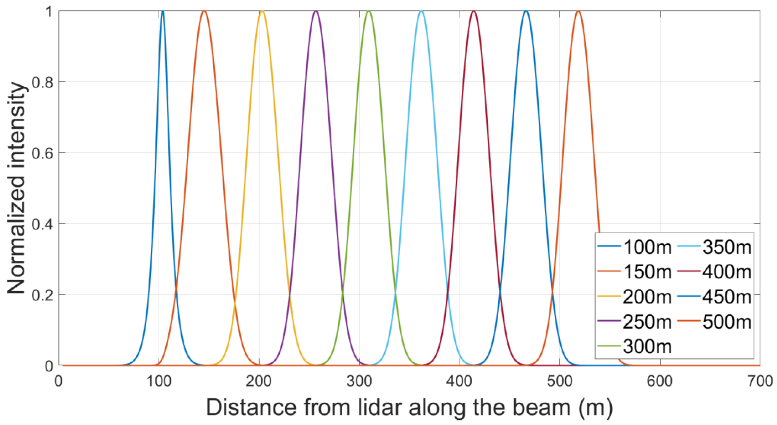

Figure 3.9: Influence of the Gaussian-beam representation part of the weighting function at the focal point [32]

The focal point determines the spread of the light intensity along the beam. The further f, the lower the peak intensity and the more spread the intensity. However, the opposite is true for f closer to the laser's origin. Due to this effect, there should be an optimum for each laser beam, depending on the furthest and closest range gates available.

The focal point f is now taken at $100\ m$, corresponding again to the continuous wave LiDAR by ZephIR [33].

The wavelength λ of the WindCube Nacelle v2.2 Long-Range configuration is given in its manual as $1.54\mu m$.

$$z_R = \frac{\lambda f^2}{\pi a_0^2} \tag{3.24}$$

Beam waist and beam radius
The beam waist can be found from the Rayleigh length, using (2.20), which results in $w_0 = 2.04\ mm$. In turn, the beam radius $w(z)$, described in (2.18), is dependent on the beam waist and the Rayleigh length and varies per position z along the beam.

Zenith and azimuth
The Zenith and Azimuth angles are the angles that describe in which direction the laser beams of the Windcube LiDAR are directed. The description of the angles defining the direction of the laser beam is visualised in Figure 2.7. The four beams and their numbering are shown in Figure 2.8. The angles used in (2.13) and (2.14) are specified by the Zenith angle θ and Azimuth angle ψ as given in Table 3.5.

Wavelength	λ [μs]	1.54
Focal length	f [m]	100
Aperture diameter	a_0 [m]	0.024
Rayleigh length	z_R [m]	8.51
Beam waist	w_0 [mm]	2.04
Pulse duration	τ_p [ns]	100
Pulse width	r_p [m]	9.01
Range gate length	Δp [m]	30
Azimuth LOS 0	ψ_0 [°]	-71.92
Azimuth LOS 1	ψ_1 [°]	71.92
Azimuth LOS 2	ψ_2 [°]	-108.08
Azimuth LOS 3	ψ_3 [°]	-251.92
Zenith	θ [°]	-15.74
Elevation	γ [°]	5
Number of range gates	N_R [$-$]	20
Minimum range gate	F_{min} [m]	50
Maximum range gate	F_{max} [m]	700

Table 3.5: Summary of LiDAR properties used in the model

3.2. LiDAR model

Now that all the inputs are known, they can be included in the LiDAR model.

3.2.1. Reference frames

Here the different reference frames used are described again. Different calculations make more sense in different reference frames. The three most important are given below.

Global reference frame

This right-handed reference frame in Figure 3.10 has its origin at the base of the tower, x pointing in the direction of the wind and z upwards. The motion data are transformed to this reference frame as input for the LiDAR model. The wind field and the coordinates of the modelled particles are similarly given in the global reference frame. In addition, the output measurement position of the LiDAR model is given in this frame as well.

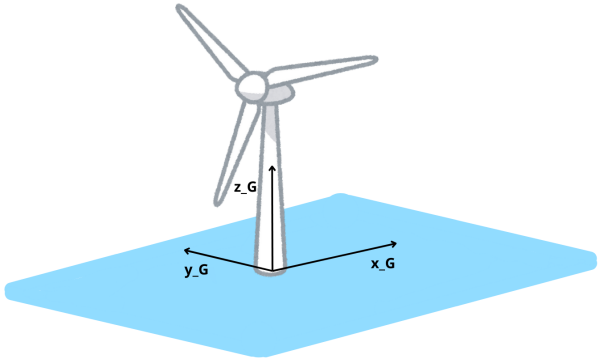

Figure 3.10: Global reference frame: $\mathcal{G}$

LiDAR reference frame

This right-handed reference frame's in Figure 3.11 origin is located at the LiDAR, directly where the beams are emitted. Here also the x-axis points towards the wind direction, and the z-axis points upward. This reference frame moves with the LiDAR. The direction vector of the laser beams is defined in this frame.

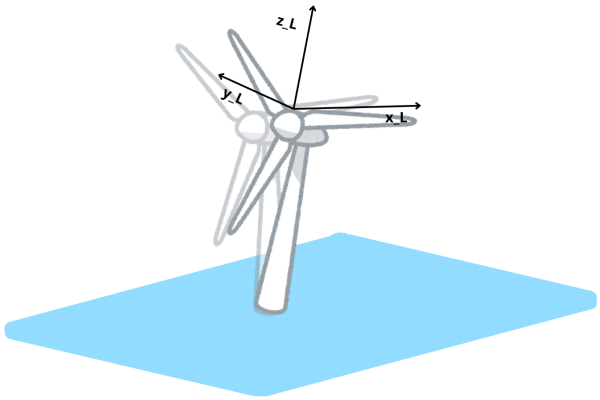

Figure 3.11: LiDAR reference frame: $\mathcal{L}$

Beam reference frame

This right-handed reference frame in Figure 3.12 has its z-axis pointing along the laser beam and x points upward. This reference frame is different for each beam. The reference frame is used for the weighting functions that determine the light intensity received for each particle.

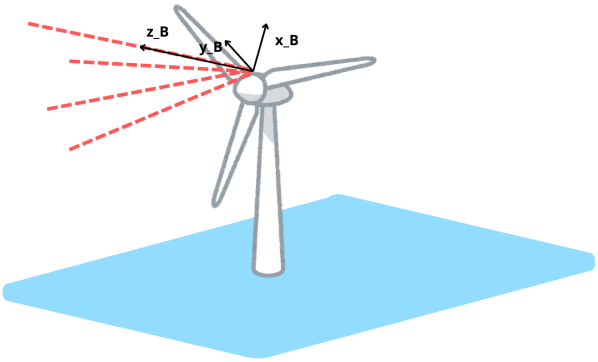

Figure 3.12: Beam reference frame: $\mathcal{B}$

3.2.2. Generation of point distribution

The measurement volume in which the LiDAR measurements are taken is modelled by a distribution of points that represent the aerosol particles reflecting the laser light. For this study a random distribution is taken. The generation of these particles is simulated in a C++ script based on the thesis of Mathieu Pellé, [35]. For this study random uniformly distributed particles are used to represent reality. These points are generated in a bounded volume that is described by a rectangular box, starting at the origin of the LiDAR and ending at the last range gate plus 50 metres. The radial limits are taken as five times the beam waist $5\ w_0$. At this location, the radial weights of the Gaussian beam will be close to zero, and the contribution of these points to the final V_{LOS} will be very small. The points are generated per beam ($\mathcal{B}$), described in subsection 3.2.1 and then transformed to the global reference frame ($\mathcal{G}$) described in subsection 3.2.1.

3.2.3. Weighting function

This weighting function considers the points in the beam reference frame. For each random point that is generated, a weight is given which is a multiplication of the weights of the Gaussian beam profile described in subsection 2.4.2 with (2.25), with the range gate weighting for the pulsed LiDAR described in (2.31). This results in the equation of the total weight represented in (3.25), also given as (2.26) in section 2.4.2.

$$w_i = W_{GaussianBeam}(x_{\mathcal{B}}, y_{\mathcal{B}}, z_{\mathcal{B}}) W_{RWF}(z_{\mathcal{B}}, F) \tag{3.25}$$

Below, for ease of reading, the equations for $W_{GaussianBeam}$ and W_{RWF} are repeated again in (3.26) and (3.27), respectively. The LiDAR properties described above in subsection 3.1.5 are used as input parameters for the weighting function.

$$W_{GaussianBeam} = \frac{z_R}{\pi(z_{\mathcal{B}}^2 + z_R^2)} \exp\left\{\left(-2\frac{r^2}{w(z_{\mathcal{B}})^2}\right)\right\} \tag{3.26}$$

$$W_{RWF}(F, r) = \frac{1}{2\Delta p}\left[Erf\left(\frac{z_{\mathcal{B}} - F + \frac{\Delta p}{2}}{r_p}\right) - Erf\left(\frac{z_{\mathcal{B}} - F - \frac{\Delta p}{2}}{r_p}\right)\right] \tag{3.27}$$

The resulting range weighting function is depicted in 3D in Figure 3.13 and in 2D in Figure 3.14 for a range gate at $400m$. The weight in the 3D plot is visualised by colours, where the lighter colours indicate a higher weight. The graph on the right shows the weighting function along the $z_{\mathcal{B}}$-axis only, as this is the most dominant direction for the light intensity with the RWF. The oscillations that are visible in Figure 3.14 are stemming from the Gaussian variation of the points that are deviating from the mean axis of the beam, so where the coordinate values in x and y are nonzero.

By plotting the RWF it became obvious that the r_p is the most dominant part of this function's uncertainty as it determines the width or the variance of the peak. The smaller the r_p, which means the smaller the

pulse duration σ, the smaller the variance and the more precise the measurement location is. Here it can thus be seen how the volume measurement influences the variance of the measurement position.

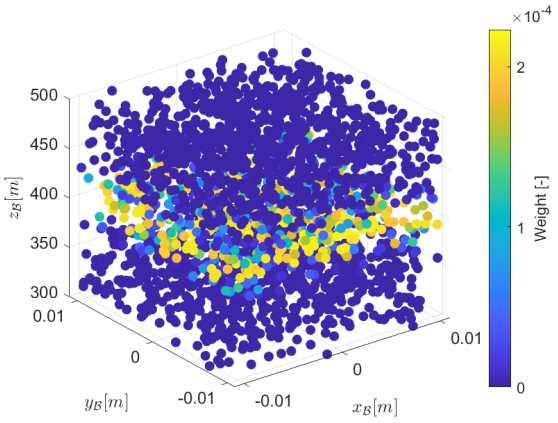

Figure 3.13: RWF of 1 beam visualised in 3D for $F = 400m$, 5000 points and $\sigma = 150ns$

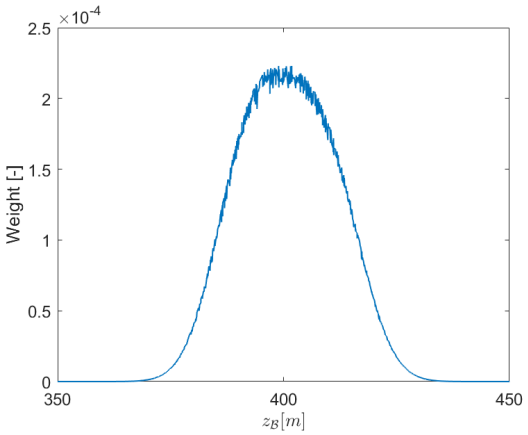

Figure 3.14: RWF of 1 beam visualised in 1D for $F = 400m$, 5000 points and $\sigma = 150ns$

3.3. Outputs

In this section, the output of the LiDAR will be discussed. A description of how they are obtained is given, as well as how the uncertainties due to volume averaging are found.

3.3.1. Position

Corrected

The correct position of the measurement is found by finding the mean position of the particles, defined as $\vec{P}_{i,\mathcal{G}} = [x_{i,\mathcal{G}}, y_{i,\mathcal{G}}, z_{i,\mathcal{G}}]^T$ in the point cloud that models the volume averaging of the LiDAR. This calculation is described by (3.28). A weighted sum of all points is taken. The variable m denotes the total number of points. The sum is then divided by the weights to get the mean of all points. This is done for all coordinates of the points, so in $x_{\mathcal{G}}$, $y_{\mathcal{G}}$ and $z_{\mathcal{G}}$. The position found for the range gate at $R = 400m$ is depicted in Figure 3.15.

$$\vec{P}_{c,\mathcal{G}} = \frac{1}{\sum_{i=1}^{m} w_i} \sum_{i=1}^{m} w_i \vec{P}_{i,\mathcal{G}} \tag{3.28}$$

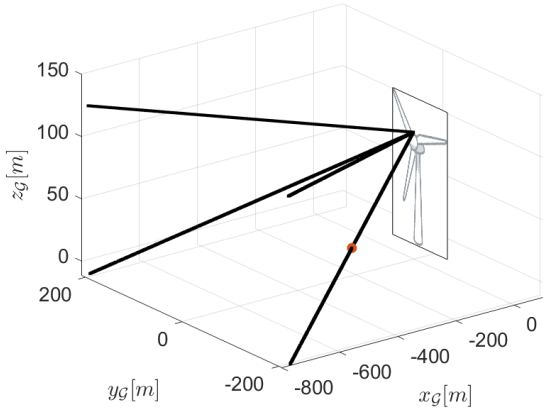

Figure 3.15: Visualisation of the measurement location (indicated with a red dot) at range gate $R = 400m$, for the fourth beam.

After the definition of the measurement position vector, the accompanying covariance matrix is given by (3.29). For which the weighted covariance matrix is used with the definition of $\vec{P}_{c,\mathcal{G}}$.

$$\mathbf{C}_{p,\mathcal{G}} = \mathcal{N} \sum_{i=1}^{m} w_i (\vec{P}_{i,\mathcal{G}} - \vec{P}_{c,\mathcal{G}})(\vec{P}_{i,\mathcal{G}} - \vec{P}_{c,\mathcal{G}})^T \tag{3.29}$$

In this equation $\mathcal{N}$ is a normalisation factor given as (3.30), which is derived in Appendix A.

$$\mathcal{N} = \frac{1}{\sum_{i=1}^{m} w_i - \frac{\sum_{i=1}^{m} w_i^2}{\sum_{i=1}^{m} w_i}} \tag{3.30}$$

The covariance matrix can be visualised in a confidence ellipse as in Figure 3.16. Here, the confidence ellipse is based on the eigenvectors of the covariance matrix. The ellipse shown contains 95 % of the weighted data points that contribute to the mean value. All points outside of this ellipse have such a small weight that their contribution to the mean measurement position can be neglected. The

confidence ellipse can be interpreted as a margin of error of the mean and can thus say something about the uncertainty of the volume measurement.

The size of the variance along z in the example plot below is $180.6m$, which corresponds to a standard deviation of $\sigma = 13.44m$, while the r_p of the RWF is $13.51m$. This is indeed what is expected for the given range weighting function and input parameters. However, the variance is quite large and has a large influence on the reconstruction of the wind speed.

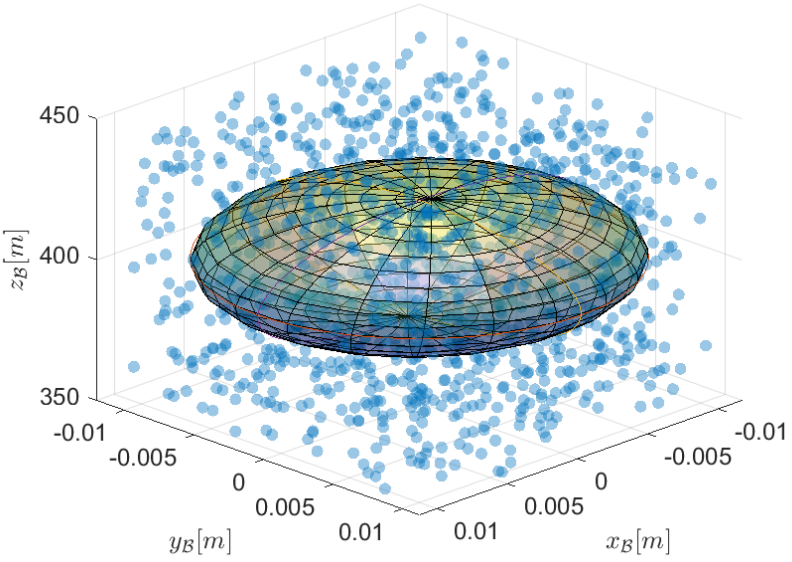

Figure 3.16: Confidence ellipse based on a 68.27 % confidence level of the covariance matrix C_p in the beam coordinate frame at range gate centre F=400 m.

Uncorrected

The uncorrected position of the LiDAR measurement assumes that the LiDAR is not moving and thus is not subject to any changes in time. Still volume averaging can be used here, but the position is taken relative to a constant initial origin position.

Unit test

The covariance of the position vector is highly dependent on the standard deviation of the RWF, described in subsection 3.2.3. In the beam coordinate frame the distribution of points, based on their weights, is Gaussian in the x and y direction and therefore the variance here should be relatively small. Along the z-direction in the direction of the beam, the variance of the points depends highly on the RWF, which uses the pulse duration in time as an input. The smaller the pulse duration, the smaller the variance of the position vector along the beam direction.

To quantify whether the found covariance matrix is indeed correct, it is transformed to the beam coordinate system and the difference between the found measurement position and the expected range gate centre is compared. To be able to judge this distance, it is expressed as the number of standard deviations (of the position vector of the point cloud) from the expected value. This is applied in (3.31) from [18], which is also called the Mahalanobis distance. This distance should be smaller than the standard deviation used as input for the RWF.

$$d_M = \sqrt{\left(\vec{P}_{c,\mathcal{B}} - \vec{P}_{c,\text{exp},\mathcal{B}}\right)^T \mathbf{C}_{p,\mathcal{B}} \left(\vec{P}_{c,\mathcal{B}} - \vec{P}_{c,\text{exp},\mathcal{B}}\right)} \tag{3.31}$$

In (3.31), $\vec{x}_{c,\text{exp},\mathcal{B}}$ is the expected position, which is the range gate centre along the beam, as expressed in (3.32). How this vector is obtained is explained in section 3.1.5.

$$\vec{x}_{c,\text{exp},\mathcal{B}} = \begin{bmatrix} 0 \\ 0 \\ \frac{F}{\cos(5^\circ)} \end{bmatrix} \tag{3.32}$$

3.3.2. Direction

Corrected

Now, the direction vector for the measurement position is equal to the position vector. For reconstruction, however, a normalised vector is required, as given in (3.33). This vector is required to be in the LiDAR reference frame $\mathcal{L}$. This is achieved by using (3.28), with the particle coordinates in the LiDAR frame as such: $\vec{P}_{i,\mathcal{L}}$.

$$\vec{d}_{n,\mathcal{L}} = \frac{\vec{P}_{c,\mathcal{L}}}{\left|\vec{P}_{c,\mathcal{L}}\right|} \tag{3.33}$$

Then the covariance for the unit direction vector is a special case, as it is desirable to only consider the covariance along the orthogonal plane of the direction vector. In this application, the covariance along the length of the unit vector does not make sense, as the vector should always be of length 1. Therefore, the projection of the points in the point cloud on the plane orthogonal to the direction vector are evaluated. In this way only the deviation in direction is being assessed, and not the deviation in length of the direction vector. In Figure 3.17 the direction vector for a simulated point cloud is given, along with the projection of the points on the orthogonal plane of this direction vector. A zoomed in version of the same figure is depicted in Figure 3.18, where the unit vectors of the yellow point cloud are also given.

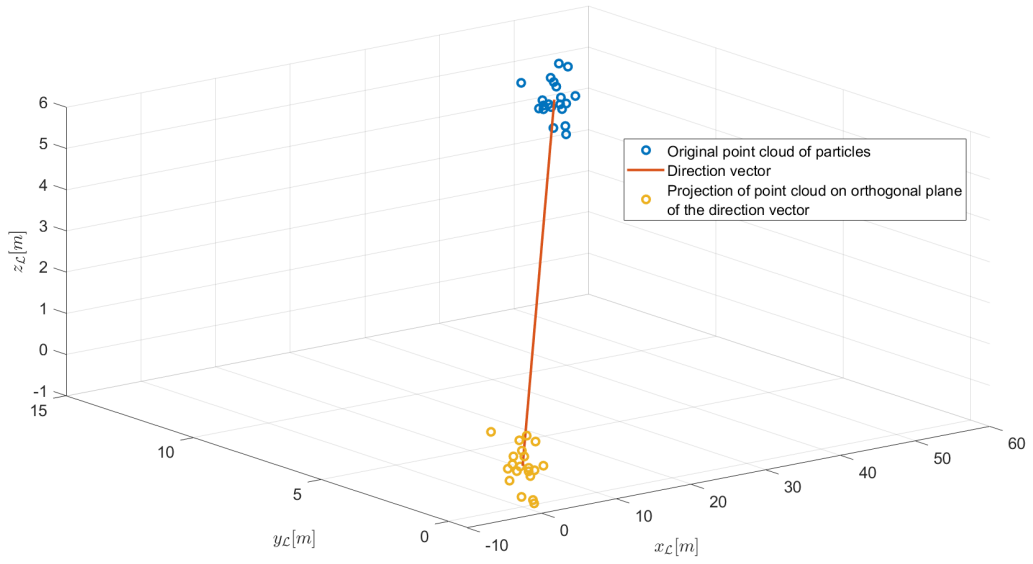

Figure 3.17: Example of a direction vector pointing to the centroid of a point cloud

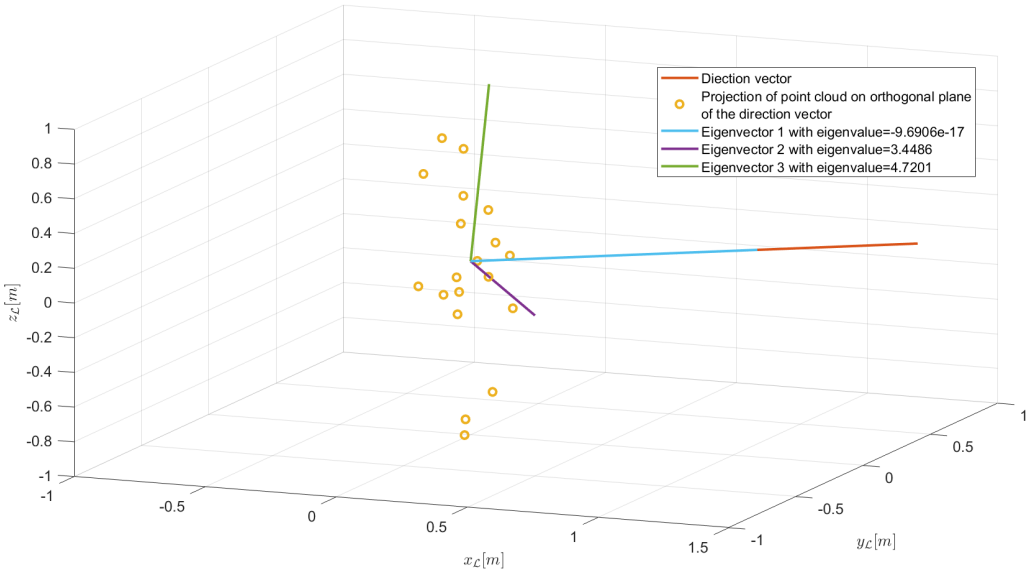

Figure 3.18: Zoomed in on projection of point cloud on orthogonal plane of direction vector of Figure 3.17, showing unit vectors of the same point cloud

The accurate covariance matrix of this yellow point cloud is given by (3.34), where the local unit direction vector in the LiDAR frame is described by (3.35).

$$\mathbf{C}_{d,\mathcal{L}} = \mathcal{N} \sum_{i=1}^{m} w_i \left[\left[\vec{d}_{i,\mathcal{L}} - \left(\vec{d}_{i,\mathcal{L}} \cdot \vec{d}_{n,\mathcal{L}} \right) \vec{d}_{n,\mathcal{L}} \right] - \vec{D} \right] \left[\left[\vec{d}_{i,\mathcal{L}} - \left(\vec{d}_{i,\mathcal{L}} \cdot \vec{d}_{n,\mathcal{L}} \right) \vec{d}_{n,\mathcal{L}} \right] - \vec{D} \right]^T \tag{3.34}$$

$$\vec{d}_{i,\mathcal{L}} = \frac{\vec{P}_{i,\mathcal{L}}}{\left| \vec{P}_{i,\mathcal{L}} \right|} \tag{3.35}$$

Here, $\vec{D}$ is given according to (3.36), which describes the mean of the yellow point cloud for which the variation along the length of the direction factor has been subtracted, by the operation $\left(\vec{d}_{i,\mathcal{L}} \cdot \vec{d}_{n,\mathcal{L}} \right) \vec{d}_{n,\mathcal{L}}$. Mathematically it can be proven that in fact (3.36) is zero. This is also confirmed with a simple Matlab programme modelling an example point cloud with a direction vector that was used to generate the plots in Figure 3.17 and Figure 3.18.

$$\vec{D} = \frac{1}{\sum_{i=1}^{m} w_i} \sum_{i=1}^{m} w_i \left[\vec{d}_{i,\mathcal{L}} - \left(\vec{d}_{i,\mathcal{L}} \cdot \vec{d}_{n,\mathcal{L}} \right) \vec{d}_{n,\mathcal{L}} \right] = 0 \tag{3.36}$$

A mathematical proof is given below in (3.37), in this equation all direction vectors $\vec{d}_n$ and $\vec{d}_i$ are given in the LiDAR reference frame $\mathcal{L}$.

$$
\begin{aligned}
\vec{D} \;=\; \vec{d_n} \;-\; & \underbrace{\frac{1}{\sum_{i=1}^{m} w_i} \sum_{i=1}^{m} w_i \left[\left(\vec{d_i} \cdot \vec{d_n} \right) \vec{d_n} \right]}_{\mathbb{E}_{\vec{d_i}} \left(\vec{d_i} \cdot \vec{d_n} \right) \vec{d_n} =} \\
& \int \left(\vec{d_i} \cdot \vec{d_n} \right) \vec{d_n} f(d_i) \mathrm{d}d_i \qquad = \\
& \int \left(\sum_{j=1}^{3} d_{ji} d_{jn} \right) \vec{d_n} f(d_i) \mathrm{d}d_i \qquad = \\
& \begin{bmatrix} \int \left(\sum_{j=1}^{3} d_{ji} d_{jn} \right) d_{n1} f(d_i) \mathrm{d}d_i \\ \int \left(\sum_{j=1}^{3} d_{ji} d_{jn} \right) d_{n2} f(d_i) \mathrm{d}d_i \\ \int \left(\sum_{j=1}^{3} d_{ji} d_{jn} \right) d_{n3} f(d_i) \mathrm{d}d_i \end{bmatrix} = \begin{bmatrix} d_{n1} \sum_{j=1}^{3} \int d_{ji} d_{jn} f(d_i) \mathrm{d}d_i \\ \dots \\ \dots \end{bmatrix} = \begin{bmatrix} d_{n1} \sum_{j=1}^{3} d_{jn} \int d_{ji} f(d_i) \mathrm{d}d_i \\ \dots \\ \dots \end{bmatrix} = \\
& \begin{bmatrix} d_{n1} \sum_{j=1}^{3} d_{jn} \mathbb{E}_{d_{ji}} \\ d_{n2} \sum_{j=1}^{3} d_{jn} \mathbb{E}_{d_{ji}} \\ d_{n3} \sum_{j=1}^{3} d_{jn} \mathbb{E}_{d_{ji}} \end{bmatrix} = \vec{d_n} \underbrace{\left(\vec{d_n} \cdot \mathbb{E}_{\vec{d_i}} \right)}_{\|\vec{d_n}\|^2 = 1^2 = 1} = \vec{d_n} \left(\vec{d_n} \cdot \vec{d_n} \right) = \vec{d_n} \\
\vec{D} \;=\; & \vec{d_n} - \vec{d_n} = 0
\end{aligned}
\tag{3.37}
$$

After this proof it can indeed be said that $\vec{D} = 0$ and thus the covariance for the unit direction vector can be taken according to (3.38).

$$
\mathbf{C}_{d,\mathcal{L}} = \mathcal{N} \sum_{i=1}^{m} w_i \left[\vec{d}_{i,\mathcal{L}} - \left(\vec{d}_{i,\mathcal{L}} \cdot \vec{d}_{n,\mathcal{L}} \right) \vec{d}_{n,\mathcal{L}} \right] \left[\vec{d}_{i,\mathcal{L}} - \left(\vec{d}_{i,\mathcal{L}} \cdot \vec{d}_{n,\mathcal{L}} \right) \vec{d}_{n,\mathcal{L}} \right]^T \tag{3.38}
$$

Uncorrected

The uncorrected direction vector that could be used for reconstruction is the direction vector that occurs if the LiDAR would not be moving. The same method is applied as in the section above, except now the points are not rotated or translated due to the LiDAR motion and thus $P_{i,\mathcal{L}} = P_{i,\mathcal{G}}$.

Unit test

The calculation of the mean direction vector $\vec{d_n}$ can be tested by comparing it to the expected direction vector which depends on the direction the laser beams point in, using the inclination and azimuth angles given by the manufacturer. This expected direction vector should of course also be rotated according to the rotation of the LiDAR due to floating motions. The dot product of these two direction vectors

should be close to 1, as expressed in (3.39). This can be checked by summing all the resulting dot products and subtracting the total number of points. The total number of points is the number of range gates per beam and the total time steps taken in the model. The answer should be close to 0.

$$\sum(\vec{d}_{n,\mathcal{L}} \cdot \vec{d}_{\text{expected},\mathcal{L}}) \approx 1 \tag{3.39}$$

Now, the covariance of the direction vector can be tested by taking the projection of the eigenvector with the smallest eigenvalue, where the eigenvalue should be close to zero, and project this onto the calculated mean direction vector. This value should be close to 1. This calculation is shown in (3.40).

$$\vec{d}_{\text{Eigenvector for } \lambda=0,\mathcal{L}} \cdot \vec{d}_{n,\mathcal{L}} \approx 1 \tag{3.40}$$

3.3.3. LOS Velocity

Uncorrected

As reference data are not available for the measured LiDAR data on the Tetrapsar demonstrator, this measurement should be simulated too. This can function as a validation case. To simulate the line of sight velocity that could be measured by a moving LiDAR, the input wind field should be taken for the particle positions that are generated to form the measurement volume, so at $\left(\frac{\vec{P}_i}{dt}\right)_{\mathcal{G}}$. From these wind field velocities, the velocity of the moving LiDAR $\left(\frac{d\vec{P}_{LiDAR}}{dt}\right)_{\mathcal{G}}$ should be subtracted, as to achieve the relative wind speed to the LiDAR. The result should then be multiplied by the direction vector of each particle to obtain the final simulated V_{LOS} as shown in (3.41). This equation is the quadrature of (2.15).

$$V_{LOS,uncorrected} = \frac{1}{\sum_{i=1}^{m} w_i} \sum_{i=1}^{m} w_i \left(\left(\frac{\vec{P}_i}{dt}\right)_{\mathcal{G}} - \left(\frac{d\vec{P}_{LiDAR}}{dt}\right)_{\mathcal{G}} \right) \cdot \frac{\vec{P}_{i,\mathcal{L}}}{\left|\vec{P}_{i,\mathcal{L}}\right|} \tag{3.41}$$

Corrected

Lastly, the offset of the line of sight velocity, that is the projection of the LiDAR velocity along the laser beams that should be subtracted from the measured V_{LOS} as to get the V_{LOS} with only a contribution of the wind speed. This can be obtained per particle by taking the scalar product of the LiDAR translational velocity along the local unit direction vector. Then the mean of each local line of sight velocity is taken, as shown in (3.42).

$$V_{LOS,Offset} = \frac{1}{\sum_{i=1}^{m} w_i} \sum_{i=1}^{m} w_i \left(\frac{d\vec{P}_{LiDAR}}{dt}\right)_{\mathcal{G}} \cdot \frac{\vec{P}_{i,\mathcal{L}}}{\left|\vec{P}_{i,\mathcal{L}}\right|} \tag{3.42}$$

The variance is obtained by applying the accepted equation for variance, as shown in (3.43).

$$\sigma_v^2 = \mathcal{N} \sum_{i=1}^{m} w_i \left(\left(\frac{d\vec{P}_{LiDAR}}{dt}\right)_{\mathcal{G}} \cdot \frac{\vec{P}_{i,\mathcal{L}}}{\left|\vec{P}_{i,\mathcal{L}}\right|} - V_{LOS,Offset} \right)^2 \tag{3.43}$$

Then the corrected line of sight velocity, where the velocity due to the movement of the LiDAR is taken out, is obtained by Equation 3.44.

$$V_{LOS,corrected} = V_{LOS,uncorrected} + V_{LOS,Offset} \tag{3.44}$$

Unit test

The application of the V_{LOS} functions can be tested by performing the same operation, as described above, except now the dot product is taken with the mean direction vector itself instead of with the wind and/or LiDAR velocity, as done in (3.45). If then all resulting values are close to 1, it proves that the weights are normalised and that the multiplication with the direction vector is correct and close to the mean direction vector. To check if all values are close to 1, the sum of all resulting V_{LOS} is taken and if the difference between that and the number of points considered is close to zero, the unit test is successful. This test can be applied to both (3.41) and (3.42).

$$V_{LOS} = \frac{1}{\sum_{i=1}^{m} w_i} \sum_{i=1}^{m} w_i \vec{d}_{n,\mathcal{L}} \cdot \frac{\vec{P}_{i,\mathcal{L}}}{\left|\vec{P}_{i,\mathcal{L}}\right|} \approx 1 \tag{3.45}$$

The variance of the line of sight velocity can be tested by checking the convergence with an increasing number of points within the beam volume, resulting in Figure 3.19.

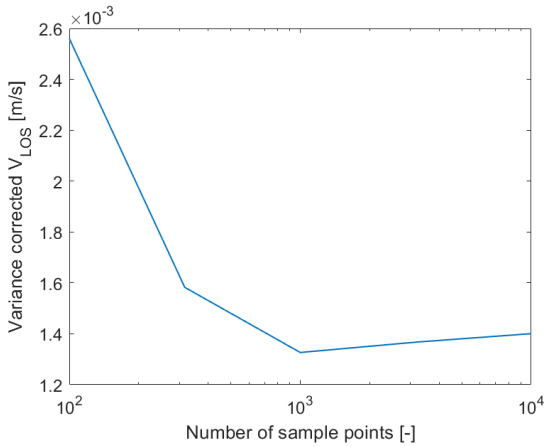

Figure 3.19: Convergence of the variance of V_{LOS}

3.3.4. Point measurement

A point measurement is a good test case for the LiDAR model. When using only a point measurement, as described in Section 2.4.2, the uncertainty of volume averaging is removed. This case can therefore be used as a comparison of the effect of the uncertainty of volume averaging on the uncertainty of the reconstructed wind field.

When a point measurement is applied, the beam will consist only of particles present on the $z_{\mathcal{B}}$-axis of the beam at exactly the range gate centres $z_{\mathcal{B}} = F_{beam}$, as visualised in Figure 3.20. Practically, this means that when applying the weighting function (3.25) for a particular F, $w_i \approx 1$ for each $z_{i,\mathcal{B}} = F$, while w_i for all the other coordinates is close to zero. Therefore, the position is measured exactly at the range gate centre location, the direction vector is the unit vector of that position. The line of sight velocity is applied to the resultant direction vector. No variance or covariance is present in any of the outputs.

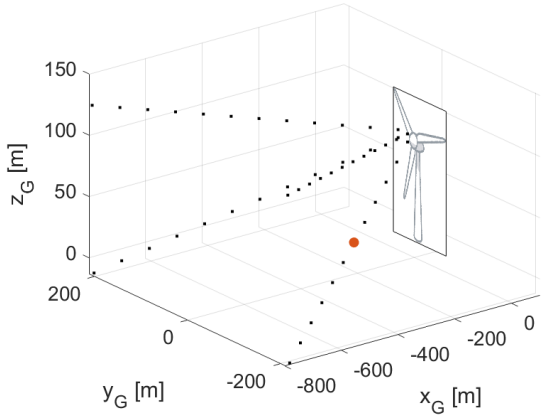

Figure 3.20: Visualisation of the point measurement case

3.4. Reconstruction

To reconstruct the wind field from the given V_{LOS}, direction and measurement position from the LiDAR model, the least squares method is used. This is also described in section 2.6. Now an explanation will be given of the set up of the weighted non-linear least squares that is applied to the line of sight velocity which, in turn, is described by the power law. The (3.46) should be minimised, which is the same as (2.45) and is copied here for reading convenience. For the Gauss-Newton algorithm, (3.54) is used to find the parameters U_{ref} and α. The reference height z_{ref} is kept constant at the height of the hub.

$$S = \sum_{i=1}^{N} \left(V_{LOS,i} - U_{ref} \left(\frac{H_i}{z_{ref}} \right)^{\alpha} \cdot d_{x,i} \right)^2 = \sum_{i=1}^{N} (V_{LOS,i} - f(H_i, d_{x,i}, \vec{\beta})^2) = \sum_{i=1}^{N} r_i^2 \tag{3.46}$$

The non-linear system, for which the values U_{ref} and α should be determined, is governed by the following observation equation: (3.47). In this equation H_i is the observed height, $d_{x,i}$ is the x-value of the unit direction vector. $V_{LOS,i}$ is the corresponding response value. The vector $\vec{\beta}$ contains the unknown values $\vec{\beta} = (U_{ref}, \alpha)$.

$$f(H_i, d_x, i, \vec{\beta}) = U_{ref} \left(\frac{H_i}{z_{ref}} \right)^{\alpha} \cdot d_{x,i} \tag{3.47}$$

As this system is non-linear, it should be linearised with a first-order Taylor approximation, as (3.48), where k indicates the guess of the values in β^k for iteration step k.

$$f(H_i, d_{x,i}, \vec{\beta}) \approx f(H_i, d_{x,i}, \vec{\beta}^k) + \frac{\partial f(H_i, d_{x,i}, \vec{\beta}^k)}{\partial U_{ref}} (U_{ref} - U_{ref}^k) + \frac{\partial f(H_i, d_{x,i}, \vec{\beta}^k)}{\partial \alpha} (\alpha - \alpha^k) \tag{3.48}$$

The partial derivatives of f for each observation i can be summarised in vector form as a Jacobian, as expressed in (3.49). The Jacobian is dependent on the unknown values U_{ref} and α and thus changes per iteration to find the minimum of the least squares. The Jacobian is a $2XN$ matrix with the partial derivatives of f with respect to U_{ref} and α, with N the number of observations in V_{LOS}, d_x and H.

$$\mathbf{J}^k = \left[\frac{\partial \vec{f}}{\partial U_{ref}}, \frac{\partial \vec{f}}{\partial \alpha} \right] = \left[-\vec{d}_x \left(\frac{\vec{z}}{z_{ref}} \right)^{\alpha^k}, \vec{d}_x U_{ref}^k \left(\frac{\vec{z}}{z_{ref}} \right)^{\alpha^k} \ln\left(\frac{\vec{z}}{z_{ref}} \right) \right] \tag{3.49}$$

The difference between the unknown values can be vectorised as well, resulting in (3.50).

$$\Delta \vec{\beta}^k = \begin{bmatrix} U_{ref} - U_{ref}^k \\ \alpha - \alpha^k \end{bmatrix} \tag{3.50}$$

Now, the difference between the response value $V_{LOS,i}$ and the solution of the forward model in iteration k is found with (3.51). The solution of the forward model is equal to (3.47) with the values of the unknown variables for the current iteration step k filled in, making $\beta = \beta^k$ and $V_{LOS,i}$ is approximated by the linearised (3.48).

$$\Delta V_{LOS,i} = (V_{LOS,i} - f(H_i, d_{x,i}, \vec{\beta^k}) \approx \mathbf{J}^k \Delta \vec{\beta}^k \tag{3.51}$$

Now, the equation to be solved to find $\Delta \vec{\beta}^k$ for one iteration becomes (3.52).

$$((\mathbf{J}^k)^T \mathbf{J}^k) \Delta \vec{\beta}^k = (\mathbf{J}^k)^T \Delta \vec{V}_{LOS} \tag{3.52}$$

The unknown variables are then found in each iteration with (3.53).

$$\vec{\beta} = \vec{\beta}^k + \Delta\vec{\beta}^k \tag{3.53}$$

This cycle of iterations is to be repeated until a certain threshold is reached, where β^k is small enough. This implies that the estimation for $\vec{\beta}$ and thus U_{ref} and α does not change much more and the solution is converged.

The iteration limit in this research is set to $\Delta\beta = 1 \cdot 10^{-10}$.

This estimate can be improved by including the variance of $\Delta V_{LOS,i}$ in terms of weights. The updated version of (3.52) including the weighting changes to (3.54).

$$((\mathbf{J}^k)^T \mathbf{W} \mathbf{J}^k)\Delta\vec{\beta}^k = (\mathbf{J}^k)^T \mathbf{W} \Delta\vec{V}_{LOS} \tag{3.54}$$

The variance in $\Delta V_{LOS,i}$ can be found by using uncertainty propagation as described in subsection 2.7.1, applied to (3.55). This equation takes as input the variances in V_{LOS}, d_x and H, found in section 3.3. In this analysis, it is assumed that there is no correlation between the variance of V_{LOS}, d_x and H. However, it is known that there is a correlation between these, because they all depend on the weighted mean of the point distribution. Specifying this correlation as an output of the LiDAR model will therefore improve the reconstruction and reduce its uncertainty.

$$\text{Var}(\Delta V_{LOS,i}) = \frac{\partial \Delta V_{LOS}}{\partial V_{LOS}}^2 \text{Var}(V_{LOS,i}) + \frac{\partial \Delta V_{LOS}}{\partial H}^2 \text{Var}(H_i) + \frac{\partial \Delta V_{LOS}}{\partial d_x}^2 \text{Var}(d_{x,i}) \tag{3.55}$$

Finally, the weight is taken as a diagonal matrix with size NXN where each diagonal entry is the inverse of $\text{Var}(\Delta V_{LOS,i})$ for each measurement, as to ensure that the measurements with a higher variance have a smaller contribution to the reconstruction and vice versa.

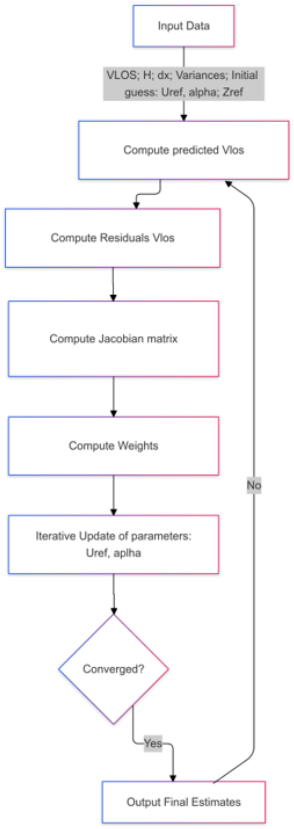

Figure 3.21: Schematic of weighted least squares for wind field reconstruction

3.5. Uncertainty quantification reconstructed wind field

The goal of this research is to quantify the uncertainty in the corrected wind measurements. This will be achieved by subtracting the reconstructed wind field from the original wind field, and comparing the error in the two reconstruction parameters. In subsection 3.1.4 it was explained that a power law is used to quantify the input wind field, which is characterised by a reference wind speed at hub height U_{ref} and a power term α. These two parameters are then reconstructed according to the method explained in section 3.4.

The error percentage between the reconstructed parameters and the original parameters is found using (3.56). Similarly, the error for α is found with a similar equation, taking the percentage error of the reconstructed α_{rec} relative to the original α_{ori}.

$$E_{U_{ref}} = \frac{\overline{U}_{ref,rec} - U_{ref,ori}}{U_{ref,ori}} \tag{3.56}$$

The effect of different parameters of the model on the final error of the reconstructed wind field is quantified by changing only this error and determining the impact this has on the final error. To quantify the uncertainty present in the motion measurements, a Monte Carlo simulation is performed. For the correction model a Gaussian white noise is added to the input motion data, with a mean equal to the motion at a corresponding time step and a variance equal to that found according to subsection 3.1.2. This is then repeated until convergence of the Monte Carlo analysis and a mean and variance of the reconstructed wind field error can be found.

4

Error and uncertainty of wind field

In this chapter, the results of the LiDAR modelling and uncertainty quantifications explained in chapter 3 are presented. The order of the research overview is followed as visualised in Figure 2.1 and repeated in Figure 4.1. First, the uncertainty in the motions is quantified in section 4.1. Then the uncertainty of the LiDAR model itself is discussed in section 4.2, touching upon the LiDAR parameters, as well as the model outputs. After that, the uncertainty of the reconstruction is presented in section 4.3.

When the uncertainties in all separate parts are quantified, the final uncertainty of the whole model can be quantified, so the uncertainty in the reconstructed wind field is evaluated in section 4.4. Both the uncertainty due to the motion will be assessed, while in addition a comparison will be made on how this uncertainty improves when using the correction method.

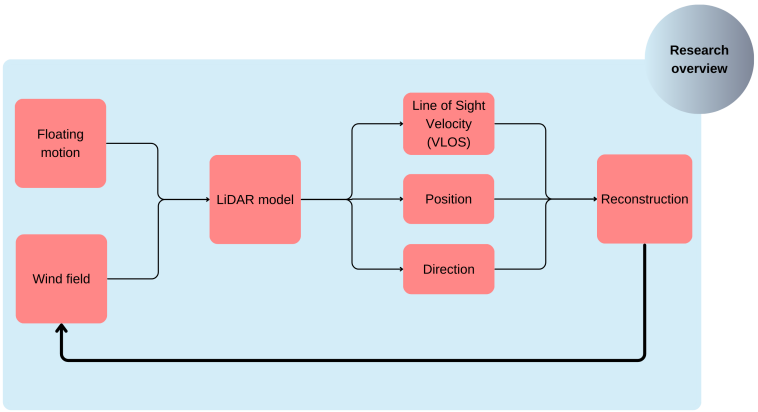

Figure 4.1: Research Steps Overview

4.1. Uncertainty of motion input

The effect of applying the regression as explained in subsection 3.1.2 will be specified here.

The frequency response of the motions says something about which components of the motion contribute most to the final plots in the time domain. In this way, it can also be shown how much the regression captures of the motion's frequencies.

The single-sided amplitude spectrum is plotted for the 2DOF data on the left side of Figure 4.2. Yhe graphs are cut-off at a random frequency for confidentiality reaons. Distinct peaks are visible, which can be expected from the sinusoidal oscillations in Figure 3.2. Different waves with different frequencies and amplitudes are modulated on top of each other. The simulated 2DOF data has a sampling rate of $0.02s$ or $50Hz$, while the sampling rate of the regression is set at $1s$ to match the LiDAR beam sampling interval. Consequently, the orange regression curve stops at $f = 0.5Hz$, in accordance with (4.1) for a single sided amplitude spectrum of the Fourier transformed data. In equation f_s is the actual sampling frequency and f is half of that, to exclude everything above the Nyquist frequency.

$$f = \frac{f_s}{2} \tag{4.1}$$

The time step for regression is set at 4 seconds, because the LiDAR data per beam is an integral average over 4 seconds too. In the graph, this corresponds to a frequency $f = 0.125Hz$. This is explained more extensively in section 3.1.2. At this frequency, the peaks at higher frequencies are filtered out, as can be seen when comparing the simulation and regression data in Figure 4.2. In addition, an artificial peak occurs in the regression data for 2DOF motions, slightly increasing the regression fit error. These peaks are indicated by a black circle in Figure 4.2c and Figure 4.2e.

For the 6DOF motions the data are more noisy and the peaks are less pronounced. With a regression sampling time step of $t_{regr} = 4s$ and a fitted data sampling interval of $t_{fit} = 1s$, the regression fails to capture the amplitude peaks at around indicated by a circle for position, velocity and orientation. As a side note, the velocity fit exhibits more pronounced peaks at this frequency compared to the position fit, as the velocity is the derivative of the position data. It is suspected that the circled peak stems from a higher tower mode.

The resulting standard deviation of the regressed motion parameters is summarised in Table 4.1 for the 2DOF motion and in Table 4.2 for 6DOF motions.

Surge	Xvel	Pitch
m	m/s	deg
0.001	0.003	0.004

Table 4.1: Standard deviation σ due to regression fit for 2DOF simulated motions

Surge	Sway	Heave	Xvel	Yvel	Zvel	Roll	Pitch	Yaw
m	m	m	m/s	m/s	m/s	deg	deg	deg
0.011	0.011	0.001	0.041	0.037	0.003	0.022	0.020	0.013

Table 4.2: Standard deviation σ due to regression fit for 6DOF simulated motions

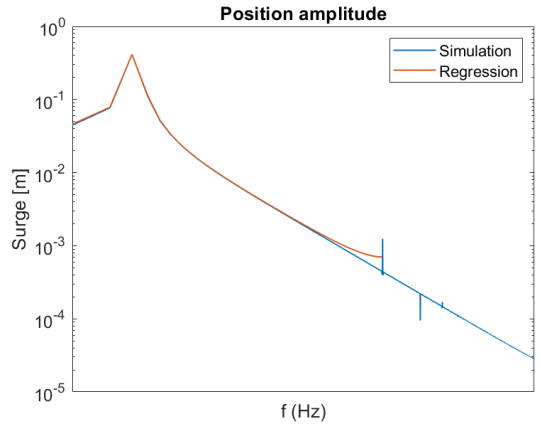

(a) Surge 2DOF

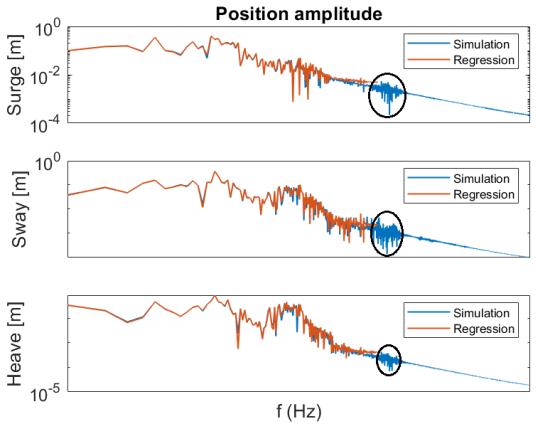

(b) Positions 6DOF

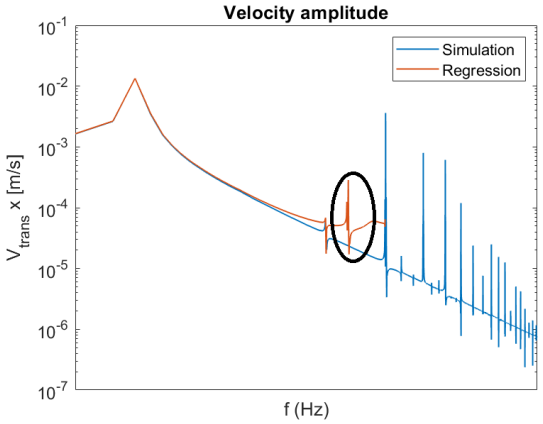

(c) X-Velocity 2DOF

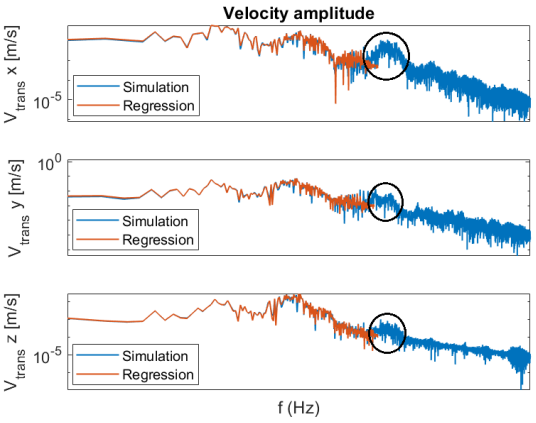

(d) Velocities 6DOF

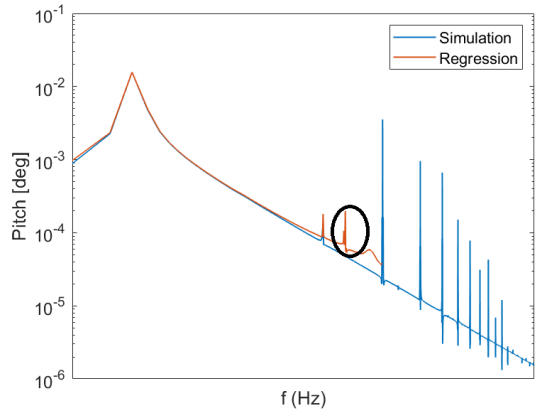

(e) Pitch 2DOF

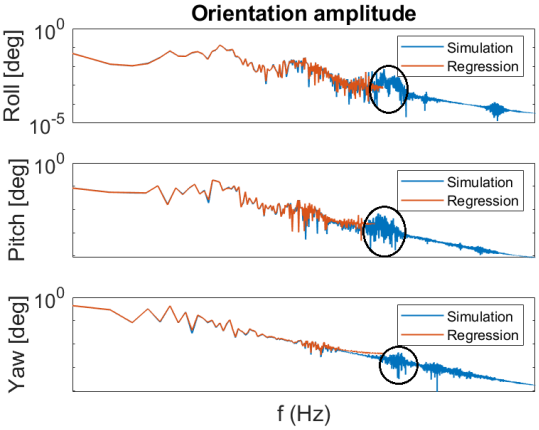

(f) Orientation 6DOF

Figure 4.2: Single-sided amplitude spectrum obtained from FFT of simulated 2DOF data (on the left) and 6DOF data(on the right)

4.2. Uncertainty of LiDAR model

In this section, the uncertainty of the LiDAR will be quantified. This will be done without including any motion of the LiDAR to eliminate motion uncertainty and focus solely on LiDAR uncertainty.

4.2.1. Limitations

It should be noted that the uncertainty due to volume averaging is expected to be small because a simple power law is used as an input for the simulation here. The power law which models the shear in wind velocity. However, in reality, turbulence is present, which causes a larger variation of particle velocities within the measurement volume and thus increases the LiDAR uncertainty due to volume averaging.

Next to the volume averaging uncertainty, more environmental factors influence the quality of the measurement. This is briefly touched upon at the beginning of this thesis report in section 2.4. The consistency of the particles in the air is important. The quality of the LiDAR measurement depends on the concentration of aerosols in the atmosphere and the question of whether there is precipitation or fog. This will block some of the measurements. Seeing as these environmental factors change per measurement situation, the uncertainty also fluctuates with these environmental changes.

In addition to environmental factors influencing the uncertainty, the LiDAR instrument itself also introduces errors in the measurement of V_{LOS}. That is, in terms of calibration and mounting errors, as well as Carrier to Noise Ratio (CNR) of the LiDAR, depending on the power of the received signal.

4.2.2. Volume averaging uncertainty

The uncertainty in volume averaging is quantified by comparing the error percentages of the parameters of the reconstructed wind field, obtained with section 3.5. The error percentage of a point measurement as described in subsection 3.3.4 is compared to a measurement in which volume averaging is applied. The difference between these two says something about the error due to the volume averaging effect of the LiDAR model.

The resulting change in error percentage is shown in Table 4.4. These results are found when no motion is applied to the system and the LiDAR model settings are applied as given in Table 4.3.

Start Range Gate	[m]	50
Last Range Gate	[m]	350
Range Gate Spacing	[m]	50
U_{ref}	[m/s]	10
α	[-]	0.1429
Hub height	[m]	90

Table 4.3: Parameters of the numerical LiDAR model

When comparing the error of the point measurement with that of a volume averaged measurement of the simulated LiDAR, it is clear that the error increases, as expected. More uncertainty is introduced about where the measurement is taken exactly.

This uncertainty is expressed in the measurement position itself, but also in the direction vector and the line of sight velocity, which both depend on the measurement position. How contributing covariances and variance are found is described extensively in section 3.3.

It can be said that the error percentage of the reconstructed wind field is very small for both cases and there is a significant increase in error of 3 orders of magnitude when including volume averaging. However, for modelling this error only a power law is used as an input wind field. If a turbulent wind field was included, this error would be larger. Therefore, the errors stated here are not realistic when compared to real world examples.

From Table 4.4 it can also be deduced that the error percentage is smaller when covariance and variance are taken into account using weighted least squares to correct for uncertainty due to volume averaging. In section 3.4 it is explained how this correction is performed with (3.55). What is also

clear from the results in Table 4.4 is that the reference wind speed U_{ref} is underestimated, while the power α is overestimated. Next to that, the percentage error for α is higher. Be that as it may, the error percentages here are still very small.

	$E_{U_{ref}}$ [%]	E_{α} [%]
Point	-0.0000000006	0.0000000081
Volume *uncorrected* for volume (co)variance	-0.0004018400	0.0070021000
Volume *corrected* for volume (co)variance	-0.0003264200	0.0048768300

Table 4.4: Reconstruction error of wind field without any motion, for a LiDAR simulated as a point measurement per range gate and a simulation where volume averaging is included

4.2.3. Effect of LiDAR parameters

In this section, the influence of the most important LiDAR parameters on the weighting function is discussed to evaluate volume averaging.

Pulse duration

As discussed in subsection 3.3.1, the most dominant factor in the uncertainty of the Range Weighting Function is the pulse duration τ_p. The W_{RWF} and its parameters are described in Section 2.4.2, where the range weighting is modelled by a Gaussian pulse and a rectangular windowing function. In Figure 4.3 the response of the weights to the change in τ_p is visualised for a range gate at $F = 400m$. The variance and thus the uncertainty of the measurement position along the z-axis of the beam increase with higher pulse durations. This effect is quantified in Table 4.5, where the corresponding standard deviations of the graphs are shown in Figure 4.3 along with the analogous r_p, the half width of the pulse. In Table 4.5 also the effect on the final reconstructed wind field is shown, which consistently increases with increasing pulse duration.

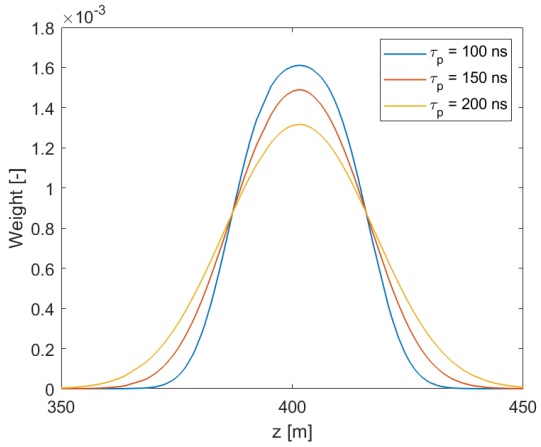

Figure 4.3: Effect of changing pulse duration τ_p

τ_p [ns]	r_p [m]	$\sigma_{z,\mathcal{B}}$ [m]	$E_{U_{ref}}$ [%]	E_{α} [%]
100	9	11	-0.0003	0.005
150	14	13	-0.0006	0.008
200	18	16	-0.0009	0.014

Table 4.5: Effect of doubling pulse duration on total uncertainty

Gaussian beam weighting

The focal length and Rayleigh length of the project specific WindCube LiDAR are unknown and assumed to be reasonable industry standard values. Therefore, it is important to consider the effect of these values and of the Gaussian weighting itself. as was already mentioned in section 3.1.5.

A figure similar to Figure 3.9 is generated for comparison of what the resulting weights of the Gaussian and the RWF look like in Figure 4.4. The weights are normalised to have a peak at 1, by dividing by their maximum, for ease of comparison. For the actual application, a normalisation is applied by dividing by their sum to ensure that all weights for a specific range gate sum up to one. Only the weights along the z-axis of the beam are considered and deviations from zero of $x_{\mathcal{B}}$ and $y_{\mathcal{B}}$ contributing to the Gaussian exponential are ignored in this figure for clarity, but are taken into account for the volume averaging. It can be seen that only at the location where the focal length and the location of the range gate match, that is, at $100m$, the shape of the weighting function changes. The standard deviation of the position along the z-axis of the beam drops from $\sigma_{z,\mathcal{B}} = 11m$ to $\sigma_{z,\mathcal{B}} = 9m$. The total effect of this uncertainty is small, since this only applies to one range gate out of 13 for range gates from $50m$ to $700m$ with a spacing of $50m$.

	$\sigma_{z,\mathcal{B}}$ [m]
RWF weighting	11
RWF + Gaussian weighting	9

Table 4.6: Effect of Gaussian beam weighting on measurement position uncertainty

In literature, often the Gaussian beam weighting described here as part of the total weighting function in (3.25) is ignored. This is done, because the effect of the change in total uncertainty due to Gaussian beam weighting is not noticeable in the reconstructed wind field. This can be deduced from the fact that only the weighting function where the range gate location and focal length coincide is really affected, as is found in the analysis above.

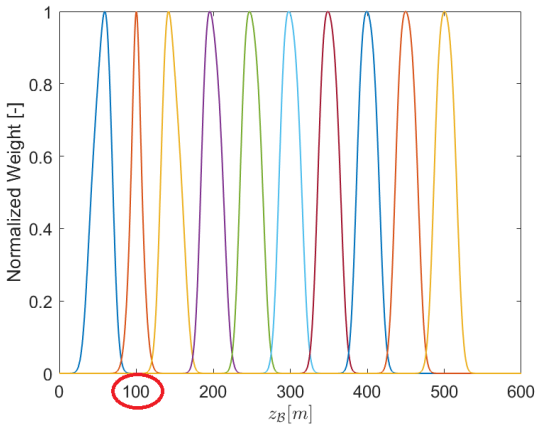

Figure 4.4: Influence of Gaussian weighting on total RWF

4.3. Uncertainty of WLSQ reconstruction method

The error of the reconstruction method can be quantified by quantifying the error percentage according to section 3.5, without introducing errors anywhere before the modelling loop. This means that no motion is introduced and point measurements as opposed to volume measurements are used for the LiDAR model. In Table 4.4 the error percentage is given as $-6E^{-10}\%$ for U_{ref} and $8.1E^{-9}\%$. This is so small, especially compared to the effect of other errors that this error is not dominant for the final reconstructed wind field uncertainty. No uncertainty arises from point measurements as the variance of the reconstructed wind field is within machine precision.

4.3.1. Influence first guess

The first guess of the parameters U_{ref} and α cannot be determined beforehand as the wind field is still to be estimated. However, with physical knowledge, it can be said that the reference wind speed should be between 0 and $50m/s$, since the speed range that the LiDAR can measure ends at $50m/s$, as can be found in the manual [6]. The power law exponent is limited from 0.11 to 0.65 according to [23]. The closer the initial guess to the actual values, the faster the system will converge. For an initial guess that is too far off, the system might not converge at all. This is tested to within the physical limits, by taking both very high power law exponent and a high reference wind speed and taking both these values on the lower limit. In addition, a high reference wind speed with a low α and vice versa are combined. For the common value used for the analysis here of $U_{ref} = 9m/s$ and $\alpha = 0.12$, the system converges in 4 iterations if harmonic motions are applied. For the extremities mentioned above the convergence increases slightly to a maximum of 7 when no motion is applied and the system always converges. Therefore, the initial guess of U_{ref} and α is not of concern.

4.3.2. Limitations

There are some limitations to the non linear weighted least squares method, because a linear approximation of a non-linear equation is used here, using a first order Taylor series. Therefore, $\vec{\hat{\beta}}$ is not the best linear unbiased estimator for $\vec{\beta}$. Due to the fact that $\vec{\hat{\beta}}$ is non-linear, it is also not normally distributed. However, if the Taylor approximation for linearisation is a good enough approximation, that is, the higher order terms are small, then the estimator can still be assumed to be normally distributed.

4.4. Uncertainty of reconstructed wind field

Now that the uncertainties of the different steps in the modelling cycle are quantified, the final uncertainty of the reconstructed wind field can be given, due to the uncertainties described above. First, the uncertainty of the uncorrected motion will be presented in order to compare this to the uncertainty of the correction method. Also, the influences of the separate DOFs are analysed, focussing on harmonic motions. Afterwards, the uncertainty due to 2DOF motions is given and subsequently that for 6DOF motions.

4.4.1. Comparison harmonic, 2DOF and 6DOF motion

When movement is added as input to the LiDAR simulation and volume averaging is used, the error percentages of the reconstructed wind field for different types of motion are given as in Table 4.7. These are the uncorrected error percentages. Compared to Table 4.4, the error due to motion is much larger. It is at least 2 orders of magnitude larger compared to the corrected volume averaged measurements without motion.

The error resulting from the harmonic motions tabulated in Table 4.7 averages out very well compared to the 2DOF and 6DOF motions. The error percentage is one to two orders of magnitude smaller than the simulated 2DOF and 6DOF motions. The reason for this is that the harmonic motions are fluctuating around a zero-mean for all motions. In contrast, the 2DOF has an offset for the mean in pitch, as pictured in Figure 3.2 and the 6DOF motion as shown in Figure 3.3 has an offset for the mean in all directions translational and rotational displacements. This will cause a bias in the effect of the motion over a 10-minute average, resulting in higher errors. From [21] it was already concluded that the main cause of the error is induced by the offset from the mean of the pitch angle. This will also be confirmed in the following sections. The errors are expected to be higher if a turbulent wind field would be analysed as an input instead of the power law here.

	$E_{U_{ref}}$ [%]	E_{α} [%]
Harmonic motion	-0.283	0.560
2DOF motion	2.513	-24.780
6DOF motion	2.953	-29.540

Table 4.7: Uncertainty of measurements with uncorrected motions

4.4.2. Individual DOF motion influence on uncertainty

It is desirable to know which motions of the floating turbine would induce the largest uncertainty in the reconstructed wind field. This has been done by leaving all harmonic motions equal to zero, except for 1 DOF. The amplitude change is analysed by changing it from $1m$ or $1°$ to $5m$ or $5°$, while keeping the original periods as recorded in Table 3.1. For an analysis of the change in period it is changed from 10 to 50 seconds, while now the amplitudes are kept the same at $2.5m$ or $2.5°$. The resulting difference between the error percentages with a higher and lower amplitude or period are given in Table 4.8 and visualised in a histogram in Figure 4.6 for U_{ref} and in Figure 4.7 for α. As a reminder of the different DOF of a floating offshore wind turbine, Figure 4.5 is presented again.

	$E_{U_{ref}}$ [%]		E_{α} [%]	
	Amp	Period	Amp	Period
Surge	0.08	-0.02	0.67	-0.55
Sway	0.01	-0.01	0.07	-0.16
Heave	0.01	0.00	0.20	-0.05
Roll	0.19	-0.01	0.13	-0.25
Pitch	0.46	-0.03	2.47	0.92
Yaw	0.13	-0.04	1.31	-1.16

Table 4.8: Error percentage of reconstructed wind field parameters for a 500% increase of the input parameters of harmonic motions

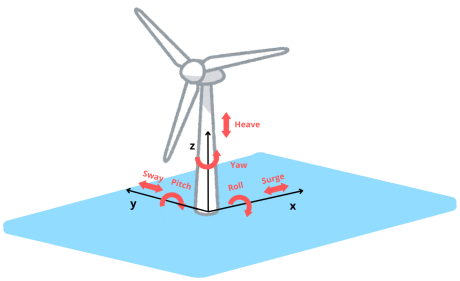

Figure 4.5: DOF visualised for a floating offshore wind turbine

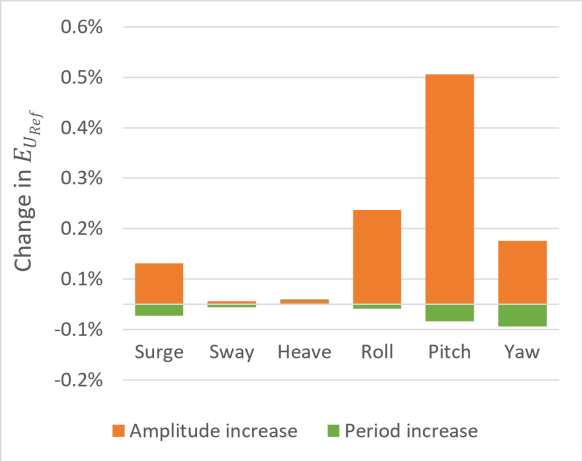

Figure 4.6: Influence of separate DOF on reconstructed reference wind speed U_{ref}'s uncertainty, with harmonic motion

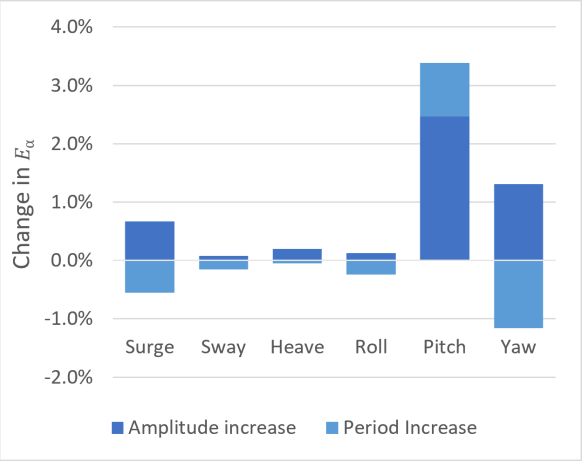

Figure 4.7: Influence of separate DOF on reconstructed power law exponent α's uncertainty, with harmonic motion

Reference wind speed vs power law exponent

Moreover, there is a clear distinction between the size of each DOF's influence on the reconstructed U_{ref} and α parameters. This is also what could be noticed before in Table 4.4 and Table 4.7. That is, the error percentage in the parameter α is much higher than in U_{ref}. If the error of α is larger, this means that the reconstructed wind speed further away from the hub height is more erroneous, while it is most precise at the hub height itself.

When only interest is taken to wind speed at hub height, the uncorrected wind field velocity error percentage is smaller than at locations further away from the hub. Depending on the accuracy required, it might be acceptable to not correct the data for hub height.

Influence of period vs amplitude

From Figure 4.6 and Figure 4.7 it is clear that the uncertainty increases when the amplitude of the harmonic motions is increased. In general the opposite is true for an increase in period, save for the pitch motion. For this motion the uncertainty increases for an increase in both amplitude and period. From Figure 4.6 it can also be seen that the influence of increasing the period by a factor 5 has a much smaller influence on the reconstructed U_{ref} compared to the same increase factor applied to the amplitude.

Surge

For the surge movement, only a change in velocity occurs, no change in direction or z-position is present. For a positive motion backwards, the measured velocity relative to the wind turbine is smaller than without any motion. This thus reduces the reference wind speed and power law component, resulting in an underestimation of both.

Sway

The error percentage of the reconstructed wind field due to the sway motion is very small, because a wind field that is described by a power law does not change for motions sideways. Only a position change in z has an effect. Neither does a sway motion give a direction change or add to the horizontal velocity. However, the velocity in y-direction induced by a sway motion, will be added to the V_{LOS} by the component of the laser beam that points in the y-direction. Therefore, still a small offset is present for sway motions.

Heave

For a heave motion the z-position changes, meaning the LiDAR will measure higher velocities for each beam for a positive heave motion due to the wind shear described by a power law. In addition, a small part of the induced velocity in z-direction will contribute to the V_{LOS}. Although the opposite is expected to be true, here U_{ref} is underestimated, while α is overestimated for a harmonic heave motion.

Roll

The rolling motion of a floating wind turbine does not create any additional velocities in x-direction, only small contributions in velocity components in y and z direction. However, a direction and position change do occur. A rolling motion will move the hub height of the turbine down. For the rolling motion an underestimation of the reconstructed U_{ref} and α is present.

Pitch

From Figure 4.6 and Figure 4.7 it is clear that the pitch motion has the highest influence on the final reconstructed wind field error. This is also predicted in [21]. The large influence of pitch motion on the total error can be explained by the fact that when the turbine pitches, the direction in which the laser beams of the LiDAR point changes, as depicted in Figure 4.8. A position change indicates a change in wind speed, as a shear is present in the wind field. Next to that, the direction vector changes and points more upwards, resulting in an overestimation of the contribution of the horizontal wind speed to the V_{LOS}. These direction changes do not occur for the translational DOF. In addition to this, the pitching motion induces a horizontal (and vertical) velocity that will add to the velocity measured by the LiDAR.

By knowing that the pitch motion has the largest effect on the reconstructed wind field uncertainty, this could be the focus of further measurement corrections if limited motion data are available. This could be the case when, for example, no IMU is installed on the turbine and only the inclinometer of the LiDAR can be used, which can only measure orientation changes.

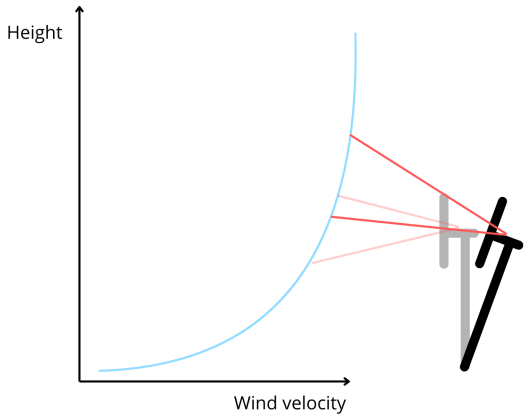

Figure 4.8: Effect of floating turbine pitching motion on LiDAR wind velocity measurement

Yaw

In yaw motion the wind turbine does not change the vertical measurement position. Each range gate still measures at the same height. However, the direction of measurement changes, which results in more of the wind speed vector being projected onto the laser beam than is actually measured by the LiDAR. For the outer two beams, when looking from above, this error is larger. Therefore, a different wind speed will be measured for the same height. Next to an error in direction, also an offset of the wind speed is present due to the yawing motion of the turbine.

In summary, from the analysis above, it can be said that a velocity change in x-direction has the largest effect, because the laser beams generally point in that direction. This occurs for surge and, in a lesser sense, for pitch movements and even slighter for yaw movements. For a similar reason the direction changes in pitch and yaw have a larger effect, as these turn away from the x-axis, along which the main part of the laser beams point. The only position change relevant for a power law input wind field is a position change in z, because the wind field only changes with height. This occurs for pitch, heave and, in a lesser sense, for roll motions.

It should be noted that this analysis has only been applied to separate DOF, while in reality the motions are coupled and so is their effect on the reconstructed wind field error percentages. However, it does give a clear indication of the major actors on error and uncertainty caused by motions of the LiDAR.

4.4.3. Uncertainty 2 DOF simulated motion & power law

Now that the effect of different parameters on the uncorrected wind field has been explored, also the uncertainty of the corrected reconstructed wind field can be determined. In this section the focus will be on the 2DOF motion input data. For a Monte Carlo simulation with 500 simulations for a Gaussian varying motion input into the correction algorithm as described by Table 4.1, the output uncertainty is described by Table 4.9.

It is clear that the correction algorithm greatly reduced the the error percentage. At the same time in correcting the measurements, uncertainty is added to the reconstructed wind field, because of the uncertainty present in the motion data, quantified in Table 4.1. In the second row of Table 4.9, the motion correction results are presented for when no correction of the volume averaging uncertainty is taken into account. The third row presents the case for the results of motion correction where also the uncertainty of the volume averaging is corrected for. This correction is done using weighted least squares as described with (3.55) in section 3.4.

	$E_{U_{ref}}$ [%]	E_{α} [%]
Uncorrected	2.5130	-24.7800
Uncorrected volume (co)variance + Corrected motion +	-0.0004 $\pm$ 0.0013	-0.0029 $\pm$ 0.0212
Corrected volume (co)variance + Corrected motion	-0.0003 $\pm$ 0.0014	-0.0030 $\pm$ 0.0212

Table 4.9: Reconstruction error of wind field with 2 DOF motion with uncertainty as in Table 4.1, for a LiDAR simulated with volume averaging

The convergence of the Monte Carlo simulation in U_{ref} and α can respectively be seen in Figure 4.9 and Figure 4.10. Here, α converges faster than U_{ref}. Also, it is clear that both parameters are underestimated here, which is also indicated by the minus sign in Table 4.9.

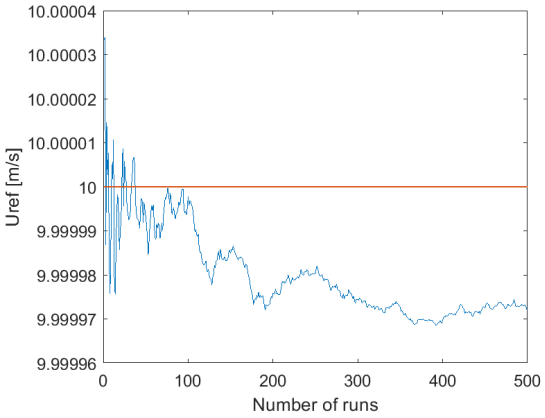

Figure 4.9: Convergence of U_{ref} with Monte Carlo simulation of varying 2DOF motion in correction algorithm

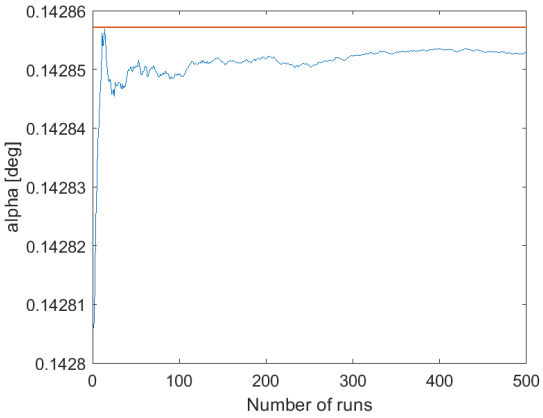

Figure 4.10: Convergence of α with Monte Carlo simulation of varying 2DOF motion in correction algorithm

The wind field over height, corresponding to the power law parameters of the wind fields, is visualised in Figure 4.11. The uncertainty of the corrected wind field velocity is too small to see in the graph, but the corrected mean overlaps with the two tolerance lines separated by σ. A striking fact to deduce from this graph is that for this specific motion, the difference in velocity is highest for the lowest altitude graphed, while the original and uncorrected wind field overlap around a height of $175m$. At this height the bias in the measurements cancel out and thus the uncorrected and corrected graph overlap. At a hub height of $H_{hub} \approx 90m$ the offset between the original and the uncorrected wind speed should be 2.5%, according to Table 4.9, resulting in a wind speed of $10.25m/s$ for the uncorrected wind speed, compared to the $10m/s$ of the original wind speed. The portion of the wind field that is measured above the LiDAR is larger than the portion below, because the wind turbine is offset by a mean pitch of around

$2.82°$, as depicted in Figure 3.2. This results in a vertical measurement offset of approximately $35m$ for the furthest range gate.

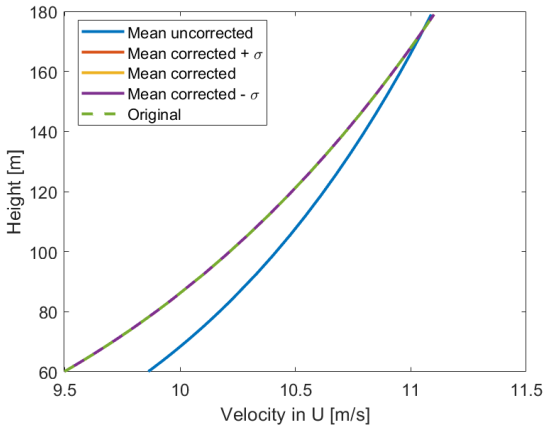

Figure 4.11: Reconstructed wind field for 2DOF, showing uncorrected and corrected with standard deviation

As was concluded in subsection 4.4.2, the pitch motion has the largest effect on the error percentage of the uncorrected motion. Therefore, it might be interesting to see what the effect of pitch is here. Especially, because an offset from zero is present, as shown in Figure 3.2, which would increase the pitch motion's influence on the error of the reconstructed wind field parameters. In [21] it was found that the mean pitch amplitude has the largest effect on the error between the reconstructed wind field and the original.

This effect is researched by applying the 2DOF to a point measurement as described in subsection 3.3.4, so without applying any volume averaging. With the result of nu volume averaging uncertainty to be present and thus assuming that the LiDAR perfectly models the measurement. The variance of these results in Table 4.10, because only point measurements are considered. First, all motions of the 2DOF are included, that is, surge, pitch and x-velocity. The outcome is then compared to a simulation in which only the 2DOF pitch is applied. The last case considered is the same pitch motion, but centred around a zero mean. The results are summarised in Table 4.10. As expected, the resulting error of only the pitch motion is almost the same as when all 3 motions are applied. This confirms the dominance of a mean pitch.

	$E_{U_{ref}}$ [%]	E_{α} [%]
Surge, Pitch, Vx	1.410	-27.370
Pitch only	1.403	-27.370
Pitch around zero mean	0.000	-0.001

Table 4.10: Effect of pitch 2DOF motion on point measurement

The difference between the original wind field and the uncorrected or corrected reconstructed wind fields is given as an error percentage for the wind velocity per height in Figure 4.12 and Figure 4.13, respectively. The x-axis of Figure 4.13 is a much smaller range than that of Figure 4.12, meaning the error percentage is smaller. The error decreases with height because for higher heights the power law exponent has a smaller influence. The shear in the wind field, namely, decreases with wind height. In Figure 4.13 the effect of correcting for the (co)variance of volume averaging can be seen by comparing the graph where a weighting based on the volume averaging variance is used and the one where this correction is not applied. The percentage of error in the velocity of the wind field U is larger for the uncorrected volume variance. When comparing the graphed results to Table 4.9 it is interesting to see that even though indeed the $E_{U_{ref}}$ is smaller for the corrected volume averaging variance, the E_{α} is slightly larger. This difference is so small that the effect of an increase in E_{α} cannot be seen, the decrease in $E_{U_{ref}}$ prevails.

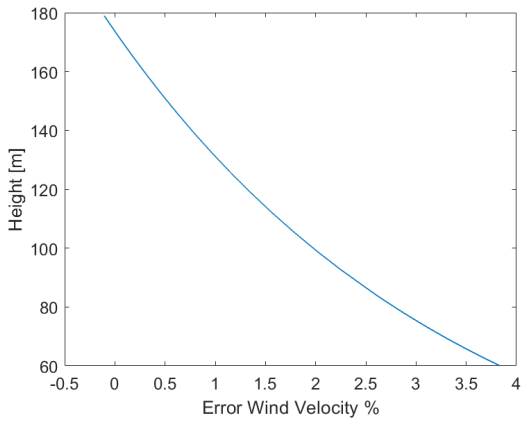

Figure 4.12: Uncorrected error percentage of reconstructed wind field for 2DOF motions

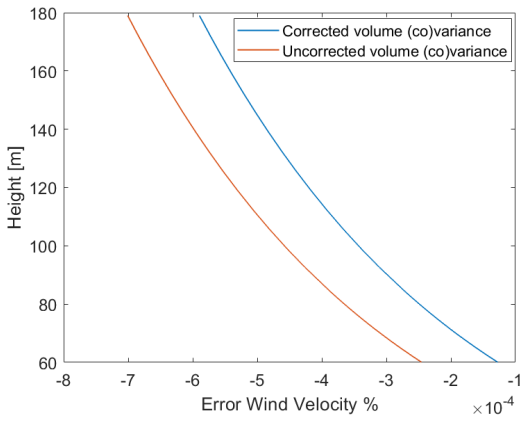

Figure 4.13: Error percentage of reconstructed wind field for corrected 2DOF motions

4.4.4. Uncertainty 6 DOF motion

The same results for a 2DOF will now be presented for a simulated 6DOF case. The uncertainties given in Table 4.2 are implemented as the standard deviation of Gaussian white noise to the correction algorithm. The motion parameters are randomly sampled from this Gaussian distribution for 500 times. The resulting outputs of the reconstructed wind field are summarised in Table 4.11. Similarly to the 2DOF case, the error in the reconstructed wind field parameters for uncorrected floater motions is compared to the erro for corrected motions. In the second row of Table 4.9, the uncertainty due to volume averaging is not corrected using (3.55) from section 3.4, while row 3 does have this correction applied.

For the 6DOf motion case also a clear increase in uncertainty can be seen for the case where volume averaging uncertainty is corrected. This is expected as the more corrections are applied, the more uncertainties are added to the model. The fact that this uncertainty is so large even increased the error percentage for U_{ref}. In the last paragraph of this section this is explored further.

It is clear that the error of the reconstructed wind field is greatly reduced when the motion correction algorithm is applied. The errors for the corrected case are so small because a power law wind profile is used as an input. This is a simplified representation of a realistic wind field, and the error due to volume averaging, as well as the uncertainty would increase if a turbulent wind field were applied.

	$E_{U_{ref}}$ [%]	E_{α} [%]
Uncorrected	2.953	-29.540
Corrected motion + Uncorrected volume (co)variance	0.001 $\pm$ 0.019	-0.028 $\pm$ 0.310
Corrected motion + Corrected volume (co)variance	0.003 $\pm$ 0.085	-0.018 $\pm$ 0.605

Table 4.11: Reconstruction error of wind field with 6 DOF motion with uncertainty as in Table 4.2, for a LiDAR simulated with volume averaging

The convergence of the Monte Carlo simulation applied to obtain the results in Table 4.11 is shown in Figure 4.14 and Figure 4.15, for U_{ref} and α, respectively. Unlike the convergence of the 2DOF results, the reference wind speed U_{ref} converges faster than α. For this particular motion case, also U_{ref} is overestimated, while α is underestimated.

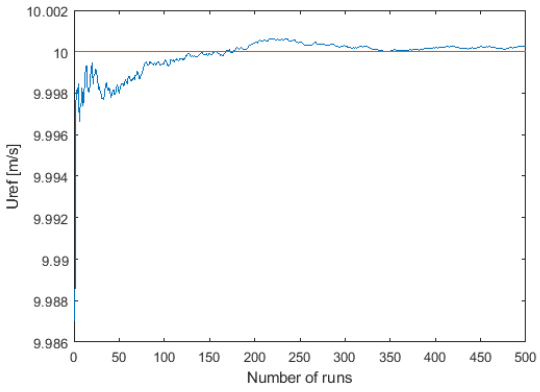

Figure 4.14: Convergence of U_{ref} with Monte Carlo simulation of varying 6DOF motion in correction algorithm

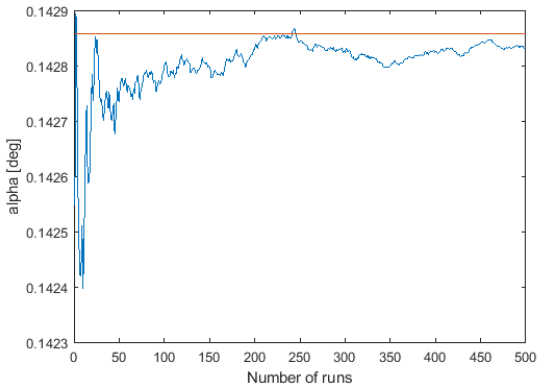

Figure 4.15: Convergence of α with Monte Carlo simulation of varying 6DOF motion in correction algorithm

A noticeable fact to be deduced for this more complicated motion case that is closer to reality, is that the standard deviation of the reconstructed wind field increased, when compared to 2DOF data. This can also be found in Figure 4.16, where the mean and its standard deviation are pictured. The reason for this is that a larger standard deviation is applied to the input of motions in the correction algorithm as recorded in Table 4.2.

Comparable to the 2DOF case in Figure 4.11, the difference between the original and uncorrected wind field is largest for the lowest height pictured. Again, close to $175m$ the two graphs cross. This crossing also means that for larger heights, above $175m$, the uncorrected wind field underestimates the original wind speed. For lower heights the opposite is true.

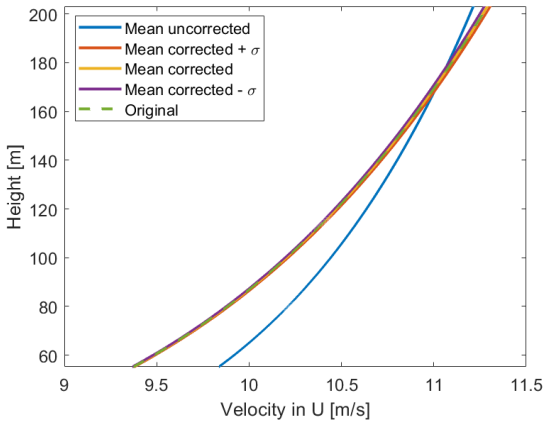

Figure 4.16: Reconstructed wind field for 6DOF, showing uncorrected and corrected with standard deviation

The influence of the pitching motion on the error percentage of the uncorrected wind field is researched by taking pitching motion only as an input. The result is recorded in Table 4.12. As was the case for the 2DOF case and as explored in subsection 4.4.2 indeed the pitch motion is the largest source of error in the reconstructed wind field.

	$E_{U_{ref}}$ [%]	E_{α} [%]
6DOF motions	0.133	-18.270
Pitch only	0.071	-17.220

Table 4.12: Effect of pitch 6DOF motion on uncorrected point measurement

Lastly, also a visualisation of the error percentage of the wind field over height is given for the uncorrected wind field in Figure 4.17 and for the corrected one in Figure 4.18. There is quite a large difference of the error percentage for different heights, due to the error in the power law exponent. Leaving much larger errors at lower heights, compared to the upper heights, as is also confirmed in the difference between the corrected and uncorrected graphs in Figure 4.16. When the difference between the corrected wind fields is compared in Figure 4.18, where for one correction of variance due to volume averaging is applied, as done in (3.55) from section 3.4 and for the other it is not, then the corrected version has a higher error up until a height of $158m$. In Table 4.11 it is clear that while indeed $E_{u_{ref}}$ is increased for the volume averaging variance correction, E_α is reduced. However, from Figure 4.18 it can be said that for the most part the error percentage of the fully corrected reconstructed wind field is higher.

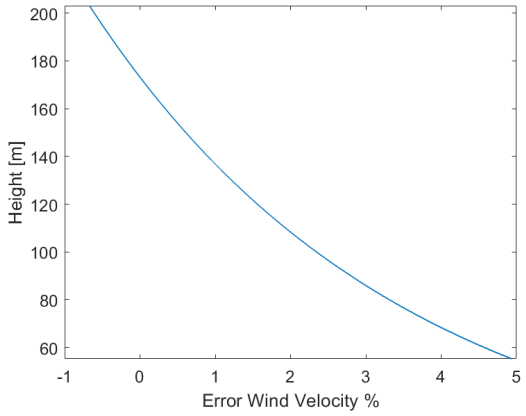

Figure 4.17: Uncorrected error percentage of reconstructed wind field for 6DOF motions

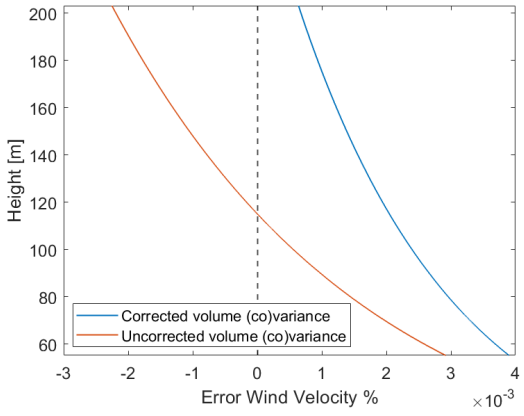

Figure 4.18: Error percentage of reconstructed wind field for corrected 6DOF motions

4.4.5. Comparison to real data uncertainties

The results presented in this chapter so far show a very positive outlook on the effect of correcting the LiDAR measurements for the movements of the floating turbine, showing a large reduction in error with a small variance. Although this is true, the analysis has thus far been limited to simulations, and a comparison with real-world conditions is necessary.

In practice, motion uncertainty is larger than that captured by regression. An uncertainty is present within the IMU measurement device, for example. In addition, the LiDAR's uncertainty is not only dependent on volume averaging, but additional sources of error occur, such as errors due to turbulent fluctuations.

In Table 4.13 the uncertainties in motion found with regression of the simulated 6DOF motion data are compared with the uncertainties of the IMU as found in [41]. The specifications of the IMU uncertainty hold for marine and subsea applications and refer to post-processed data with an outage duration of GNSS satellite contact of 30 seconds. In reality, this standard deviation depends on many factors and changes for each measurement, but this comparison provides a useful baseline for assessing order-of-magnitude differences. For the velocities and angles, the comparison in Table 4.13 confirms that the simulated noise levels are within the expected range. However, for positional changes, the simulation yields a much smaller standard deviation than that reported in the IMU manual. This discrepancy could pose a problem when correcting for positional changes. As discussed in subsection 4.4.2, positional changes have a relatively minor impact on overall error compared to orientation changes. If also the wind field uncertainty due to the uncertainty of these position measurement exceeds the bias caused by position changes, applying a correction may not be beneficial. The total effect of applying the uncertainties as the maximum standard deviations of the IMU in all DOF's is studied in this section.

	Surge	Sway	Heave	Xvel	Yvel	Zvel	Roll	Pitch	Yaw
	m	m	m	m/s	m/s	m/s	deg	deg	deg
Simulation	0.011	0.011	0.001	0.041	0.037	0.003	0.022	0.020	0.013
IMU	1.000	1.000	0.300	0.050	0.050	0.030	0.040	0.040	0.050

Table 4.13: Standard deviation σ due to regression fit for 6DOF simulated motions

In reality, also the uncertainty in the line of sight velocity will be higher because of additional uncertainties due to more complex and detailed wind fields and LiDAR models. For example, time averaging in the LiDAR or turbulent fluctuations in the wind field will add to the total LiDAR model uncertainty. For an order of magnitude comparison, the mean standard deviations of the line of sight velocities of real measurements of the WindCube Nacelle Lon-Range LiDAR mounted on the Tetraspar demonstrator over a period of 1 hour are compared with the computation of volume averaged uncertainty in the V_{LOS} in Table 4.14. This uncertainty is then applied in a similar way as how the motion uncertainty is applied. The standard deviation in Table 4.14 for the actual WindCube LiDAR is used in a Gaussian white noise that is added to the modelled V_{LOS}. By increasing the uncertainty in V_{LOS}, a more realistic test case can be simulated, providing insight into how the results would appear under real-world conditions

	$\overline{\sigma}_{V_{LOS}}$ [m/s]
Simulation	0.0124
Actual WindCube LiDAR	1.0000

Table 4.14: Comparison of mean standard deviation of V_{LOS}

The resulting error percentages in the reconstructed U_{ref} and α for the corrected motion data are given in Table 4.15. The comparison is done without volume averaging, assuming to measure at the exact location of the range gates. This is done because the uncertainty due to volume averaging is replaced by the uncertainty given in Table 4.14. This is applied by taking the exact V_{LOS} for a given point and adding a Gaussian white noise with a standard deviation of $\sigma = 1m/s$ to it.

	$E_{U_{ref}}$ [%]	E_{α} [%]
Simulation	0.003 $\pm$ 0.085	-0.018 $\pm$ 0.605
Reality	0.349 $\pm$ 0.185	-0.552 $\pm$ 5.571

Table 4.15: Reconstruction error of wind field with 6 DOF motion with uncertainty as in Table 4.13, for a LiDAR simulated with exact point measurements that are not volume averaged

When accounting for higher uncertainties in the modelling process, both the standard deviation and the error of the reconstructed wind field increase. As shown in Figure 4.19, this wind field exhibits a greater variance from the mean, and the mean deviates more from the original wind field compared to Figure 4.16. Nevertheless, the correction still improves accuracy compared to the uncorrected wind field, even when one standard deviation is added to the corrected mean. Thus, with 68 % confidence, the correction method produces a wind field measurement that is closer to reality. For heights between 88 and $200m$, where the mean of the uncorrected wind field falls within one standard deviation of the corrected wind field, the uncertainty exceeds the bias correction. However, applying this correction, despite the increase in variance, remains preferable to leaving the bias uncorrected.

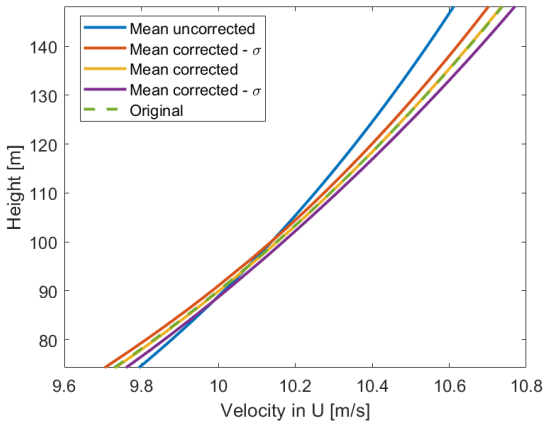

Figure 4.19: Velocity wind field with σ added to motion and V_{LOS} based on real measurements

5

Conclusion and recommendations

After having presented the background theory, the methodology used for the correction and the final results, the final conclusions to answer the research question can be drawn. In addition, recommendations for further research have been identified.

5.1. Conclusion

The objective of developing a correction algorithm for the influence of floater motions on LiDAR measurements and quantifying the uncertainty of this method was captured in the following research question: *What are the uncertainties in corrected wind speed measurements taken from a nacelle-mounted LiDAR on a floating wind turbine?*

This question will be answered in this concluding chapter with the help of the results and methodologies presented in the previous chapters. First, the sub-questions that will guide the answer to the main research question will be answered.

SQ1. How is the correction of a wind velocity LiDAR measurement on a floating wind turbine performed with the use of a numerical LiDAR model?
This question has been answered by developing a numerical LiDAR model. The principles of LiDAR measurements are explained in section 2.4, while the correction method is detailed in section 3.2. The main takeaway from these sections is that all three outputs of the LiDAR measurement should be corrected. That is, the measurement position, the direction in which the laser beams point, and V_{LOS}.

SQ2. What are the specific floater motions that influence LiDAR wind speed measurements and how significant is their impact?
The motions of a floating offshore wind turbine are briefly described in section 2.2. Then the specific motions used in this thesis, namely the simulated harmonic motions, 2DOF and 6DOF motions, are detailed in subsection 3.1.1. Each successive motion model introduces increasing complexity, with the 6DOF motion being the most realistic.

Among these motions, pitch motion has the most significant impact on the reconstructed wind field. This is primarily because pitch motion has a non-zero mean, leading to a bias in the measured wind speed. For a harmonic motion, a pitch motion with a zero mean results in an increase in the error percentage of U_{ref} and α of 0.46% and 2.47%, respectively, due to an increase in pitch angle from 1 to $5°$. This change is fairly large compared to the mean error percentage of a 500% change in amplitude for each individual DOF of 0.15% and 0.81%.

For a 2DOF motion, it can be concluded from Table 4.10 that the largest portion of the error of the reconstructed wind field stems from the pitch motion. If no mean pitch would be present, the error is reduced a lot from 1.403000% to 0.000003% for U_{ref} and from -27.370% to -0.001% for α.

The reconstructed velocity field that is uncorrected for the motion experiences a similar dependency

on the pitch motion, where in Table 4.12 again the largest part of the error can be attributed to the pitch motion.

SQ3. What are the uncertainties of the involved input parameters, that is, of the LiDAR parameters, the LiDAR modelling and the motion input?
The uncertainty of the motion input is calculated with a least-squares regression method as explained in subsection 3.1.2 and the resulting uncertainties are given in section 4.1. The uncertainty of the measurements depends on the sampling time chosen for the regression method. The larger the sampling frequency, the less oscillations are captured, and more of the motion is defined as noise. The sampling time is set at 4 seconds to match the time over which the LiDAR measurements are averaged.

No uncertainty is assumed to be present in the wind field described by a power law.

The uncertainty of the LiDAR parameters is unknown, but a sensitivity study of the effect of different parameters is performed in section 4.2. From this, it can be concluded that the range weighting function has the largest effect on the error in the correction of the reconstructed wind field. The LiDAR parameter, which in turn influences this weighting the most, is the pulse duration, which induces an uncertainty of the measured position along the laser beam of $\sigma_{z,\mathcal{B}} 11m$, for the applied pulse duration of $\tau_p = 100ns$.

The error induced by the LiDAR model was found by excluding motions and their uncertainties, and the resulting error due to volume averaging was found to be -0.0004% for U_{ref} and 0.0070% for α, the variance connected to these values is within machine precision.

The uncertainty of the reconstruction method as explained in section 3.4 is within machine precision, and the error percentage caused by only the reconstruction method is very small, too, in the order of E^{-9} and E^{-10}. This is documented as the error percentages for a point measurement in Table 4.4, as explained in section 4.3. This holds because a lot of wind speed measurements that deviate only slightly per height are available for the reconstruction of a 10-minute average of a wind field described by a power law.

SQ4. What is the most dominant source of error in the reconstructed wind field?
From the results in chapter 4 it is clear that the largest source of error in the cases analysed here is the motion of the LiDAR. Especially for the more complicated BHawC motions that also have a non-zero pitch. The error percentage is between 20 and 30% for the power law exponent and above 2% for the reference wind speed. The motion with the biggest influence is then the mean pitch motion, as is answered in the first sub-question. The error due to motion is much larger than the error due to volume averaging, for the case of a power law wind field. The error of volume averaging will increase if a turbulent wind field is present, inducing larger variations within the LiDAR's measurement volume. However, it is expected that the error caused by motions will remain larger than the error due to volume averaging. If the different factors of volume averaging are compared, then the pulse duration in the range gate weighting function has the largest effect. When the pulse duration is doubled, the error percentage approximately triples for both U_{ref} and α.

SQ5. What is the remaining error of the corrected wind speed measurements?
The remaining error of the correction is quantified in error percentages as described in section 3.5. The reconstructed wind field is compared to the input wind field and the relative error is tabulated in percentages. The error percentage for 2DOF motion is reduced from 2.5130% to -0.0003% for U_{ref} and from -24.7800% to -0.0030% for α. This is summarised in Table 4.9. For the 6DOF motion, a similar reduction in error is present, from 2.953% to 0.003% for the reference wind speed and from 29.540% to -0.0018% for the power law exponent. These results are also summarised as in Table 4.11. It is clear that the correction method used in this thesis is very effective in reducing the error of the LiDAR wind speed that occurs due to floating turbine motions because the errors are greatly reduced. Now, the last thing to do is to answer the main research question by putting this correction in to perspective in terms of additional uncertainties that arise from performing this correction.

RQ: What are the uncertainties in corrected wind speed measurements taken from a nacelle-mounted LiDAR on a floating wind turbine?
Uncertainties in the reconstructed wind field increase when more parameters are corrected. This can be concluded from Table 4.11, where an uncertainty increase of the reconstructed wind field was found for

the correction of the variance due to volume averaging in the output parameters of the LiDAR model. It increased from 0.019% to 0.085% for U_{ref} and from 0.310% to 0.605% in α. Even with this large increase in uncertainty and with a standard deviation larger than the mean error, the correction method is still noticeably better than when no correction is applied. This gives a good idea of how effective this method is in correcting LiDAR measurements for floating offshore wind turbines.

5.2. Recommendations

In this section, recommendations for future work will be given.

First of all, more detail can be included in the methodology used here to make the analysis more complete and closer to reality. For example, instead of using a power law, a turbulent wind model can be used as input to the LiDAR model. This will induce larger errors and uncertainties in the reconstructed wind field. The volume averaging uncertainty will increase, because a higher variance of the wind speed inside the measurement volume of the LiDAR will be present. The wind field could be complicated further by introducing low-level jets, for example. Then the reconstruction of the wind field can no longer be based on a power law and a different, more general description should be used. One option would be to use Laguerre basis functions to describe the reconstructed wind field. This again introduces new uncertainties that are likely to be higher, because now the equation describing the wind field is not known beforehand and so it is uncertain how well the Laguerre basis functions can capture the wind field. Moreover, a scaling factor is used for the Laguerre basis function which influences the uncertainty of the reconstructed wind field. It is not immediately clear which scaling factor would produce the best results, and this should thus be studied further.

The floating motions that are studied in this thesis are already quite detailed, but a similar approach can be used to actual IMU measurements as a check for the 6DOF simulated results. One difference that is present in these IMU-measured motions are large differences in yaw angle due to direction changes of the wind field. These changes act almost as step changes and occur due to control of the wind turbine, which is not modelled in the simulations.

The model of the LiDAR can also be improved. Firstly, knowing exactly the input parameters would improve the accuracy of the weighting functions. In particular, knowing the pulse duration would decrease the possible variance of the outputs. Moreover, the range gate weighting function used here is a convolution between a Gaussian pulse shape and a rectangular windowing function. However, it is known that this does not exactly represent what the range gate weighting function for the Widncube Nacelle Long-Range configuration looks like. The manufacturer could give the exact equation and parameters.

The uncertainty of the LiDAR parameters should be inserted in the model too, to have a complete picture of the total uncertainty of the reconstructed wind field. The levelling accuracy also influences the final error and uncertainty and is not studied in this thesis.

In addition, the uncertainty of the LiDAR modelling can be improved by incorporating other sources of error and uncertainty, such as the Carrier-to-Noise ratio of the LiDAR.

Once all these improvements are applied to the model, the remaining error and uncertainties are quantified and the model can be applied to real LiDAR measurements on the Tetraspar. No met mast is available on the sight, so no verification is possible for these measurements, but this (improved) study can function as a verification. If a floating offshore wind turbine demonstrator with a reference wind field would be available, this would be a good validation opportunity of the correction method.

This study has focused on correcting individual LOS measurements, but focused on reconstruction with a 10-minute average. However, for studies of the effect of turbulence this correction method can also be used. The outputs should then be implemented in a different reconstruction algorithm, such as the Kriging algorithm to quantify turbulence developed by Romain Tiphaigne in [46]. For this method the mean wind speed should be subtracted, and thus the results from this research can be used for that.

The corrected wind data can then be used as an input to BHawC-Orcaflex to model the loads on the Tetraspar demonstrator. Consequently, these loads can be compared to the loads measured on the demonstrator. This can improve the modelling tool and in turn improve floating wind turbine design.

Besides, using the correction method for load validation, it also has potential as a use for real-time turbine control. If the wind field is known more precisely, a better control strategy can be implemented.

Another application that this correction of LiDAR data can be used for is power performance optimisation. In [21] it is stated that an error of 1% in the reconstructed wind speed is already significant for power performance measurements. If the real wind field is known, this can be compared with the generated power and more precise power curve studies can be made. With the results of this thesis, a follow-up on [26], where it was suggested that motion compensations in LiDAR measurements could reduce the standard deviation of a 10-minute average for power measurements up to 5.6% for nacelle-based LiDAR measurements on a floating offshore wind turbine.

The method developed in this thesis can also be incorporated in the aero-hydro-elastic code BHawC-Orcaflex to improve simulations.

References

[1] Payam Aboutalebi et al. “Switching Control Strategy for Oscillating Water Columns Based on Response Amplitude Operators for Floating Offshore Wind Turbines Stabilization”. In: *Applied Sciences 2021, Vol. 11, Page 5249* 11 (11 June 2021). Used picture for FOWT motion, p. 5249. ISSN: 2076-3417. DOI: 10.3390/APP11115249.

[2] V.A. Banakh and I.N. Smalikho. “ESTIMATION OF THE TURBULENCE ENERGY DISSIPATION RATE FROM THE PULSED DOPPLER LIDAR DATA”. In: *Atmos. Oceanic Opt* 10 (12 1997).

[3] Christine Weibøl Bertelsen. *IEC 61400-1:2019 Wind energy generation systems - Part 1: Design requirements*. 2018. URL: https://webstore.iec.ch/en/publication/26423.

[4] Michael Borg et al. “Technical Definition of the TetraSpar Demonstrator Floating Wind Turbine Foundation”. In: *Energies 2020, Vol. 13, Page 4911* 13 (18 Sept. 2020), p. 4911. ISSN: 1996-1073. DOI: 10.3390/EN13184911. URL: https://www.mdpi.com/1996-1073/13/18/4911/htm%20https://www.mdpi.com/1996-1073/13/18/4911.

[5] S Butterfield et al. “Engineering Challenges for Floating Offshore Wind Turbines”. In: (2007). URL: http://www.osti.gov/bridge.

[6] Leosphere (a Vaisala company). *WindCube Nacelle PO user manual - Version v2.2 – Long Range PPT configuration*.

[7] Stephen Crowder et al. “Analytical Methods for the Propagation of Uncertainties”. In: *Introduction to Statistics in Metrology* (2020), pp. 131–151. DOI: 10.1007/978-3-030-53329-8_7.

[8] Stephen Crowder et al. “Monte Carlo Methods for the Propagation of Uncertainties”. In: *Introduction to Statistics in Metrology* (2020), pp. 153–180. DOI: 10.1007/978-3-030-53329-8_8.

[9] Jian S. Dai. “Euler–Rodrigues formula variations, quaternion conjugation and intrinsic connections”. In: *Mechanism and Machine Theory* 92 (Oct. 2015), pp. 144–152. ISSN: 0094-114X. DOI: 10.1016/J.MECHMACHTHEORY.2015.03.004.

[10] Mohammad Dehghani Soltani et al. “Safety Analysis for Laser-Based Optical Wireless Communications: A Tutorial”. In: *Proceedings of the IEEE* 110.8 (2022), pp. 1045–1072. DOI: 10.1109/JPROC.2022.3181968.

[11] Thibault Désert, Graham Knapp, and Sandrine Aubrun. “Quantification and Correction of Wave-Induced Turbulence Intensity Bias for a Floating LIDAR System”. In: *Remote Sensing 2021, Vol. 13, Page 2973* 13 (15 July 2021), p. 2973. ISSN: 2072-4292. DOI: 10.3390/RS13152973.

[12] “Emissions Trends and Drivers”. In: *Climate Change 2022 - Mitigation of Climate Change: Working Group III Contribution to the Sixth Assessment Report of the Intergovernmental Panel on Climate Change*. Cambridge University Press, 2023, pp. 215–294. DOI: 10.1017/9781009157926.004.

[13] A. R. Meyer Forsting, N. Troldborg, and A. Borraccino. “Modelling lidar volume-averaging and its significance to wind turbine wake measurements”. In: *Journal of Physics: Conference Series* 854 (1 June 2017). ISSN: 17426596. DOI: 10.1088/1742-6596/854/1/012014.

[14] Rod Frehlich. “Coherent Doppler lidar measurements of winds”. In: *Trends in Optics* (Jan. 1996), pp. 351–370. DOI: 10.1016/B978-012186030-1/50021-7.

[15] Rod Frehlich. “Doppler lidar measurements of winds and turbulence in the boundary layer”. In: *IOP Conf. Ser.: Earth Environmental Science* 1 (2008), p. 12017. DOI: 10.1088/1755-1307/1/1/012017.

[16] Rod Frehlich, Stephen M Hannon, and Sammy W Henderson. “COHERENT DOPPLER LIDAR MEASUREMENTS OF WIND FIELD STATISTICS”. In: *Boundary-Layer Meteorology* 86 (Feb. 1998). Derivation of pulse of pulsed LiDAR intensity description, pp. 233–256. DOI: https://doi.org/10.1023/A:1000676021745.

[17] Rod Frehlich and Michael J. Yadlowsky. “Performance of Mean-Frequency Estimators for Doppler Radar and Lidar”. In: *Journal of Atmospheric and Oceanic Technology* 11 (1994), pp. 1217–1230. URL: https://api.semanticscholar.org/CorpusID:121045932.

[18] Hamid Ghorbani. “MAHALANOBIS DISTANCE AND ITS APPLICATION FOR DETECTING MULTIVARIATE OUTLIERS”. In: *Facta Universitatis, Series: Mathematics and Informatics* 0 (0 Oct. 2019), pp. 583–595. ISSN: 2406-047X. DOI: 10.22190/FUMI1903583G. URL: https://casopisi.junis.ni.ac.rs/index.php/FUMathInf/article/view/5028.

[19] Moritz Gräfe, Vasilis Pettas, and Po Wen Cheng. “Wind field reconstruction using nacelle based lidar measurements for floating wind turbines”. In: *Journal of Physics: Conference Series* 2265 (4 May 2022), p. 042022. ISSN: 1742-6596. DOI: 10.1088/1742-6596/2265/4/042022.

[20] Moritz Gräfe, Vasilis Pettas, and Po Wen Cheng. “Wind field reconstruction using nacelle based lidar measurements for floating wind turbines”. In: *Journal of Physics: Conference Series* 2265 (4 May 2022), p. 042022. ISSN: 1742-6596. DOI: 10.1088/1742-6596/2265/4/042022.

[21] Moritz Gräfe et al. “Quantification and correction of motion influence for nacelle-based lidar systems on floating wind turbines”. In: *Wind Energy Science* 8 (6 June 2023), pp. 925–946. ISSN: 23667451. DOI: 10.5194/WES-8-925-2023.

[22] Cvi Melles Griot. *Gaussian Beam Optics - CVI Melles Griot 2009 Technical Guide, Vol 2, Issue 1*. 2009. URL: www.cvimellesgriot.com.

[23] Tatsuo Hanafusa, Chong Bum Lee, and Aloysius K. Lo. “Dependence of the exponent in power law wind profiles on stability and height interval”. In: *Atmospheric Environment (1967)* 20 (10 Jan. 1986), pp. 2059–2066. ISSN: 0004-6981. DOI: 10.1016/0004-6981(86)90348-3.

[24] P. Hellekalek. “Don’t trust parallel Monte Carlo!” In: *Proceedings. Twelfth Workshop on Parallel and Distributed Simulation PADS ’98 (Cat. No.98TB100233)*. 1998, pp. 82–89. DOI: 10.1109/PADS.1998.685273.

[25] Rob J Hyndman and George Athanasopoulos. *Forecasting: Principles and Practice (2nd ed)*. 2nd ed. OTexts, 2018. ISBN: 0987507117. URL: https://otexts.com/fpp2/.

[26] Bench Uwe Jassmann et al. “Power curve measurement of a floating offshore wind turbine with a nacelle-based lidar”. In: *Journal of Physics: Conference Series* 2265 (4 May 2022), p. 042016. ISSN: 1742-6596. DOI: 10.1088/1742-6596/2265/4/042016.

[27] Felix Kelberlau et al. “Taking the Motion out of Floating Lidar: Turbulence Intensity Estimates with a Continuous-Wave Wind Lidar”. In: *Remote Sensing 2020, Vol. 12, Page 898* 12 (5 Mar. 2020), p. 898. ISSN: 2072-4292. DOI: 10.3390/RS12050898.

[28] R. Krishnamurthy et al. “Offshore Wind Turbine Wake characteristics using Scanning Doppler Lidar”. In: *Energy Procedia* 137 (Oct. 2017), pp. 428–442. ISSN: 1876-6102. DOI: 10.1016/J.EGYPRO.2017.10.367.

[29] Joyce Lee and Feng Zhao. *Global Wind Report*. Apr. 2024. URL: www.gwec.net.

[30] Per Jonas Petter Lindelöw. “Fiber Based Coherent Lidars for Remote Wind Sensing”. In: (Nov. 2007).

[31] R. C. Lupton and R. S. Langley. “Scaling of slow-drift motion with platform size and its importance for floating wind turbines”. In: *Renewable Energy* 101 (Feb. 2017), pp. 1013–1020. ISSN: 0960-1481. DOI: 10.1016/J.RENENE.2016.09.052.

[32] Axel Matavar. “Wind Field Reconstruction from data of floating LiDARs | TU Delft Repository”. In: (2024). URL: https://resolver.tudelft.nl/uuid:ddb09dd5-7b50-4a72-886a-81c9c42623ee.

[33] Torben Mikkelsen. “On mean wind and turbulence profile measurements from ground-based wind lidars: limitations in time and space resolution with continuous wave and pulsed lidar systems”. In: *EWEC* 6 (2009), pp. 4123–4132.

[34] Holger Nobach. *Practical Realization of Bessel’s Correction for a Bias-Free Estimation of the Auto-Covariance and the Cross-Covariance Functions*. May 2017. URL: https://arxiv.org/pdf/2303.11047.

[35] Mathieu Pellé. “Flow structure detection using a numerical lidar measurement model”. In: (2022). URL: https://resolver.tudelft.nl/uuid:ab55d015-e3e2-4075-8397-8a88132f13bd.

[36] Vasilis Pettas et al. “A numerical framework for constraining synthetic wind fields with lidar measurements for improved load simulations”. In: *AIAA Scitech 2020 Forum*. Reston, Virginia: American Institute of Aeronautics and Astronautics, Jan. 2020, pp. 1–6. ISBN: 978-1-62410-595-1. DOI: 10.2514/6.2020-0993. URL: https://doi.org/10.2514/6.2020-0993.

[37] Bello Abdulkadir Rasheed et al. “Robust weighted least squares estimation of regression parameter in the presence of outliers and heteroscedastic errors”. In: *Jurnal Teknologi* 71 (1 Nov. 2014), pp. 11–18. ISSN: 21803722. DOI: 10.11113/JT.V71.3609. URL: https://www.researchgate.net/publication/273311220_Robust_Weighted_Least_Squares_Estimation_of_Regression_Parameter_in_the_Presence_of_Outliers_and_Heteroscedastic_Errors.

[38] Oliver Reitebuch. “Wind Lidar for Atmospheric Research”. In: *Atmospheric Physics: Background – Methods – Trends*. Ed. by Ulrich Schumann. Berlin, Heidelberg: Springer Berlin Heidelberg, 2012, pp. 487–507. ISBN: 978-3-642-30183-4. DOI: 10.1007/978-3-642-30183-4_30.

[39] Oliver Reitebuch and R. Michael Hardesty. “Doppler Wind Lidar”. In: *Springer Handbook of Atmospheric Measurements*. Ed. by Thomas Foken. Cham: Springer International Publishing, 2021, pp. 759–797. ISBN: 978-3-030-52171-4. DOI: 10.1007/978-3-030-52171-4_27.

[40] Bahaa E.A. Saleh and Malvin Carl Teich. *Fundamentals of Photonics*. 3rd ed. John Wiley and Sons, Ltd, 2019. ISBN: 9781119506874. URL: https://learning.oreilly.com/library/view/fundamentals-of-photonics/9781119506874/c03.xhtml.

[41] SBG Systems SAS. *EKINOX Series Tactical Grade MEMS Inertial Sensors Hardware Manual*. 2007.

[42] Eric Simley et al. “Analysis of light detection and ranging wind speed measurements for wind turbine control”. In: *Wind Energy* 17.3 (2014), pp. 413–433. DOI: https://doi.org/10.1002/we.1584.

[43] Christopher W. Slinger and Michael Harris. “Introduction to continuous-wave Doppler lidar”. In: 2012. URL: https://api.semanticscholar.org/CorpusID:129938731.

[44] Matt Smith and Euan Macdonald. “The Competitive Advantage of Onshore Lidar: Lessons from the Offshore Wind Industry Applications”. In: *Lecture Notes in Civil Engineering* 395 (2024), pp. 2859–2869. ISSN: 23662565. DOI: 10.1007/978-981-99-9722-0_198/FIGURES/7. URL: https://link.springer.com/chapter/10.1007/978-981-99-9722-0_198.

[45] J. Sanz Subirana, J.M. Juan Zornoza, and M. Hernández-Pajares. *Conventional Terrestrial Reference System - Navipedia*. 2011. URL: https://gssc.esa.int/navipedia/index.php?title=Conventional_Terrestrial_Reference_System.

[46] Romain Tiphaigne. “Fourier space methods for wind field reconstruction with LiDAR measurements”. In: (2024).

[47] Thanh Toan Tran and Dong Hyun Kim. “The platform pitching motion of floating offshore wind turbine: A preliminary unsteady aerodynamic analysis”. In: *Journal of Wind Engineering and Industrial Aerodynamics* 142 (July 2015), pp. 65–81. ISSN: 0167-6105. DOI: 10.1016/J.JWEIA.2015.03.009.

[48] Ulla Wandinger. “Introduction to Lidar”. In: *Lidar* (June 2005), pp. 1–18. DOI: 10.1007/0-387-25101-4_1. URL: https://link.springer.com/chapter/10.1007/0-387-25101-4_1.

[49] Christian Werner. “Doppler Wind Lidar”. In: *Lidar: Range-Resolved Optical Remote Sensing of the Atmosphere*. Ed. by Claus Weitkamp. New York, NY: Springer New York, 2005, pp. 325–354. ISBN: 978-0-387-25101-1. DOI: 10.1007/0-387-25101-4_12.

[50] Rebecca Williams, Feng Zhao, and Joyce Lee. *Global Offshore Wind Report*. June 2022. URL: www.gwec.net.

A

Derivation unbiased weighted variance

The following weighted variance defined in (A.1) has a bias. The expectation of the weighted sample variance s^2 should be adjusted to be equal to the unbiased weighted population variance σ_w^2. The bias can be found by calculating the expectation of the weighted sample variance as expressed in (A.2). Here m is the total number of samples.

$$s^2 = \frac{\sum_{i=1}^{m} w_i (x_i - \mu)^2}{\sum_{i=1}^{m} w_i} \tag{A.1}$$

$$\mathbb{E}(s^2) = \sigma_w^2 \left(1 - \frac{\sum_{i=1}^{m} w_i^2}{(\sum_{i=1}^{m} w_i)^2} \right) \tag{A.2}$$

(A.2) is derived below in (A.3) based on the lecture notes of Dr. H. Nobach [34], realising that the mean is in fact a weighted average and thus also contains weights.

$$s^2 = \frac{\sum_{i=1}^{m} w_i (x_i - \mu)^2}{\sum_{i=1}^{m} w_i} = \frac{\sum_{i=1}^{m} w_i \left(x_i - \frac{\sum_{j=1}^{m} w_j x_j}{\sum_{j=1}^{m} w_j} \right)^2}{\sum_{i=1}^{m} w_i} \tag{A.3}$$

First expanding the part between brackets in (A.4).

$$\left(x_i - \frac{\sum_{j=1}^{m} w_j x_j}{\sum_{j=1}^{m} w_j} \right)^2 = x_i^2 + \frac{\sum_{j=1}^{m} \sum_{k=1}^{m} w_j w_k x_j x_k}{\left(\sum_{j=1}^{m} w_j \right)^2} - 2 \frac{\sum_{j=1}^{m} w_j x_j x_i}{\sum_{j=1}^{m} w_j} \tag{A.4}$$

Substituting back into (A.3), to get (A.5).

$$s^2 = \frac{\sum_{i=1}^{m} w_i x_i^2}{\sum_{i=1}^{m} w_i} + \frac{\cancel{\sum_{i=1}^{m} w_i} \sum_{j=1}^{m}\sum_{k=1}^{m} w_j w_k x_j x_k}{\cancel{\sum_{i=1}^{m} w_i} \left(\sum_{j=1}^{m} w_j\right)^2} - 2\frac{\sum_{j=1}^{m}\sum_{i=1}^{m} w_j w_i x_j x_i}{\left(\sum_{j=1}^{m} w_j\right)^2} \tag{A.5}$$

The second term in (A.5) k can easily be interchanged with i, resulting in (A.6).

$$s^2 = \frac{\sum_{i=1}^{m} w_i x_i^2}{\sum_{i=1}^{m} w_i} + \frac{\sum_{j=1}^{m}\sum_{i=1}^{m} w_j w_i x_j x_i}{\left(\sum_{j=1}^{m} w_j\right)^2} - 2\frac{\sum_{j=1}^{m}\sum_{i=1}^{m} w_j w_i x_j x_i}{\left(\sum_{j=1}^{m} w_j\right)^2} \tag{A.6}$$

Now that the last two terms are proportional to the same parameters, the equation can be simplified to (A.7).

$$s^2 = \frac{\sum_{i=1}^{m} w_i x_i^2}{\sum_{i=1}^{m} w_i} - \frac{\sum_{j=1}^{m}\sum_{i=1}^{m} w_j w_i x_j x_i}{\left(\sum_{j=1}^{m} w_j\right)^2} \tag{A.7}$$

Taking the expectation of the sample variance as expressed in (A.7), results in (A.8).

$$\mathbb{E}(s^2) = \frac{\sum_{i=1}^{m} w_i \mathbb{E}(x_i^2)}{\sum_{i=1}^{m} w_i} - \frac{\sum_{j=1}^{m}\sum_{i=1}^{m} w_j w_i \mathbb{E}(x_j x_i)}{\left(\sum_{j=1}^{m} w_j\right)^2} \tag{A.8}$$

If the variables x_i are considered independent, that is, no correlation is present between the samples. For $i \neq j$ it thus holds that $\mathbb{E}_{i\neq j}(x_i x_j) = \mu^2$. For $i = j$, it is generally known that $\mathbb{E}(x_i^2) = \mathrm{Var}(x_i) + \mathbb{E}(x_i)^2 = \sigma_w^2 + \mu^2$ holds.

$$\mathbb{E}(s^2) = \sigma_w^2 \left(1 - \frac{\sum_{i=1}^{m} w_i^2}{\left(\sum_{i=1}^{m} w_i\right)^2}\right) \tag{A.9}$$

Now, to obtain the unweighted variance, the expression for s^2 in (A.1) should be divided by the factor between brackets in (A.9). Finally, the unbiased weighted variance can then be computed as in (A.10).

$$\sigma_w^2 = \frac{\sum_{i=1}^{m} w_i (x_i - \mu)^2}{\sum_{i=1}^{m} w_i \left(1 - \frac{\sum_{i=1}^{m} w_i^2}{\left(\sum_{i=1}^{m} w_i \right)^2} \right)} = \frac{\sum_{i=1}^{m} w_i (x_i - \mu)^2}{\left(\sum_{i=1}^{m} w_i - \frac{\sum_{i=1}^{m} w_i^2}{\left(\sum_{i=1}^{m} w_i \right)} \right)} = \mathcal{N} \sum_{i=1}^{m} w_i (x_i - \mu)^2 \tag{A.10}$$

In this way, the normalisation factor $\mathcal{N}$ of (3.30) has been proven that ensures unbiased (co)variance in section 3.3. The bias due to a decrease in degrees of freedom have been corrected for. It can also be noted that in the limiting case where all weights are equal, the expression simplifies to the regular Bessel's correction in (A.11).

$$\sigma^2 = \frac{1}{m-1} \sum_{i=1}^{m} (x_i - \mu)^2 \tag{A.11}$$